

Master's Thesis for the acquisition of the academic degree
Master of Science in Earth Sciences

The application of
Ground-Based InSAR to understand
slope behavior at the Hornbergl in
Reutte, Tyrol and the Ingelsberg in
Bad Hofgastein, Salzburg, Austria

Author: Klaus Unterberger, BSc.

Supervisor: Univ.-Prof. B.A. M.S. Ph.D. Daniel Scott Kieffer

Department of Applied Geosciences, Graz, University of Technology

Graz, October 2013

Statutory Declaration

I declare that I have authored this thesis independently, that I have not used other than the declared sources / resources, and that I have explicitly marked all material which has been quoted either literally or by content from the used sources.

Graz, am

.....

(Klaus Unterberger)

Acknowledgements

I want to thank my Supervisor Univ.-Prof. B.A. M.S. Ph.D. Daniel Scott Kieffer for his valuable suggestions, enthusiastic encouragement and useful critiques during the planning and development of this thesis. My grateful thanks are also extended to all members of the Institute of Applied Geosciences for their support during field works, data analysis and organizational issues.

I wish to acknowledge the help provided by the WLV Ausserfern, under the guidance of Dr. Thomas Sausgruber and Dipl.-Ing. Christian Ihrenberger, for enabling equipment installation and providing financial support for the measurements at the Hornbergl. My special thanks should be given to Mr. Fritz Zettenig, mayor of the municipality of Bad Hofgastein, Josef Lainer and Mag. Gerald Valentin, representing the Geological Service of Salzburg, who provided ideal infrastructure and financial support for the implementation of measurements at the Ingelsberg. Meteorological data provided by the *'Flugsportverein Reutte-Höfen'* is also greatly appreciated.

I wish to thank my roommates, Matthias and Theresa, and my fellow students, especially Cyrill, Istvan and Peter, for their constructive support and refreshing company during the last years. Special thanks belong to my girlfriend Nora for her encouraging help and patience when it was most required. Finally, I wish to thank my family for their endless support and encouragement throughout my study.

Abstract

In the last years Ground-Based Interferometric Synthetic Aperture Radar (GBInSAR) has proven its possibilities and advantages in detecting displacements and deformations in unstable areas. Two mass movement affected sites, the Hornbergl in Reutte, Tyrol and the Ingelsberg in Bad Hofgastein, Salzburg were investigated using this powerful tool to better understand the effective slope behavior.

The key concepts of GBInSAR, as well as the data processing and analysis are described in this thesis. At both sites monitoring delivered continuous information of occurred displacement with accuracy in the range of millimeters. Additionally, a high temporal resolution with measurement intervals below seven minutes was provided. Movement patterns could be observed and evaluated. Moreover, the extent of landslide affected area was defined and possibly collapsing parts were highlighted.

Measurement results for the Hornbergl displayed constant displacement within depositional areas (e.g. talus and toe areas), not indicating significant movement of extensive parts of the steep and confining cliffs. At the Ingelsberg continuous displacement within depositional areas as well as distinctive rock fall events could be detected. A comparison with different monitoring methods (e.g. fissurometer) proved the consistent displacement tendencies detected by various techniques. Time of slope failure predictions were calculated using the method proposed by Fukuzono (1985).

Summarizing GBInSAR delivers highly useful information about the slope behavior of both investigation sites, considering a few limiting factors (e.g. vegetation and atmospheric influence).

Kurzfassung

In den letzten Jahren hat sich bodengestützte Radarinterferometrie mit synthetischer Apertur (GBInSAR) als ein leistungsstarkes Instrument für die Überwachung von Verformungen und Bewegungen in instabilen Regionen bewährt. Mit dem Hornbergl, nahe Reutte in Tirol, und dem Ingelsberg, nahe Bad Hofgastein in Salzburg, wurden zwei Gebiete, die akut von Massenbewegungen betroffen sind, mittels dieser Technologie untersucht um die vorherrschenden Hangprozesse besser zu verstehen.

In dieser Arbeit werden die Grundprinzipien von GBInSAR, als auch die Datenverarbeitung und Auswertung besprochen. In beiden Untersuchungsgebieten konnten kontinuierliche Verschiebungsdaten mit einer Genauigkeit im Millimeterbereich erfasst werden. Messintervalle von unter sieben Minuten ermöglichten eine enorm hohe zeitliche Auflösung der Verschiebungsdaten. Bewegungsmuster wurden erfasst und bewertet und zusätzlich konnte das Ausmaß der, von Massenbewegungen betroffenen, Gebiete abgegrenzt werden, wobei mögliche Gefahrenbereiche hervorgehoben wurden.

Die Messergebnisse für das Hornbergl zeigten durchgehend Bewegungen in den Ablagerungsbereichen (z.B.: Schuttkegel und Fußbereiche), jedoch keinerlei signifikante oder großflächige Verschiebungen in den angrenzenden Steilwänden. Am Ingelsberg konnten kontinuierliche Bewegungen in den Ablagerungsbereichen, als auch plötzliche Felsstürze beobachtet werden. Eine Gegenüberstellung der Radardaten mit anderen Überwachungsmethoden (z.B.: Fissurometer) bestätigte die Bewegungstendenzen der verschiedenen Messprogramme. Eine Prognose der Versagenszeitpunkte wurde mittels der Methode nach Fukuzono (1985) erstellt.

Zusammenfassend lieferte GBInSAR enorm nützliche Informationen der vorherrschenden Hangprozesse in beiden Untersuchungsgebieten zur Verbesserung der geologischen Modelvorstellungen.

List of Acronyms

DEM	Digital Elevation Model
DTM	Digital Terrain Model
GCP	Ground Control Points
GNSS	Global Navigation Satellite System
GBInSAR	Ground-Based Interferometric Synthetic Aperture Radar
IBIS	Image by Interferometric Survey
IBIS-DV	IBIS-Data Viewer
IDS	Ingegneria dei Sistemi
IDTF	Inverse Discrete Fourier Transform
InSAR	Interferometric Synthetic Aperture Radar
KB	Kilobyte
LoS	Line of Sight
MB	Megabyte
NASA	National Aeronautics and Space Administration
ÖBRD	Österreichischer Bergrettungsdienst
PSI	Persistent Scatterer Interferometry
PS	Persistent Scatterer
PS	Permanent Scatterer
Radar	Radio detection and ranging

SAR	Synthetic Aperture Radar
SFCW	Stepped Frequency Continuous Wave
SNR	Signal to Noise Ratio
TInSAR	Terrestrial Interferometric Synthetic Aperture Radar
WLV	Wildbach und Lawinenverbauung
ZAMG	Zentralanstalt für Meteorologie und Geodynamik

List of Symbols

A	Constant
B	Bandwidth
c	Speed of light
C	Celsius
f	Frequency
L	Scan length
n/N	Imaginary number
r	Distance
R_{max}	Maximum distance
ΔR	Range resolution
T_0	Echo delay
Δt	Scan time

Δt	Difference receiving time
t_f	Time of slope failure
α	Constant
$\Delta\vartheta$	Cross-range resolution
λ	Wavelength
τ	Duration of pulse
φ	Measured interferometric phase
$\Delta\varphi_{atm}$	Interferometric phase due to atmospheric changes
$\Delta\varphi_n$	Interferometric phase due to phase ambiguity
$\Delta\varphi_{noise}$	Interferometric phase due to noise
$\Delta\varphi_r$	Interferometric phase due to displacement

Index

1.	Introduction	1
1.1	Objectives	1
2.	Literature Review.....	2
2.1	GBInSAR Technology.....	2
2.1.1	Principles	3
2.1.1.1	Pulse Radar	4
2.1.1.2	SF-CW.....	6
2.1.1.3	SAR.....	7
2.1.1.4	Focusing	9
2.1.1.5	Interferometry.....	11
2.1.2	Permanent Scatterer	13
2.1.3	Corner Reflectors	13
2.2	IBIS-FL	14
2.2.1	Advantages and Disadvantages.....	16
2.3	IBIS Controller	17
2.3.1	Masking	18
2.4	IBIS Evaluation Software.....	19
2.4.1	IBIS Guardian	19
3.	Hornbergl Study Site.....	21
3.1	Regional Setting	21
3.2	Site Conditions	25

3.3	Historical Landsliding & Mitigation Measures.....	29
3.4	Previous Survey Campaigns.....	30
4.	Ingelsberg Study Site	32
4.1	Regional Setting.....	32
4.2	Site Conditions.....	36
4.3	Historical Landsliding & Mitigation Measures.....	40
4.4	Previous Survey Campaigns.....	41
5.	Hornbergl GBInSAR Measurement Campaign.....	43
5.1	Instrument Setup.....	43
5.2	Measurement Results.....	47
5.3	Comparison of Monitoring Methods.....	50
5.4	Interpretation	52
6.	Ingelsberg GBInSAR Measurement Campaign	55
6.1	Instrument Setup.....	55
6.2	Measurement Results.....	58
6.2.1	Phase 1 (27.03. – 01.05.2013).....	58
6.2.2	Phase 2 (03.05.2013 - Present)	62
6.2.3	Comparison of Different Masks	69
6.2.4	IBIS Data Viewer	70
6.2.4.1	Ground Control Points.....	71
6.3	Comparison of Monitoring Methods.....	73
6.4	Interpretation	76
6.4.1	Phase 1 (27.03. – 01.05.2013).....	76
6.4.2	Phase 2 (03.05.2013 - Present)	79
6.4.3	Slope Failure Prediction	84

7.	Summary & Conclusions	87
7.1	Hornbergl.....	87
7.2	Ingelsberg	88
8.	Appendix.....	92
8.1	List of Figures.....	92
8.2	List of Tables	99
8.3	List of References	99

1. Introduction

The need for a precise, real-time and safe monitoring of hillslope deformations and stability is indispensable. With a rising number of settlements and infrastructure in possibly hazardous mountainous regions, the impact of devastating events is increasing (Schaes, 2012). Precise, real-time monitoring data contributes hazard maps to predict future hillslope failures, for example by applying the inverse velocity method of Fukuzono (1985).

1.1 Objectives

To gain a better understanding of slope behavior and to generate comprehensive displacement maps of the Hornbergl and the Ingelsberg the application of a Ground-Based Interferometric Synthetic Aperture Radar (GBInSAR) is advantageous, as this technique enables the remote monitoring of large-scale landslides with accuracy in the mm range (Luzi, 2010, Mazzanti, 2011). The generated displacement maps include information for every scanned pixel, offering time series plots of displacement or velocity for the entire survey domain. A continuous displacement map provides necessary information regarding the magnitude and location of movements. Using the GBInSAR measurements the main objectives include:

- Gain insight to slope processes
- Assess whether significant volumes of rock or soil material displace or once in motion potentially mobilize into a significant landslide event
- Correlation of displacement to climate variations
- Where applicable, compare GBInSAR results to independent conventional survey measurements
- Where possible, use the inverse velocity method of Fukuzono (1985) to estimate time of slope failure

2. Literature Review

2.1 GBInSAR Technology

This chapter is dedicated to deliver an introduction from the invention of the basic principles of radar to the nowadays applied method GBInSAR (Ground-Based Interferometric Synthetic Aperture Radar). Radar is an acronym for Radio detection and ranging and involves a technique, where the backscattered echoes of actively generated microwaves are measured (Rödelsperger, 2011). In this process electromagnetic waves illuminate objects, surfaces and volumes with a certain resolution (Luzi, 2010). With the invention of synthetic aperture radar (SAR) the spatial resolution of radar images was improved significantly. Over the last couple of decades, satellite-borne radar used for remote sensing became a powerful and highly reliable tool for investigating the Earth's surface. With the launch of the NASA satellite SEASAT in 1978 it was soon demonstrated that synthetic aperture radar (SAR) was able to acquire features like topography, morphology or roughness of the backscattering layer (Bamler and Hartl, 1998). In the late 1980s the first interferograms were produced, whereby several acquired SAR images were compared with each other. More exactly interferometry exploits the phase information of at least two different SAR images to retrieve temporal or spatial information of the propagating waves (Luzi, 2010). Information derived from these interferograms can be used to assess different parameters, such as topography, deformations of the surface or vegetation properties (Bamler and Hartl, 1998). This new method, called Interferometric Synthetic Aperture Radar (InSAR) enabled the mapping and detection of huge areas with respect to surface displacements (Bamler and Hartl, 1998).

In contrary to the satellite born method ground-based or terrestrial InSAR was developed to acquire images with higher temporal resolution (5-10min) using a stable baseline (Luzi, 2010, Rödelsperger, 2011). The first prototypes of terrestrial InSAR equipment were developed by the Joint Research Center (JRC) of the European Community in the late 90s (Rödelsperger, 2011). The first commercially available apparatus was manufactured by IDS in cooperation with the Department of Electronics and

Telecommunications at the University of Florence and is distributed in similar form since 2006 (Rödelsperger, 2011, Mazzanti, 2011).

In the last decade Ground-Based Interferometric Synthetic Aperture Radar, further on mentioned as GBInSAR, equatable with the term TInSAR (Terrestrial InSAR), as sometimes used in literature, has gained significant interest in the field of Geotechnics (Mazzanti, 2011). This technique uses one microwave emitting and one receiving sensor to gain radar images, while moving along a rail track (Montserrat Hernandez, 2012). One of the biggest advantages of this technique is the independency of weather and daytime limitations due to the usage of microwaves. With providing two dimensional displacement maps at a spatial resolution of a few meters and an accuracy of 1/10mm to 1mm, this novel tool already proved its possibilities on several fields of applications (Rödelsperger, 2011). Especially the monitoring of hazardous slopes and landslides, often in connection with construction sites, stayed in the focus of numerous research projects (Tarchi et al., 2003, Herrera et al., 2009, Barla et al., 2010, Mazzanti et al., 2011, Bozzano et al., 2011), as well as the observation of unstable volcano flanks (Rödelsperger et al., 2009), the generation of digital elevation models (Rödelsperger et al., 2010) or the acquisition of snow cover characteristics (Luzi et al., 2009).

2.1.1 Principles

Working on the basic principle of a Pulse Radar, GBInSAR equipment uses three different techniques to increase the possibilities of radar observations (Rödelsperger, 2011):

- Stepped Frequency Continuous Wave (SFCW) to acquire range resolution (see chapter 2.1.1.2)
- Synthetic Aperture Radar (SAR) to acquire azimuth and cross range resolution (see chapter 2.1.1.3)
- Interferometry to detect and calculate object displacements (see chapter 2.1.1.5)

Generally an image is acquired by the radar head, which moves perpendicular to the measurement direction in a continuous way along the rail. As a result of every acquisition, a two dimensional image with an amplitude and phase information for every

single measurement pixel is generated. Within the radar image a correlation between the phase φ , the known wavelength λ and the distance r is given (Rödelsperger, 2011, Schares, 2012)(Equation 1).

$$\varphi = - \frac{4\pi}{\lambda} * r \quad (1)$$

The dimension of the measured pixels is defined by a constant range resolution of 0.75m and distance dependent cross range resolution of 4.4mrad, which resembles 4.4m at a distance of 1km (IDS, 2013)(www.idscorporation.com);(Figure 1). Basically GBInSAR devices are only capable of measuring displacements along the Line of Sight (LoS) from the antenna head to the illuminated surface.

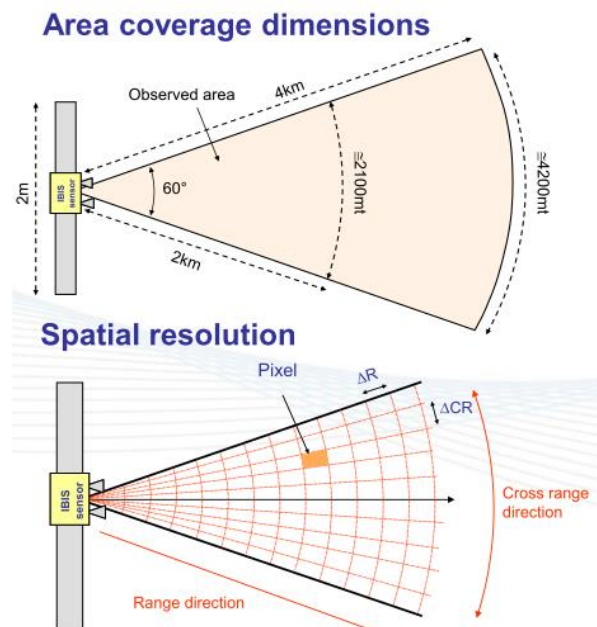


Figure 1, Resolution cells GBInSAR (Kurka, 2012); graphics from IDS, 2011

2.1.1.1 Pulse Radar

Pulse Radar uses an emitted primary signal and a backscattered secondary signal within the microwave frequency to measure a distance to a specific object (Schaes, 2012). In the simplified example of Figure 2 the emitted pulse is reflected by the airplane and received with an echo delay T_0 . Using this information and the known speed of light c ($\approx 3 \times 10^8$ m/s), the distance R_0 to the investigated object can be determined (Coppi, 2011);(Equation 2).

$$2R_0 = c * T_0 \Leftrightarrow R_0 = \frac{c * T_0}{2} \quad (2)$$

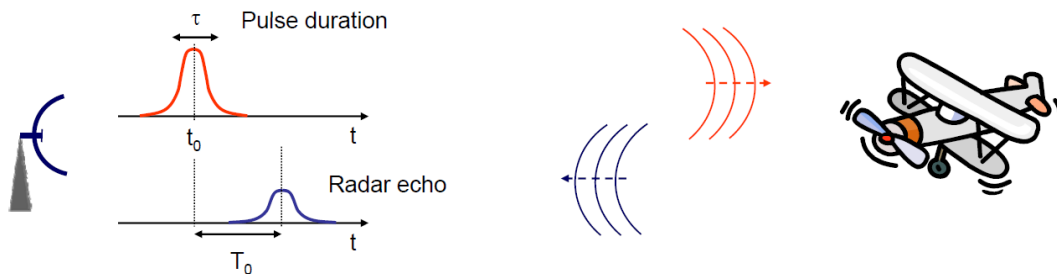


Figure 2, Pulse Radar working principle (Coppi, 2011)

The distinction of echoes of two different pulses is only enabled, if the difference of their receiving time Δt is higher than the duration of the pulse τ or if the distance between the objects Δd is higher than the range resolution ΔR (Figure 3, Equation 3) modified after (Coppi, 2011).

$$\Delta t > \tau \Leftrightarrow \Delta d > \Delta R \quad (3)$$

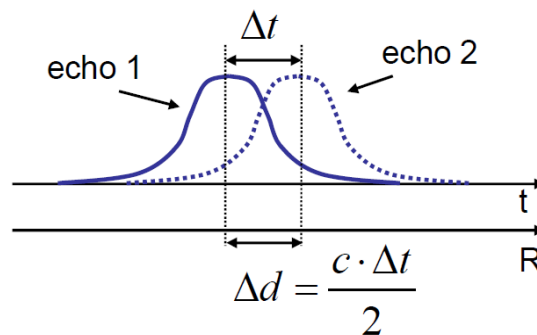


Figure 3, Range resolution concept (Coppi, 2011)

Therefore, the range resolution can be expressed as a dependency of the pulse duration τ or the pulse bandwidth B (Equation 4). To overcome this disadvantageous limitation the pulse width has to be shortened or the SF-CW approach has to be applied to receive a higher range resolution (Rödelsperger, 2011).

$$\Delta R = \frac{c * \tau}{2} = \frac{c}{2B} \quad (4)$$

2.1.1.2 SF-CW

To increase the range resolution the radar pulse is fully synthesized by means of the Stepped Frequency Continuous Wave (SF-CW) technique (Paulose, 1994). This approach uses the fact, that the range resolution is inversely proportional to the swept bandwidth of the radar pulses (Equation 4),(Alba et al., 2008). Instead of transmitting a short pulse with duration τ using a large bandwidth within one frequency domain, the IBIS-FL radar transmits a sweep of synthesized N monochromatic waves equally and incrementally spaced in frequency (Alba et al., 2008, Jungner, 2009). This is realized using fixed frequency steps of Δf within a bandwidth B (Equation 5), (IDS, 2012).

$$B = \Delta f (N - 1) \quad (5)$$

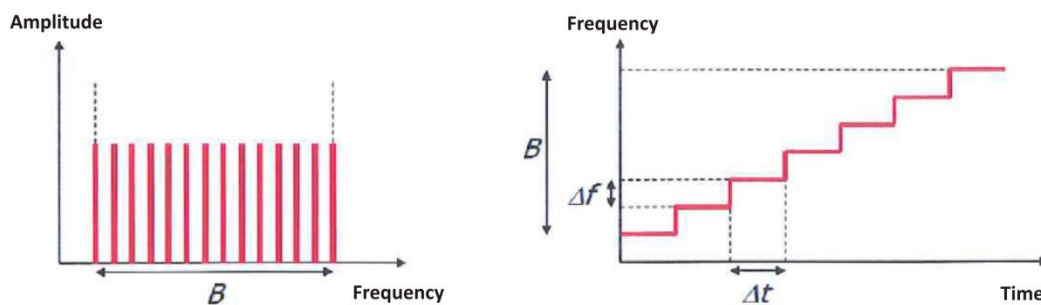


Figure 4, Synthetic pulse with bandwidth B and frequency steps Δf using SF-CW, modified after (Schaes, 2012)

One sweep containing all frequency steps within the entire bandwidth resembles one measurement position of the radar head along the rail (Figure 4), (Schaes, 2012). For each frequency step IBIS-FL acquires a complex vector containing components of the reflected echo representing the frequency response of the N pulses. Using an Inverse Discrete Fourier Transform (IDFT) the stored data is then converted from time to range domain (Coppi, 2011). This range profile delivers a one dimensional map of the reflected objects in the LoS as a function of their relative distance from the radar (Schaes, 2012). The SF-CW approach enables IBIS-FL to provide a range resolution ΔR of 0.75m, which defines certain range bins along the measured profile (Schaes, 2012). The radar beam illuminates n target points at different distances and angles, being 0.75m apart (Alba et al., 2008). Targets within the same range bin return a cumulative response. As a result it is impossible to distinguish between certain objects or their displacements within one

range bin, as the echo delivers a description of the mean changes of all scatterers (Alba et al., 2008, Jungner, 2009). An exemplary range profile illustrates the range resolution concept and the limitation of two or more objects within one range bin (Figure 5).

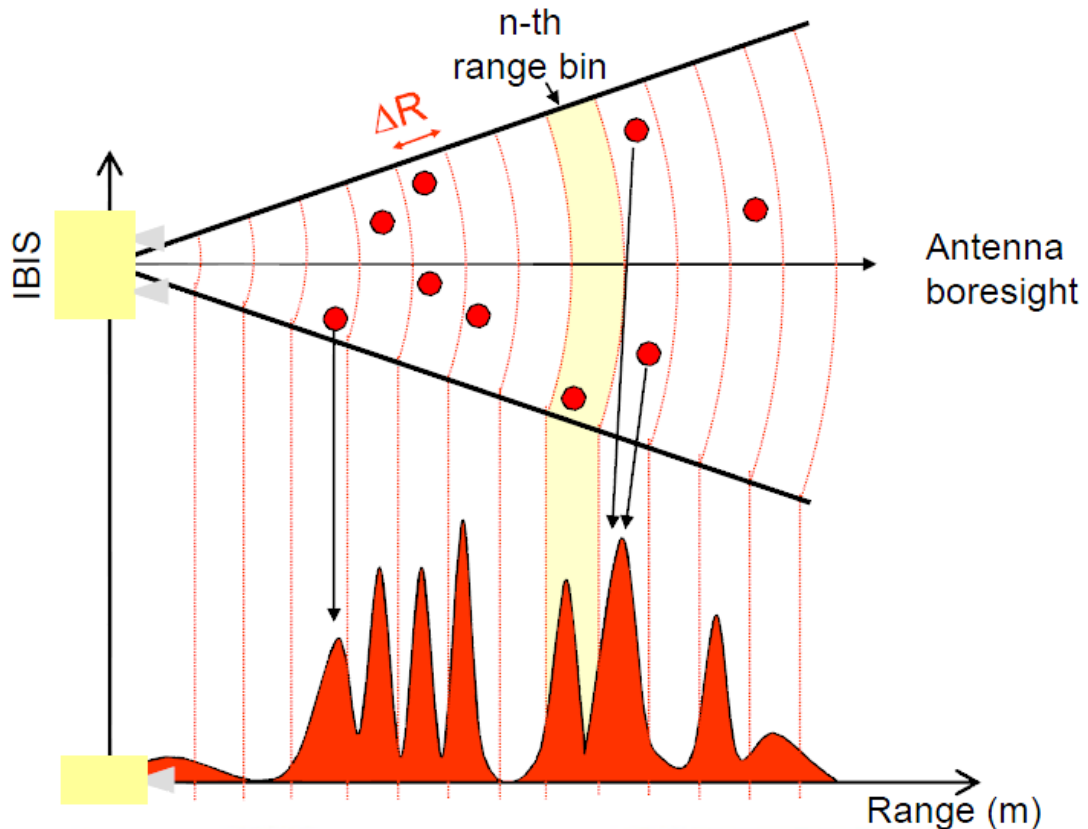


Figure 5, Idealized range measurement along a profile with several targets showing the amplitude of the echoes (Coppi, 2011)

2.1.1.3 SAR

To overcome the problems of illuminated objects in one range bin an additional approach is executed. By moving the radar head along the rail a synthetic aperture is simulated (Rödelsperger, 2011). By combining several coherent, slightly offset images of the same scene, a synthetic aperture allows the focusing of all gained acquisitions into one two-dimensional image (Jungner, 2009). This Synthetic Aperture Radar (SAR) technique is accomplished by a stepped but almost continuous movement along the rail, perpendicular to the measurement direction. All acquired images with slightly different viewing angles are compressed into one image, which adds a cross-range resolution, assuming that all images are captured at the same time (Schaes, 2012). The obtained

angular resolution $\Delta\theta$ is defined by Equation 6, where λ is the wavelength and L the synthesized antenna length (= 2m in case of IBIS-FL);(Alba et al., 2008).

$$\Delta\theta = \frac{\lambda}{2L} \quad (6)$$

As a result of Equation 6 and the 2m movement along the rail a cross-range resolution of 4.4mrad is obtained. Since cross-range resolution is defined as an angle, the measurement cells increase linearly in size in the cross-range direction with distance from the radar (Jungner, 2009). Therefore the pixel resolution changes with distance, reducing the possibility of detecting small-scale objects at the maximum range.

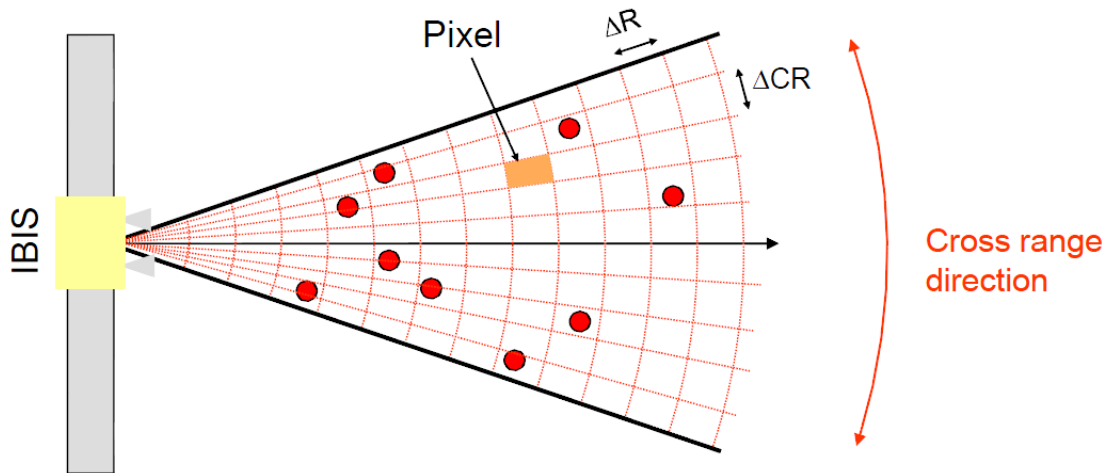


Figure 6, Illustration of the pixel resolution defined by range resolution ΔR and cross range resolution ΔCR (Coppi, 2011)

Combining the SF-CW and the SAR technique exact measurement pixels (Figure 6) are defined by a range resolution of 0.75m and a cross-range resolution of 4.4mrad (e.g. @1km, 0.75m by 4.4m; @2km, 0.75m by 8.8m);(Alba et al., 2008, Coppi, 2011, IDS, 2013).

2.1.1.4 Focusing

One automatic step within the evaluation software IBIS-Guardian to obtain a grid with spatial resolution is the focusing of the detected amplitude and phase values (Rödelsperger, 2011). SAR images highly differ in their geometrical and radiometric properties from optical images, as they mainly depend on the geometry of the target and the type of reflecting material (Rödelsperger, 2011). The application of an Inverse Discrete Fourier Transform (IDFT) onto the raw images enables the transformation of the gained data from the frequency domain into the spatial domain (Schaes, 2012). In Figure 7 the focusing of a GBInSAR image is illustrated. By applying the IDFT on each column of the raw image (Figure 7a) a range focused image is generated (Figure 7b), (Rödelsperger, 2011). Repeating the same procedure for the rows a completely focused image is created (Figure 7c). As last step the image is transposed into a Cartesian x-y-grid (Figure 7d);(Schaes, 2012).

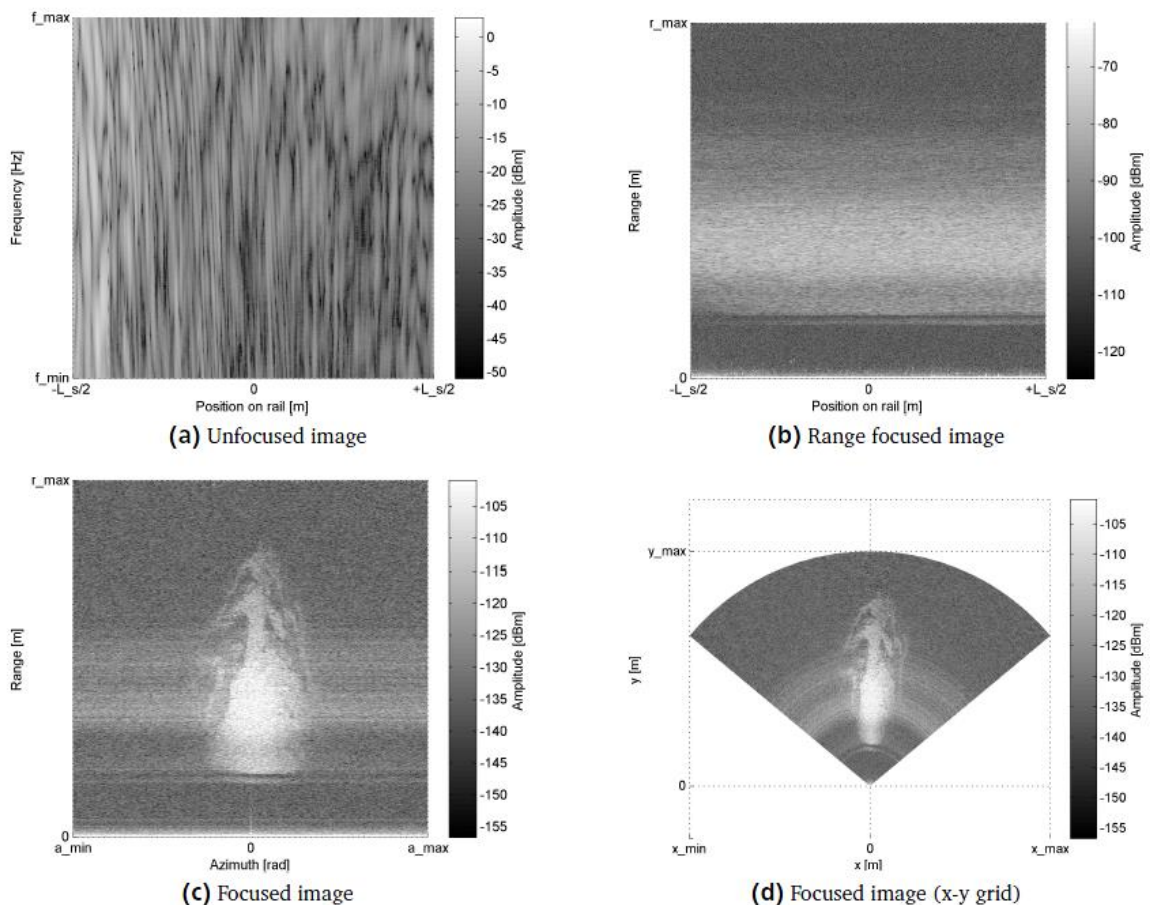


Figure 7, Different stages of focusing during the generation of a GBInSAR image (Amplitude only);(Rödelsperger, 2011)

For interpretation reasons the addition of a geo-referenced Digital Elevation Model (DEM) is indispensable. Introducing a z-coordinate to the system a local three-dimensional coordinate system (X, Y, Z) is required. Its origin is located in the center of GBInSAR rail, whereby X is orientated in direction of the movement of the radar along the rail, Y in direction of the measurement and Z as a vertical axis (Rödelsperger, 2011). The range resolution concept now produces a distortion of the measurement cells due to irregular topography (Rödelsperger, 2011). The main limitation related to this issue is that all objects within one range and azimuth bin, but with different elevation, are mapped indistinguishably into one pixel (Rödelsperger, 2011). A measurement cell is defined by a certain size on a two-dimensional plane. If this cell is projected at a vertical cliff in a three-dimensional system one pixel may cover the entire length of the cliff and therefore summarizes all properties along this cliff into one pixel (Figure 8). This loss of information can be minimized by choosing an advantageous sensor position.

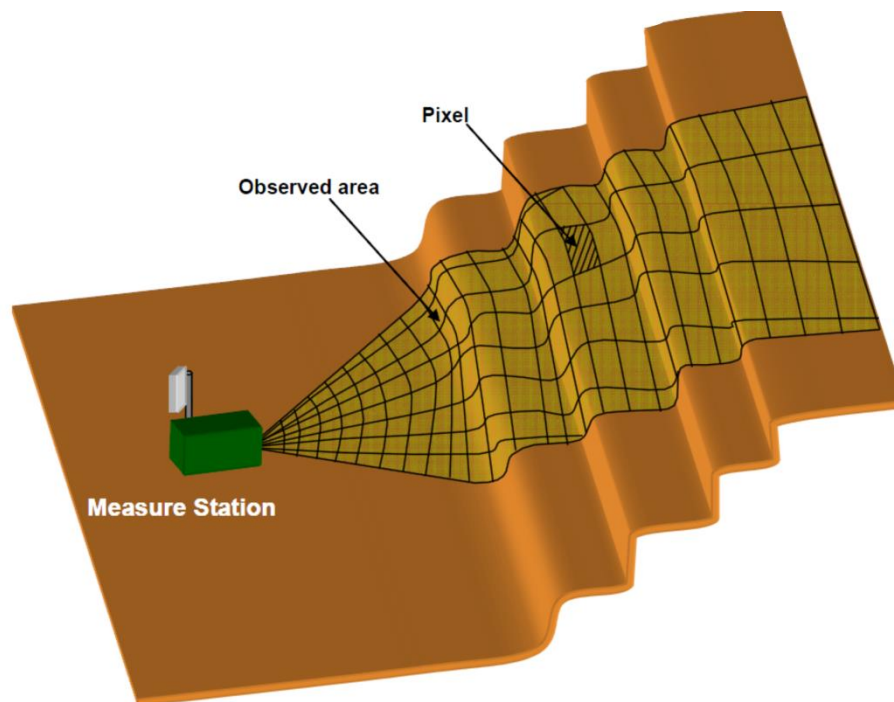


Figure 8, Distortion of measurement cells due to the projection on a three-dimensional system (Coppi, 2011)

2.1.1.5 Interferometry

Interferometry is based upon the comparison of different phase components φ of at least two coherent radar images (Figure 9), (Schaes, 2012). Using data from different viewing points or instants of time the measurement of relative range differences is enabled (Schaes, 2012). In both case studies, the Hornbergl and the Ingelsberg, the SAR images were collected at different time periods, but at the same sensor position. Therefore the spatial baseline equals zero, but a temporal baseline gets introduced, due to the temporal change of the distance between the target and the sensor (Rödelsperger, 2011). Basically a possible displacement d in the Line of Sight for every single pixel can be derived from equation 7 (Mazzanti, 2011, Schaes, 2012).

Two major complications arise during the generation of an interferogram. As the phase is periodic within $[-\pi, +\pi]$ an excess of this value creates a ambiguity of phases, due to the unknown number of phase cycles (Jungner, 2009). Therefore the maximum unambiguous measurable phase between adjacent pixels is reduced to $\pm \frac{\lambda}{4}$, defined by equation 7 using $\pm\pi$.

$$d = -\frac{\lambda}{4\pi}(\varphi_2 - \varphi_1) \quad (7)$$

Using the Ku band with a wavelength of 17,44mm the maximum unambiguous change of distance between two measurements is limited to approximately 4,38mm (Schaes, 2012). If the phase gradient stays below this threshold the absolute or real phase can be reconstructed with phase unwrapping (Jungner, 2009). To resolve a possible transgression of this threshold the Persistent Scatterer Interferometry (PSI) technique is introduced. This approach uses time series of pixels with highly coherent phase measurement results as a stable reference in relation to quickly moving points (Schaes, 2012).

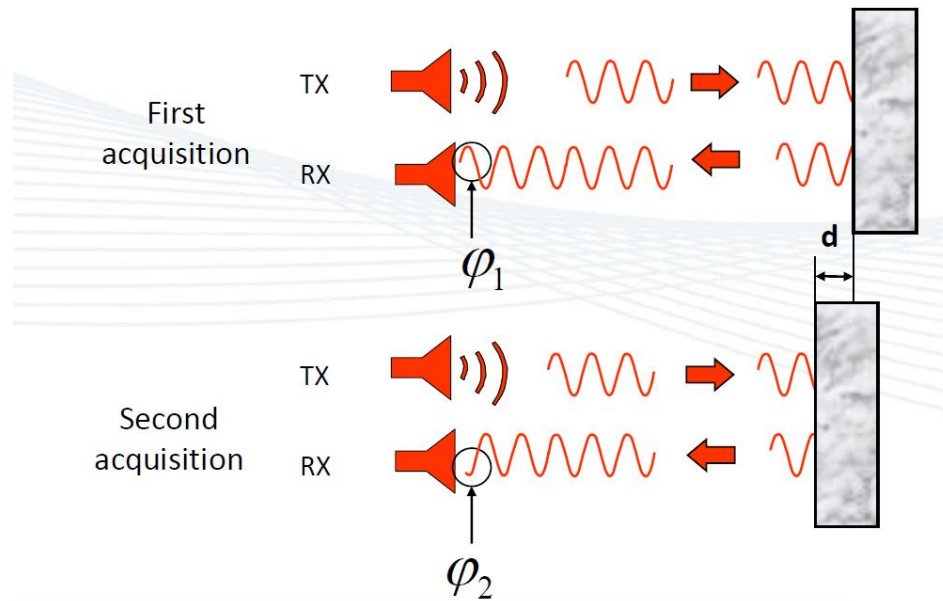


Figure 9, Principle of interferometry (Coppi, 2011)

Another error prone factor exists with changing atmospheric conditions at the investigation site. As the images are taken during slightly different climatic conditions, the changing diffraction index influences the propagation velocity of the electromagnetic waves (Rödelsperger, 2011). Mainly humidity, temperature and atmospheric pressure introduce errors to the measured phase (Rödelsperger, 2011). As a result the measured phase difference $\Delta\varphi$ does not resemble the true phase difference $\Delta\varphi_r$, as the atmospheric phase contribution $\Delta\varphi_{atm}$, the phase ambiguity $\Delta\varphi_n$ and noise $\Delta\varphi_{noise}$ have to be considered (Equation 8) (Jungner, 2009, Kurka, 2012).

$$\Delta\varphi = \Delta\varphi_r + \Delta\varphi_{atm} + \Delta\varphi_n + \Delta\varphi_{noise} \quad (8)$$

To resolve most of the atmospheric influence IBIS Guardian uses different atmospheric models, which are embedded within the evaluation software IBIS Guardian and offer only an approximation for discerning complex atmospheric effects. (Schaes, 2012). As atmospheric influence affects the entire radar image to the same degree, persistent or permanent scatterer deliver a coherent phase signal to discriminate between atmospheric pseudo displacement and real displacement.

2.1.2 Permanent Scatterer

One of the most challenging aspects for radar based measurements is the correct handling of atmospheric artifacts. To resolve atmospheric influence the permanent scatterer (PS) approach is introduced, which originates from space-borne radar campaigns (Rödelsperger, 2011). Using the complete phase information of highly time-coherent permanent scatterers, the accuracy of the entire measurement is pushed within the sub-mm range (Colesanti et al., 2003). The basic principle of this technique relies on the estimation of displacement, morphology, atmosphere and other disturbing parameters via certain stable permanent scatterers (Rödelsperger, 2011). Usually the analysis of obtained interferograms delivers this sort of information. Due to the highly changing conditions for space-borne SAR various techniques using similar approaches have been developed and summarized via the term Persistent Scatterer Interferometry (PSI) (Rödelsperger, 2011).

Atmospheric artifacts are usually spatially correlated within one radar acquisition and highly diverse in time (Colesanti et al., 2003). On the contrary displacement normally shows a strong correlation in time and a more complicated spatial correlation depending on the failure or movement mechanism (Ferretti et al., 2000, Colesanti et al., 2003). Assuming that certain pixels remain stable within time in terms of displacement during multiple SAR images, the atmospheric effect can be estimated using these referencing pixels (Ferretti et al., 2000). The calculated displacement is then corrected by subtracting the atmospheric artifacts.

2.1.3 Corner Reflectors

Environments with a closed cover of vegetation may produce problems in terms of target reflectivity and signal power (Rödelsperger, 2011). As a result the accuracy drops significantly and measurements are normally confined to non-vegetated areas. To resolve this limitation, artificial reflectors (e.g. corner reflectors) can be mounted within the investigation site. Accessibility to the site has to be given to allow an installation.

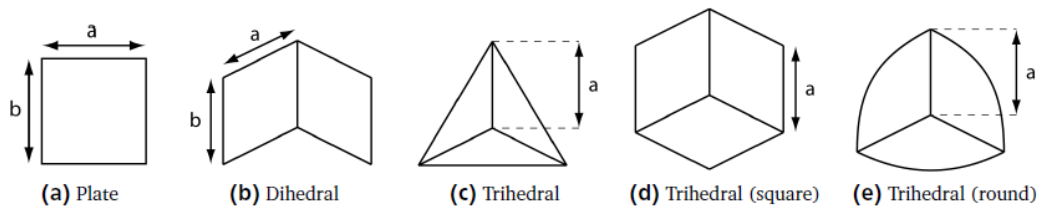


Figure 10, Different types of radar reflectors (Rödelsperger, 2011)

Different radar reflectors are shown in Figure 10, whereby trihedral reflectors show the best reflecting properties and the most tolerance for inaccurate adjustment (Rödelsperger, 2011). Due to their metal surface a distinctive amplitude signal is received, which theoretically allows the clear distinction from all other surrounding reflected signals.

2.2 IBIS-FL

In this thesis further research was realized with the apparatus IBIS-FL (Image by Interferometric Survey - Landslide; Figure 11), manufactured by the company IDS (Ingegneria dei Sistem S.p.A.; www.idscorporation.com), which is commercially available in similar form since 2006 (Mazzanti, 2011). The used equipment had the technical prerequisites for an upgrade to the next generation of IBIS scanner, the so called IBIS-FL version. This upgrade comprises faster acquisition intervals and therefore less atmospheric influence during one measurement (IDS, 2013). Anyhow this advantage could not be used during half of the measurement campaigns due to a missing software update, which was finally executed on May 2nd 2013. Up to this date measurements were executed using the former IBIS-L version, which resembles the IBIS-FL version in all properties, except the scan time.

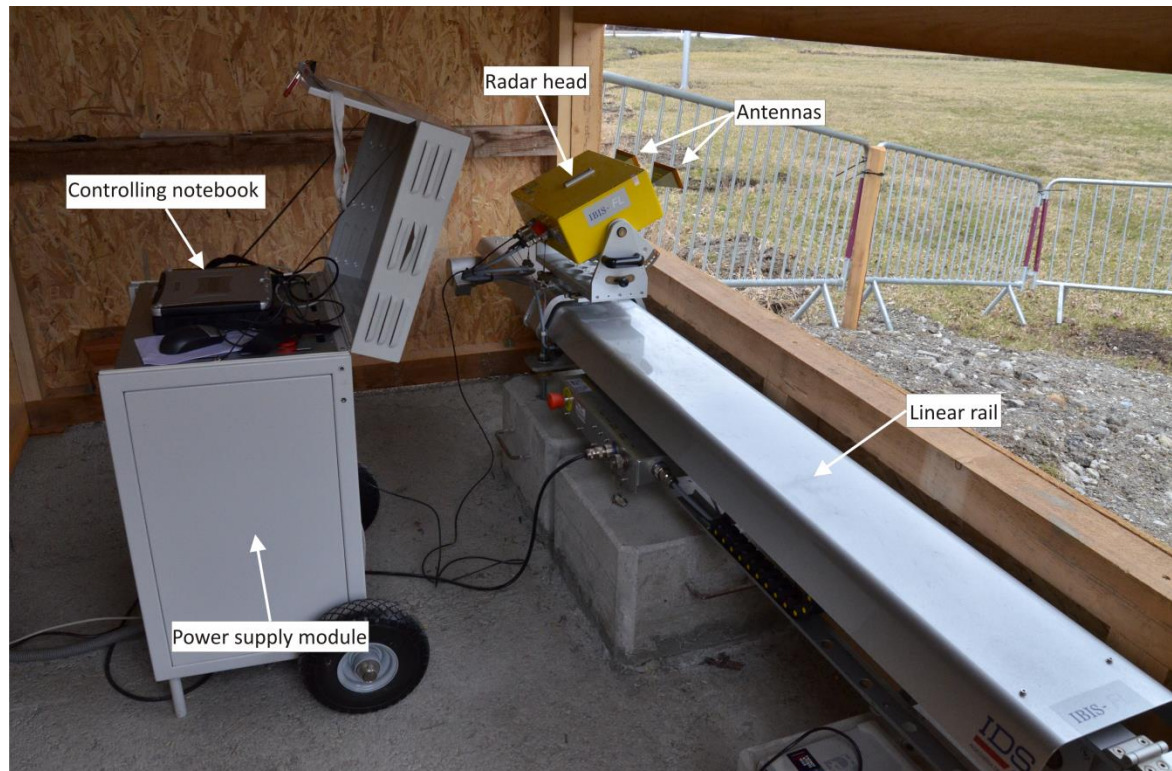


Figure 11, IBIS-FL equipment mounted on a concrete foundation in Bad Hofgastein

IBIS-L/IBIS-FL is a linear Ground-Based Interferometric Synthetic Aperture Radar which is composed of a radar head, a 2.5m long linear rail with an effective path length of 2m, a power supply module and a controlling notebook. The rail has to be mounted on a stable foundation like a concrete block. The radar head is mounted on a trolley, which is moving continuously along the rail. Two antennas transmit and receive radar waves with a frequency ranging from 17.1GHz to 17.3GHz (IDS, 2012). The sensor can be tilted to obtain the best fitting viewing angle.

The instrument is controlled with a laptop computer. After every measurement, which takes approximately 2.5min or 5-10min, depending on the maximum range and the software version (IBIS-L/IBIS-FL), one file with the extension *gbd* is stored on the local hard disk. The file size depends on the chosen maximum range and resolution and averages around 10-30 MB. By the use of a 3G modem, data transmitting is enabled, but only for already processed *psv* files (70-100 KB) to keep the transmitted data volume as low as possible. This processing step requires the prior creation of a mask in the field, as this step is only applicable on the *gbd* files.

All descriptive properties (Table 1) resemble both the IBIS-L and IBIS-FL version and most of the measurements were performed using Version 01.03.002 of the evaluation software IBIS-Guardian and the controlling software IBIS Controller (IDS, 2012).

Table 1, Technical specifications of IBIS-L/IBIS-FL; modified after (IDS, 2012, IDS, 2013)

Parameter	Value
Frequency f	17.1 - 17.3GHz
Central Wavelength λ	17.44mm
Bandwidth B	200MHz
Scan time Δt (IBIS-L)	5 – 10min
Scan time Δt (IBIS-FL)	2.5min
Scan length L	2m
Maximum distance R_{max}	4000m
Range Resolution ΔR	0.75m
Cross-range resolution $\Delta \vartheta$	4.4mrad (4.4m @ 1000m range)
Antenna type	IBIS-ANT6 (beamwidth of 50° horizontal and 20° vertical)

2.2.1 Advantages and Disadvantages

IBIS-L/IBIS-FL has several advantageous properties as well as some limitations (Rödelsperger, 2011, IDS, 2013, Schares, 2012).

Advantages:

- As a remote sensing technique with a maximum range of 4km, possibly dangerous or inaccessible sites can be monitored without the prior installation of reflectors.
- High accuracy and spatial resolution due to the use of radar waves. All targets within the radar beam are monitored simultaneously with an accuracy of 0.1 to 1mm.
- Independent of weather and daylight conditions, monitoring is continuously possible during the night and during limited visibility (e.g. fog, clouds or rain).

Moreover, IBIS-FL performs measurements, once initiated, automatically without the need of human intervention.

- In contrary to space-borne SAR IBIS-L/IBIS-FL has full control of the spatial baseline and is therefore perfectly suitable for displacement measurements.
- Due to continuous monitoring a high sampling rate is achieved, with measurements taking place every 2.5min and 5-10min, respectively. A high sampling rate enables real-time monitoring of possible displacements.

Limitations:

- IBIS-L/IBIS-FL infrastructure requirements are significant: a stable foundation, a power supply and a protective housing.
- Vegetation reduces the reflectivity and therefore the accuracy of targets significantly. Additionally grass, bushes or trees are subject to possible movement due to changing climatic conditions (e.g. wind and rain). Artificial reflectors (e.g. corner reflectors) or highly reflecting areas (e.g. rock walls, debris or concrete) are required to achieve sufficient coherence of measurements.
- Atmospheric delay can reduce the accuracy. During rapidly changing weather conditions or long term monitoring, the introduction of stable reference points or exact weather data is necessary.
- Phase ambiguity may disable the identification of the correct phase. Additionally rock fall activities or other fast moving processes may complicate the phase identification.

2.3 IBIS Controller

Using the IBIS Controller software configurations for the acquisition of radar images are implemented. Mainly information regarding the maximum distance (<4km), the range resolution (0.75m) and the antenna type have to be specified. Additionally, the synthetic aperture can be specified. Any value below the maximum synthetic aperture of 2m decreases the cross-range resolution of 4.4mrad, simultaneously the scan time is reduced. An average scan time of 7min may be expected for IBIS-L. For the most recent software version of IBIS-FL scanning times around 2.5min are realized. With a shorter

acquisition time the atmospheric influence during one measurement decreases considerably leading to a more accurate measurement result (IDS, 2013).

Measurements are stored as *gbd* raw files which require 10-30MB memory capacity. To accelerate data transfer and processing of the data, a selection mask defines investigated area and applies filtering thresholds. After this processing step the masked files are stored in the *psv* format with a file size of 70-100KB.

2.3.1 Masking

For the creation of a valid selection mask at least two *gbd* files have to be processed to generate three different radar maps (Figure 12). Due to the temporal deviation of the measurements the coherence map delivers a very useful map of the stability of all pixels in every image (Figure 12c and Figure 12d). Moreover, a general power map (dB) (Figure 12a) and a signal to noise ratio (SNR) map (Figure 12b) of the reflected signal are created. Generally non-vegetated areas (e.g. rock, debris, concrete) provide a strong and stable signal, whereas trees and bushes show high noise values (Rödelsperger, 2011).

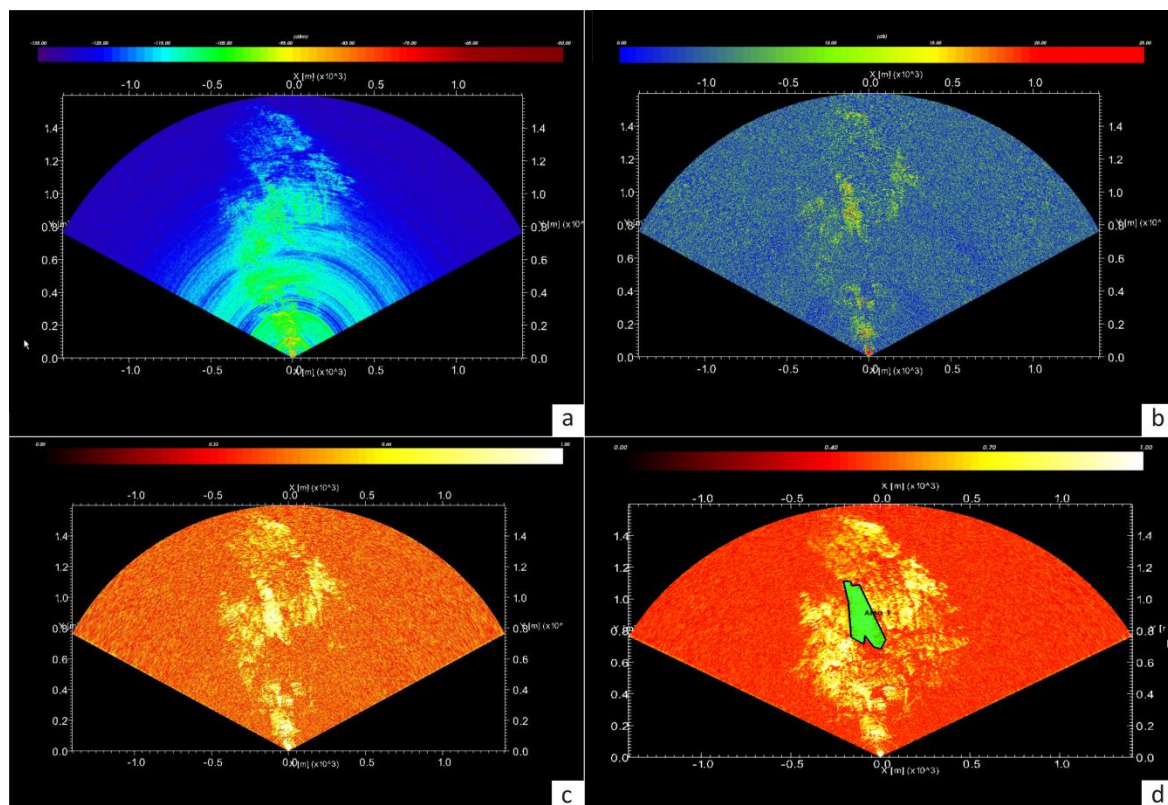


Figure 12, Power map (a); Signal to noise ratio (SNR) map (b); Coherence map (c); Selection mask (green) applied onto the coherence map of the Ingelsberg investigation (d). Bright areas indicate highly coherent pixels and represent rocky or sparsely vegetated areas.

After the introduction of an adequate mask, *gbd* raw files are processed into *psv* files, which are then transferred to the Department of Applied Geosciences in Graz. The *psv* files include the masked area and the excluded area is only stored within the *gbd* files. Collected measurement data is then imported into IBIS Guardian for further processing and visualization.

2.4 IBIS Evaluation Software

IDS provides two different approaches to process measurement data. First of all IBIS Data Viewer (IBIS-DV) allows a basic calculation of displacement maps. The advantage of this software is the possibility of inserting Ground Control Points (GCP), which act as a reference to the occurred displacement to remove atmospheric noise. However IBIS Data Viewer does not allow visualization of the processed displacement maps onto a digital terrain model (DTM). In contrast to this basic approach, IBIS Guardian enables a more advanced processing of displacement maps with the advantage of visualization with a geo-referenced DTM.

2.4.1 IBIS Guardian

IDS developed IBIS Guardian to allow a quick analysis of the acquired radar data. Many advantages arise with this intention, but the software remains a 'black box' in terms of used algorithms or applied atmospheric corrections. IBIS Guardian was used for the main part of the processing due to its straightforward approach. Hence a short overview of its functions will be given here.

IBIS Guardian has its advantages with calculating displacement maps visualized on 3D-terrain models. Using airborne laser scan data a DTM was selected and transformed to a resolution of 1x1m. Within the DTM options the position and northing (viewing direction in degrees deviating from north) of the IBIS radar are inserted to provide a precise overlay of displacement data onto the DTM. After choosing the previously defined selection mask all acquired *psv* files are processed and displayed as maps with different

information. IBIS Guardian calculates a displacement map, using interferograms of all radar images, a velocity map, which simply indicates the speed at which displacement occurred, and an amplitude map with the power of the signal. Moreover, pixels and areas can be selected and investigated using their time series. Generated time series are simply exported as .txt file for further correlation with other data (e.g. meteorological data). One week of data with a measurement interval of 7 minutes requires several hours for processing using a customary computer (e.g. Intel Core i7 and 8GB RAM).

3. Hornbergl Study Site

3.1 Regional Setting

The Hornbergl study area is situated within the Ausserfern in Tyrol, Austria, near to the town of Reutte (Figure 13). The Hornbergl is located directly west of the village of Höfen. The study area is bordered by the Murenbach and the Herrenbach to the North and the South, respectively.



Figure 13, Location of the Hornbergl study area within Austria, Scale 1:2 000 000 (BEV, 2013)

With an elevation of 1755m above sea level the Hornbergl is not a very dominant peak in this area. The steep rock wall beneath the '*Höfener Kreuz*' (Figure 15 & Figure 14), which is directly located on the peak of the Hornbergl, and the almost vertical cliff along the south-east striking ridge were investigated by means of the GBInSAR. The south-east striking ridge reaches from the peak of the Hornbergl down to an elevation of 900m above sea level. Confined by the Murenbach and Herrenbach the ridge forms slopes with a gradient of up to 40° to the South and the East (Moser et al., 2009), whereas its boundary to the North is an almost vertical cliff. In Figure 15 the investigated area is highlighted with a white line, moreover, repeatedly mentioned areas are marked by arrows.

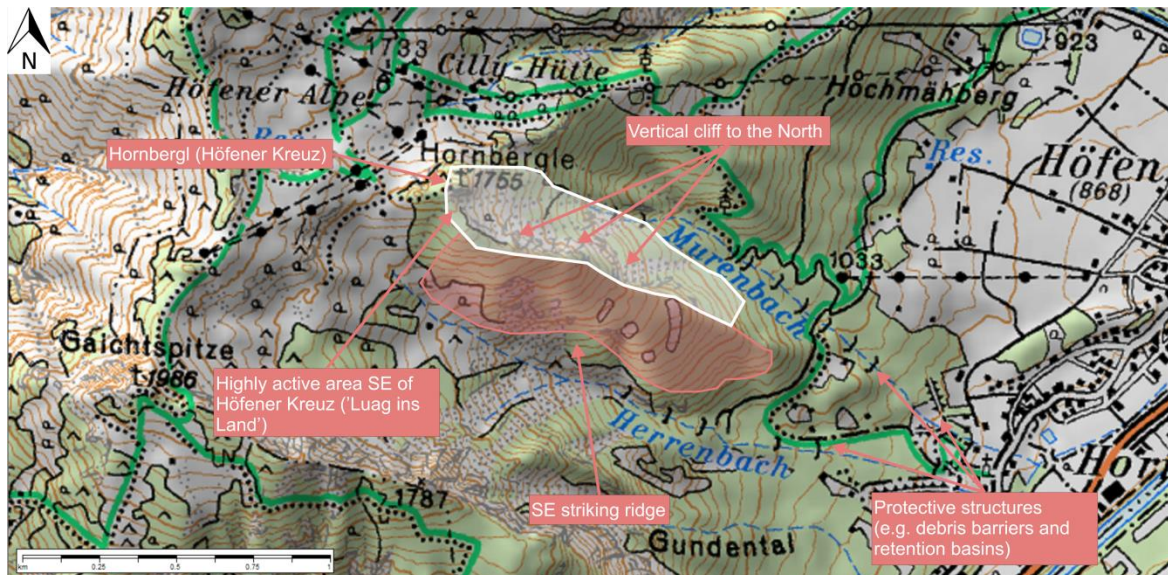


Figure 15, Hornbergl study area indicated with white shading, Scale 1:50 000 (BEV, 2006)

The study area has a temperate climate with a relatively high yearly precipitation of 1411mm in the reference period between 1981-2010 (ZAMG, 2013c). Due to the dominant influence of humid north-western weather in middle Europe, the Ausserfern area represents a geographic barrier enabling high amounts of rain and snow to fall (ZAMG, 2013c). Temperature ranges between monthly average -3°C in January and 16°C in July in the reference period of 1961-1990 (ZAMG, 2012).

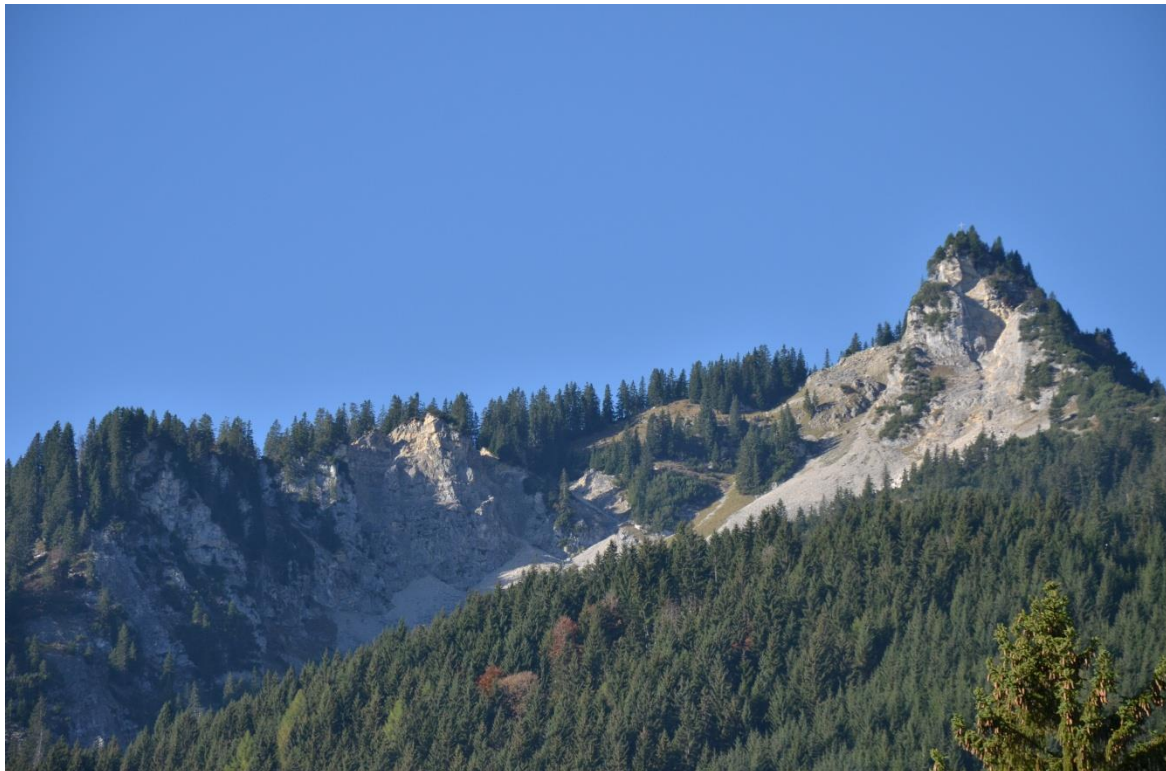


Figure 14, The Hornbergl seen from the valley (view looking SW). The ‚Höfener Kreuz‘ is located at the right edge, whereby the south-east striking ridge and its confining cliffs can be seen at the left.

The vegetation around the Hornbergl and the south-east striking ridge is dominated by spruces and mountain pines, which often display an inclined growth. Generally the study area doesn't enable significant land use, due to the steep terrain. At the lower end of Murenbach and Herrenbach agricultural land is situated.

According to the ZAMG (2013a) 14 earthquakes per year on average are noticeable in Tyrol. The area around Reutte is situated within seismic risk zone 3 (Figure 16), where major damages to buildings may occur (ZAMG, 2013a).

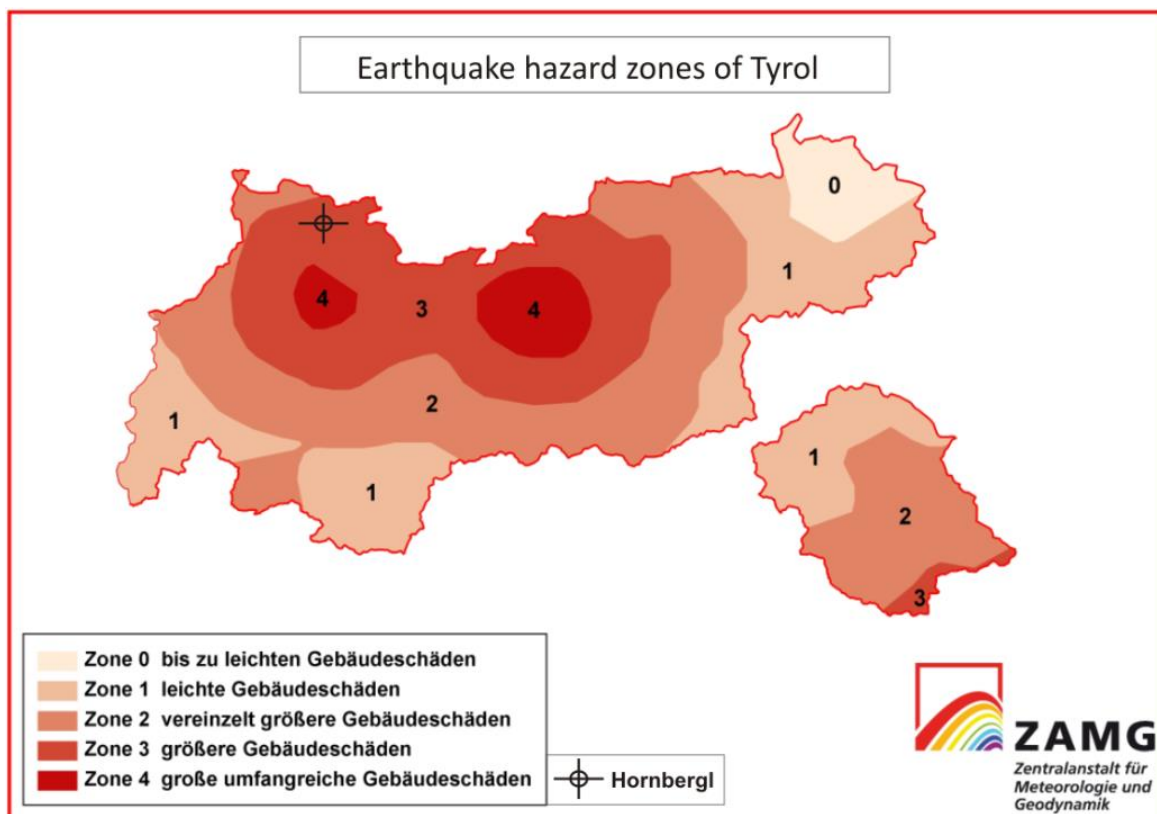


Figure 16, Earthquake hazard map of Tyrol (ZAMG, 2013a)

The Hornbergl is part of the Northern Calcareous Alps, which are dominated by extensive nappes and foldings. In the Hornbergl area (Figure 17) rock units are built up by the Allgäunappe ('Allgäu-Decke') as footwall and by the Lechtalnappe ('Lechtal-Decke') as hanging wall (Tollmann and Deuticke, 1976b). As the Allgäunappe is not directly encountered in the investigation area of the Hornbergl, a more precise description of the single formations is only given for the Lechtalnappe.

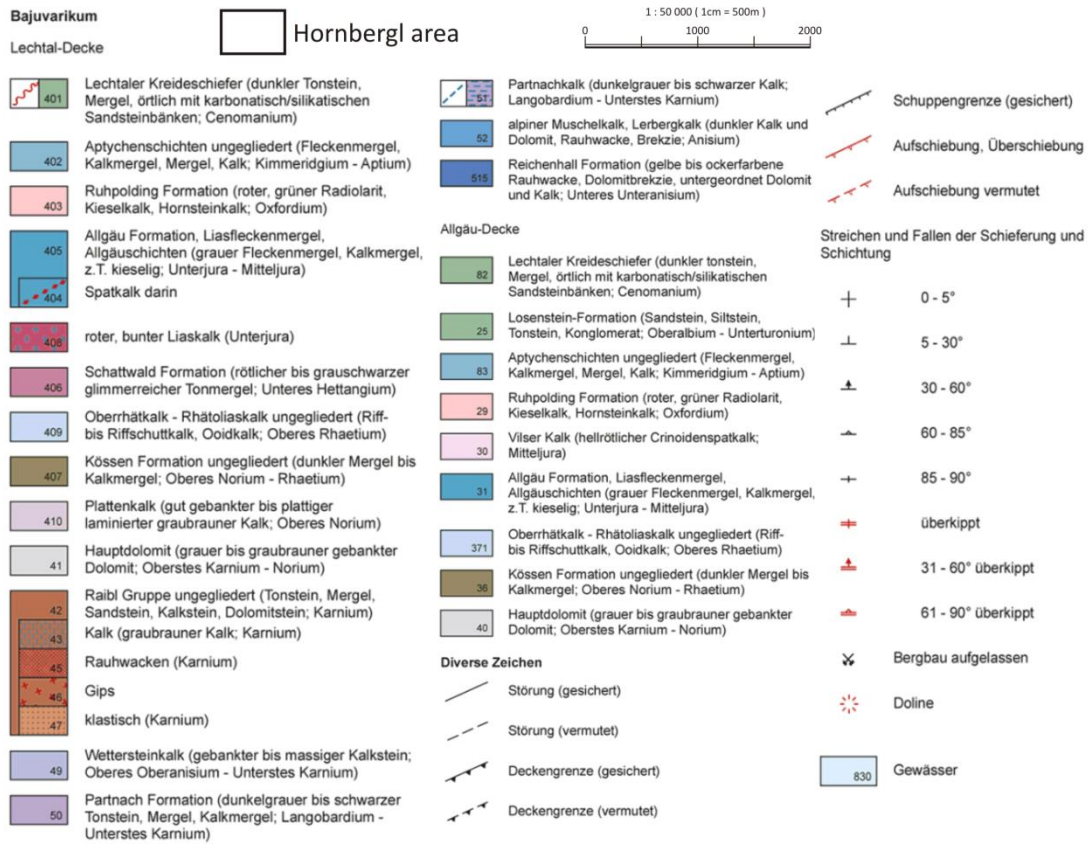
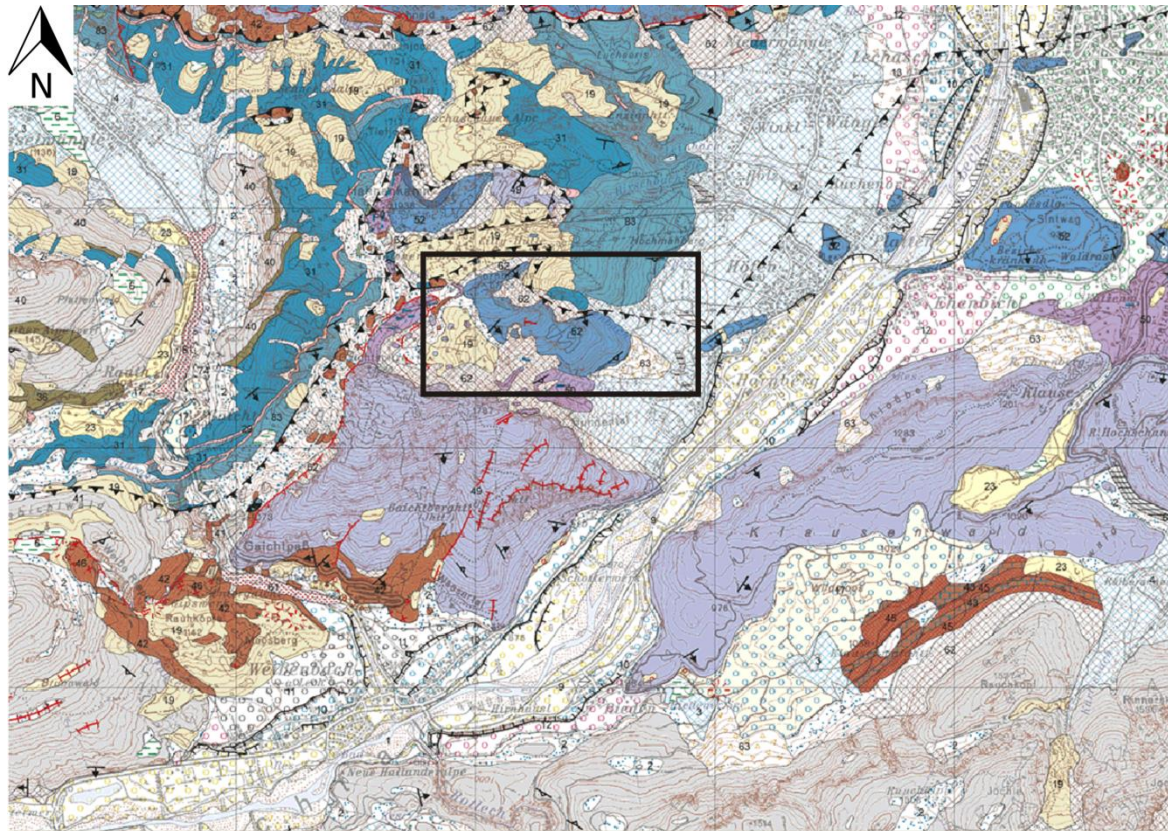


Figure 17, Regional geological map of the area around Reutte, Scale 1:50 000, modified after (GBA, 2009)

3.2 Site Conditions

At the base of the Lechtalnappe the '*Reichenhaller Schichten*' (Reichenhall formation) are forming the undermost layer of carbonatic Triassic with distinctive boundaries to the neighboring formations (Tollmann and Deuticke, 1976a). Built of calcareous, dolomitic, sandy or *rauhwacke* components it is thought to origin from a shallow inter to supratidale depositional milieu (Tollmann and Deuticke, 1976a). Due to the alternating sequences of trans- and regressional phases saliniferous and evaporitic interlayers were built (Moser et al., 2009). The formations overlying the Reichenhall formation are summarized as '*Alpine Muschelkalk Gruppe*' (Alpine shell limestone unit), whereby a more exact subdivision would be, from a stratigraphical point of view, lower to higher, Virgloria formation, Steinalm formation and Reifling formation (Kirschner, 2006). These three layers all consist of alternating layers of limestone and marly interbeds (Figure 18), with partly bioturbatic Micrites (Kirschner, 2006). The Virgloria formation shows



Figure 18, Typical alternating layers of limestone and marly interbeds of the '*Alpine Muschelkalk Gruppe*'

centimeter thick beds, whereby the Steinalm formation builds up decimeter thick beds (Kirschner, 2006). The Reifling formation is highly distinctive due to its main component the '*Reiflinger Knollenkalk*' or Reifling nodular limestone. Consisting of light greyish to light brownish rather thin beds of limestone, it always shows a typical undulating and nodular surface (Tollmann and Deuticke, 1976a). The alpine shell limestone unit dominates the appearance of the Hornbergl (Figure 19), especially on the steep slope to the Murenbach where there are near-vertical cliffs up to 130m height. The overlying Partnach formation is marked by an increase in marl and thicker interbeds, respectively. Simultaneously a decrease of the carbonatic content is observable (Kirschner, 2006).

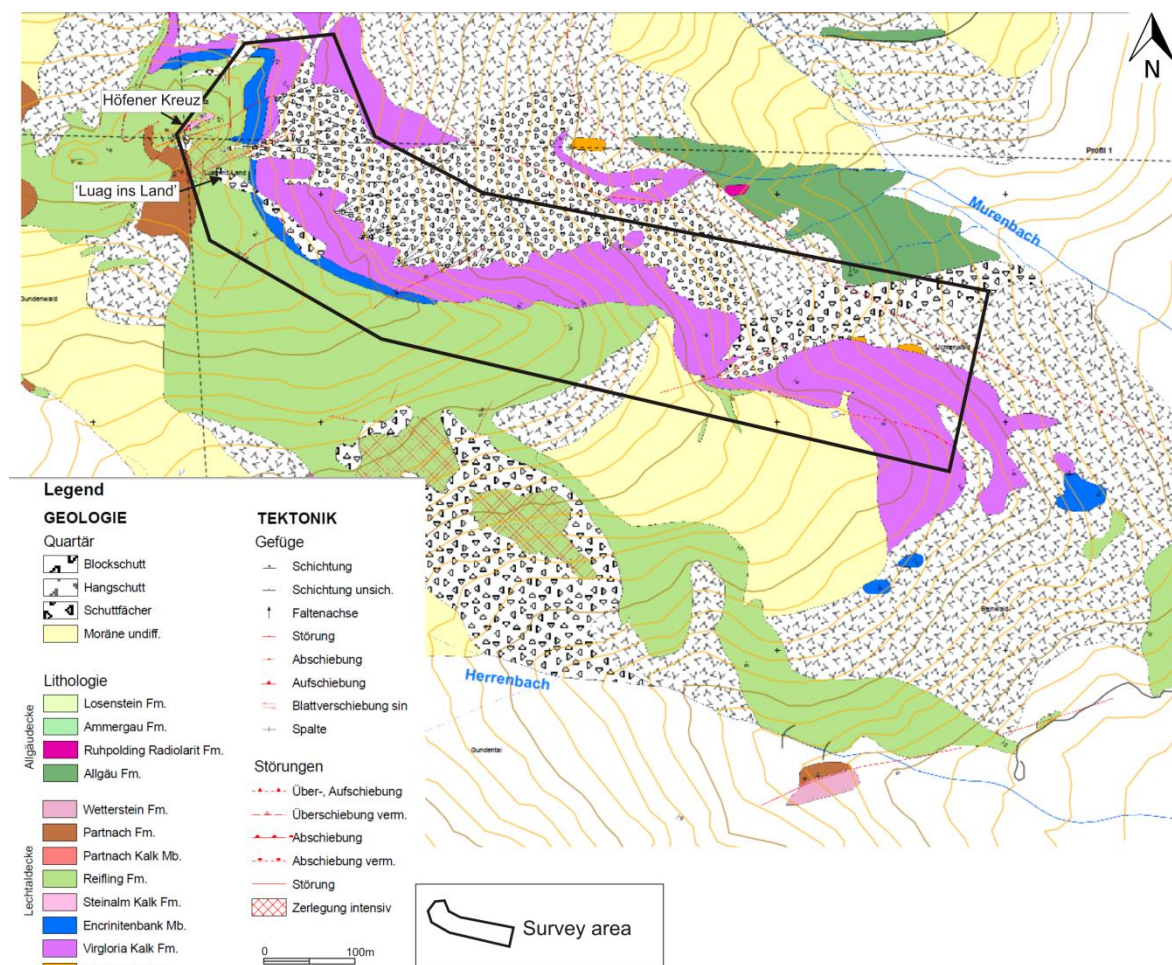


Figure 19, Geological site map of the Hornbergl, Scale 1:500, modified after (Kirschner, 2006)

According to Moser et al. (2009) light grey and almost white limestone mylonites are detectable at an elevation of 1355m, which are highly deformed. These mylonites, situated along the thrust fault of Lechtalnappe and Allgäunappe, are a distinctive zone of weakness (Moser et al., 2009).

Several landslide events testify the instability of the Hornbergl (Marschallinger et al., 2010, Moser et al., 2009). The tectonical influence and the unstable geological structures form a setting with an exceptionally high number of debris flows, rock falls and rock slides (Meier et al., 2009). According to Moser et al. (2009) all measured slope displacement is mainly taking place within the upper layers of the alpine shell limestone unit ('*Alpine Muschelkalk Gruppe*'). With a general dipping of $40^\circ - 55^\circ$ to SSE the limestone beds are striking almost parallel to the slope dipping in direction to the Herrenbach (Moser et al., 2009). Moreover, they are characterized by intercalated marl layers with a thickness of only a few centimeters (Meier et al., 2009). Two different joint sets cut through the limestone layers, orientated almost perpendicular to the bedding surfaces (Meier et al., 2009).

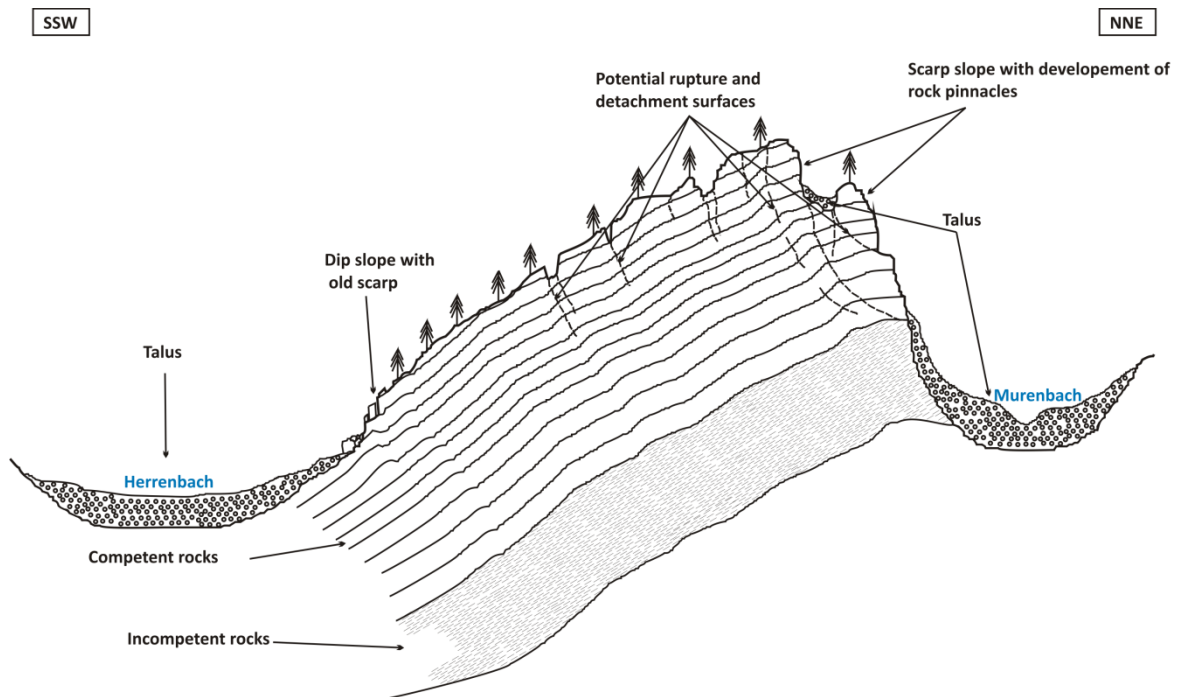


Figure 20, Schematic profile along the south-east striking ridge at the Hornbergl; this general model includes the development of rock slides along the bedding planes at the dip slope. On the contrary the formation of rock pinnacles at the scarp slope and the formation of graben-like structures at the ridge are implied. 'Competent rocks' refer to the limestone layers of the alpine shell limestone unit, 'Incompetent rocks' to the Reichenhall formation; modified after (Kirschner, 2006, Meier et al., 2009)

To gain a more detailed and illustrated knowledge about the Hornbergl a field investigation was carried out in October 2012. The starting point of the investigation was the '*Höfener Kreuz*' at the top of the Hornbergl, whereby the main focus was put on the southeast striking ridge and the small talus at the point '*Luag ins Land*' between the ridge and the '*Höfener Kreuz*'.

At the point *'Luag ins Land'* as well as along the south-east striking ridge the effects of instability were visible in the morphology and the vegetation. For instance several cracks in the uppermost vegetation layer with elongated and disrupted roots were found. Along the south-east striking ridge heavily tilted trees are another potential indicator for past movement. The most obvious features are the deep cracks (>4m depth) and holes in the vegetation, extending into the underlying limestone layers (Figure 21). Especially on the rim of the south-east striking ridge crack widths could be observed from decimeter size to several tens of meters. Partially cracks evolve into graben like structures, where the vertical displacements may reach several meters. In direction to the Murenbach cracks with a length of several tens of meters generated a slightly stepped morphology. Additionally freestanding rock pinnacles were observed at the escarpment of the south-east striking ridge towards the Murenbach (Figure 21).



Figure 21, Freestanding rock pinnacle on top of the ridge; 5m deep crack along the ridge

3.3 Historical Landsliding & Mitigation Measures

In the case of the Hornbergl the two bordering torrents Herrenbach and Murenbach are very active and are the main 'carrier' for the rock fall and debris material. According to Moser et al. (2009) the Hornbergl has suffered several rock fall events in the past, which include (Dragosits, 1996):

- Debris flow along the Herrenbach in 1975
- Rock fall in 1976, with a volume of approximately 100.000 m³ along the Herrenbach
- Several smaller-scale debris flows in 1982 with an estimated volume of 40.000 m³ [according to Albrecht (1999) in (Meier et al., 2009)]
- Several debris flows from May 2.-5. 1986, along the Murenbach with an estimated volume of 60.000 m³. These events devastated 4 hectares of agricultural land (Figure 22)



Figure 22, Result of the debris flow of May 2.-5. 1986 (Photograph taken by Dr. Dragosits in 1986, WLV, Ausserfern)

Due to its history of instability the 'Austrian Service for Torrent and Avalanche Control' (WLV) has constructed mitigation measures to prevent a major damage to inhabited areas along the lower part of the Murenbach. Starting at an elevation of around 1400m

above sea level several check dams have been constructed along the brook bed until the beginning of the first settlements down in the valley at an elevation of 900m above sea level. At the downstream end of the Murenbach a retention basin has been constructed to mitigate debris flow impacts. Between 1967 and 2006 the carried out protection measures have cost approximately 14 million Euro (Marschallinger et al., 2010).

3.4 Previous Survey Campaigns

Since 1987 relative extensometer measurements were carried out across main fissures and moving areas, additionally absolute geodetic measurements determined displacement rates and directions (Moser et al., 2009). Furthermore a GNSS (Global Navigation Satellite System) was installed in 2007 by the Institute of Geodesy of the University of the Bundeswehr Munich (Glabsch et al., 2009). Additionally one week of GBInSAR measurements were carried out in September 2011 by the Technical University of Munich (Schaes, 2012).

Two distinctive areas of movement were mapped within previous investigations. In the area called '*Luag ins Land*', south-east of the '*Höfener Kreuz*' the highest rates of displacement were measured (Figure 23). According to Moser et al. (2009) several measurement campaigns showed displacement rates of $>20\text{cm/a}$. This part either reflects deep seated movements or a shallow sliding of blocks on marly layers, anyhow it is difficult to clarify by now (Moser et al., 2009).

The other distinctive area of movement developed along the south-east striking ridge (Figure 23). Confined by the steep cliffs to the NE and the steepening slopes to its south, graben like structures formed in this area with a length of up to 100m. Forming these massive cracks, filled with tilted trees and loose blocks, a toppling of pinnacles in direction of the Murenbach destabilizes the ridge at velocities of $5\text{-}10\text{cm/a}$ (Moser et al., 2009). That notwithstanding a significant trend of the movements in direction of the Herrenbach was observed within all implemented measurements (Moser et al., 2009).

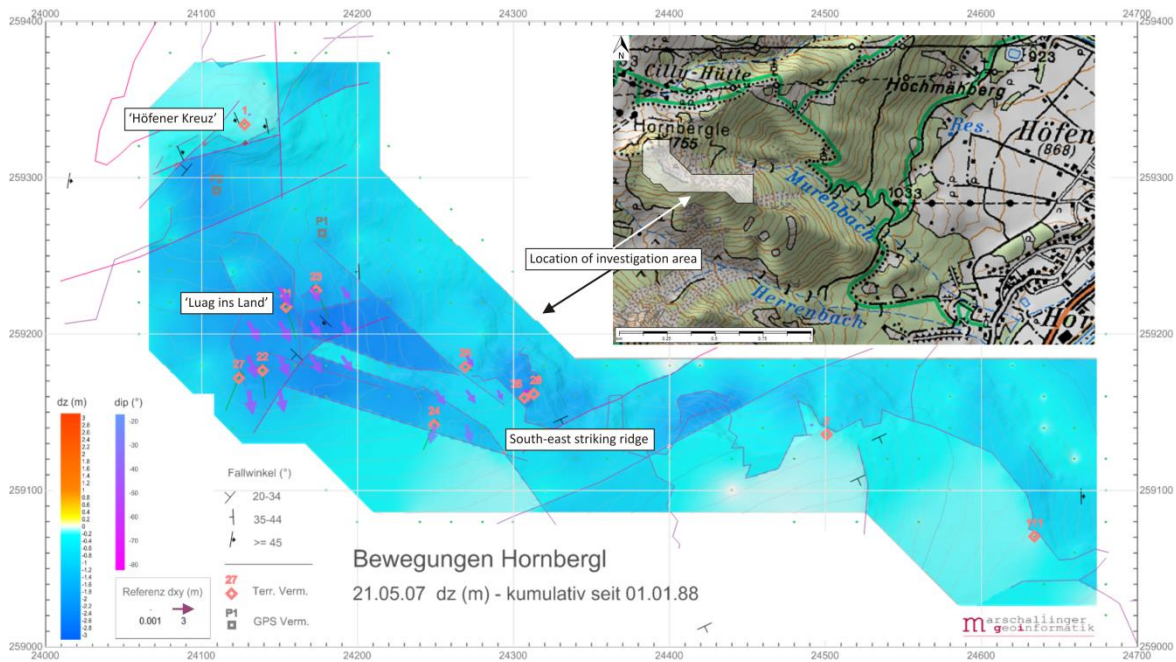


Figure 23, Cumulative displacement between 01.01.1988 – 21.05.2007; Arrows indicate direction and dip (purple colors) of movement; Colors indicate interpolated vertical displacement between +3m (red) and -3m (blue), modified after (Marschallinger et al., 2010)

A clearly visible trend in faster movements was shown during snowmelt in spring and early summer (Glabsch et al., 2009, Schubäck, 2009). On the contrary movement rates stabilize during cold winter months.

4. Ingelsberg Study Site

4.1 Regional Setting

The Ingelsberg is situated in the Gastein valley in Salzburg at the north-eastern end of the village Bad Hofgastein (Figure 24). The site can be divided into a bedrock part in the upper area, starting at 1446m above sea level continuing with a debris talus down to 1072m above sea level and a vegetated area, reaching down to the valley floor at 872m above sea level. The slope gradient averages in the upper area at 45°, whereby the lower vegetated area flattens to averaged 30°. With an elevation of 1446m above sea level it is not a dominant peak in this area, though the Ingelsberg remains a well-known mountain due to its historical instability (Wilhelmstötter, 2013).



Figure 24, Location of the Ingelsberg study area within Austria, Scale 1: 1 000 000, (BEV, 2013)

The site belongs to the temperate climate zone and is highly influenced by humid north-western weather (ZAMG, 2013c). Due to its proximity to the main alpine ridge to the South, acting as a meteorological divide, a relatively high amount of yearly rain days (139 days) leads to an average precipitation of 1162mm per year in the reference period of 1981-2010 (ZAMG, 2013b). Monthly temperature average -3°C in January and 15°C in July during the reference period of 1961-1990 (ZAMG, 2012).

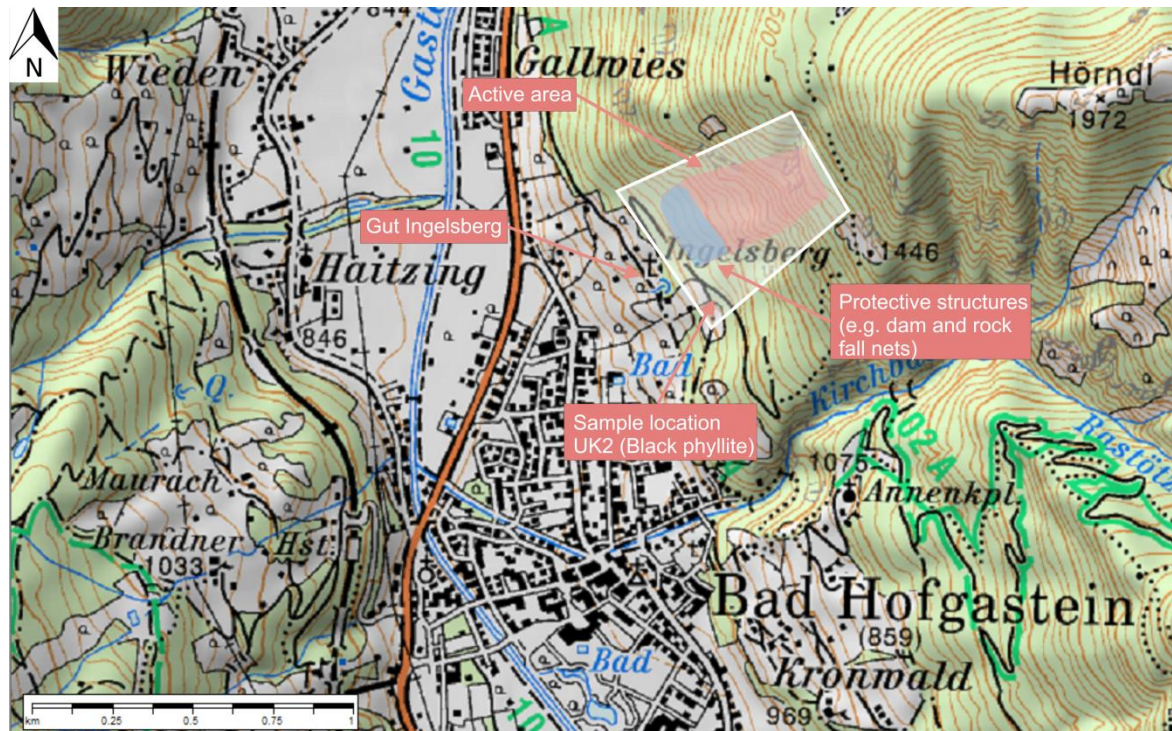


Figure 25, Ingelsberg study area indicated with white shading, Scale 1:50 000 (BEV, 2006)

The study area is mainly vegetated with spruces and larches, though most unstable parts remain without a cover of vegetation (Figure 26). The bordering areas to the South display heavily crooked or tilted trees and partly stretched roots along major cracks. In the lower part of the study area meadows dominate. In Figure 26 a general overview of the investigation site is given.



Figure 26, The Ingelsberg, seen from the Gastein valley and the position of the radar (view looking E). The framed area shows the unstable area and the encircled parts represent interpreted previously detached blocks.

Situated within the Tauern window, the Gastein valley consists of several geological units (Figure 27). A general differentiation includes Penninic, Sub-Penninic, Helvetic and Austroalpine nappes, whereby the Ingelsberg is only located in Penninic units (Schmid et al., 2004). The Penninic units can be subdivided into *'Matreier Schuppenzone und Nordrahmenzone'* (Matrei zone) and the *'Glockner-Deckensystem'* (Glockner nappe), (Figure 27). The surrounding area of Bad Hofgastein includes only units of the Glockner nappe as the transition to the Matrei zone is situated further to the north close to the village of Dorfgastein (Pestal et al., 2009).

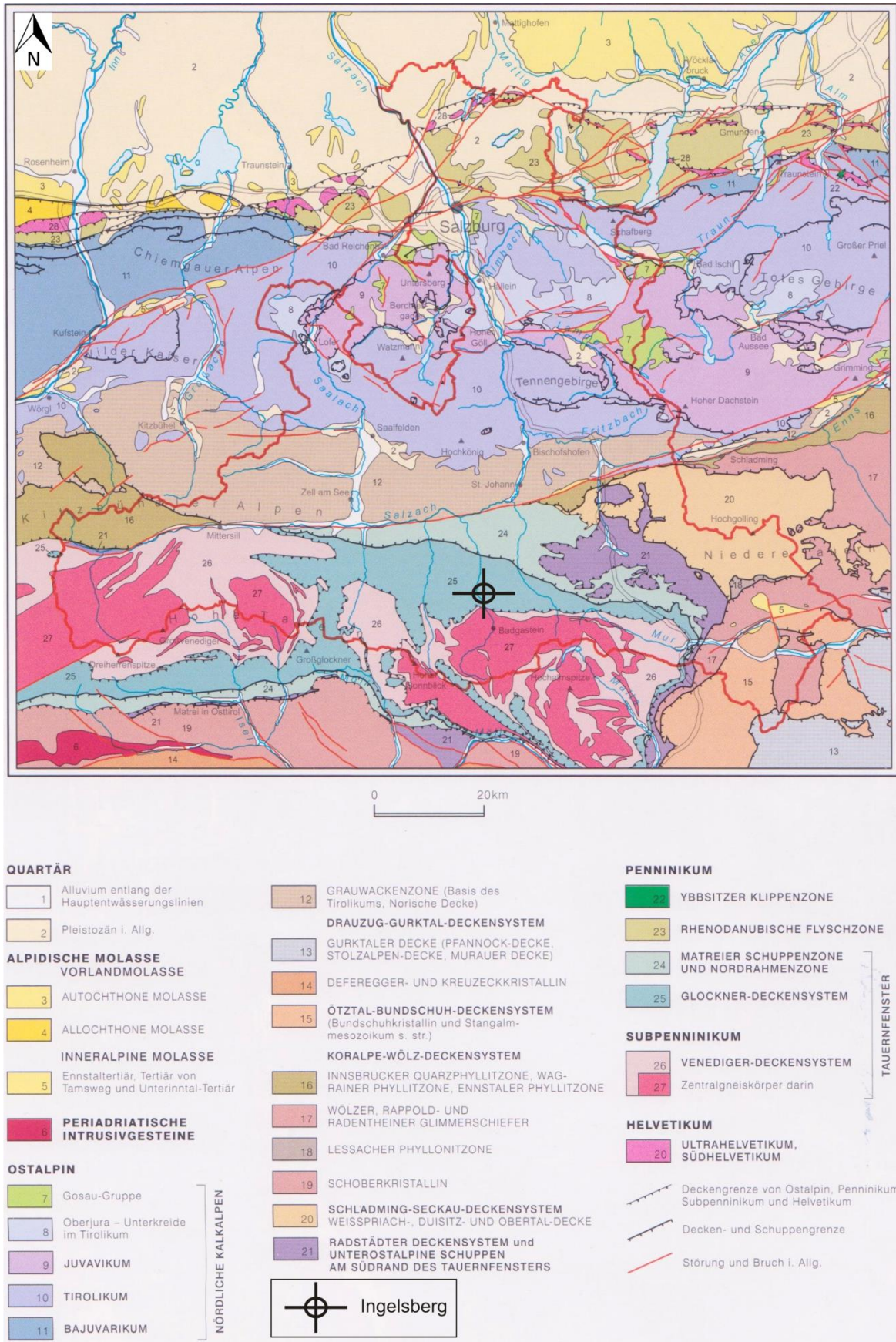


Figure 27, Tectonic overview of Salzburg, Scale 1:1 000 000, modified after (Pestal et al., 2009)

The seismic risk within the federal state of Salzburg is classified as low, with averaged three noticeable earthquakes per year (ZAMG, 2013a). Bad Hofgastein and its surrounding areas are located within a seismic risk zone with the possibility of slight damages to buildings (ZAMG, 2013a).

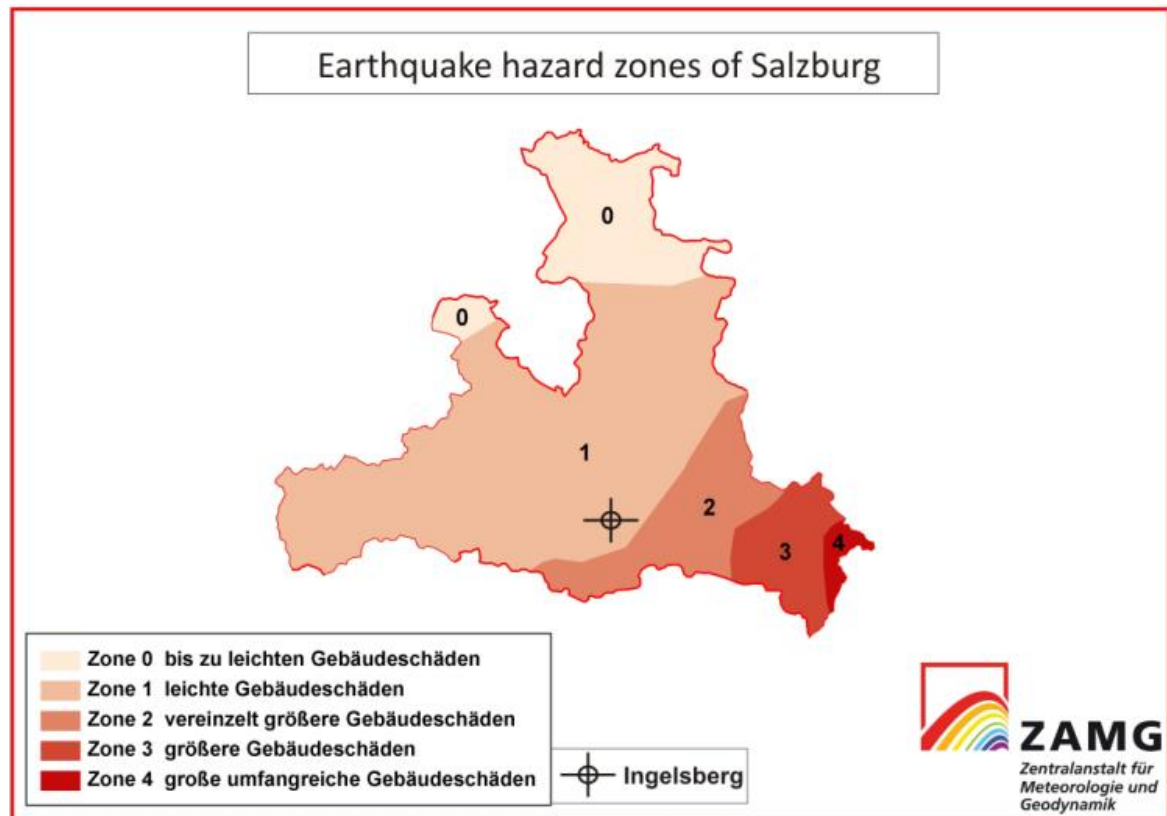


Figure 28, Earthquake hazard map of Salzburg (ZAMG, 2013a)

4.2 Site Conditions

According to the geological map of Salzburg and its annotations (Pestal et al., 2009) the Glockner nappe consists mainly of metamorphic products of marly, clayey and calcareous sediments, which were deposited on oceanic or distal continental crust (Schmid et al., 2004). These units show a cretaceous depositional age and experienced metamorphism during the alpine orogeny. As a result predominantly calc-mica schist, black phyllite, and a metabasic unit comprised of amphibolite and greenschist can be distinguished in the field. The units are summarized via the collective term '*Bündnerschiefer*' (Schmid et al., 2004). A more detailed description of these three dominating rock units follows:

- The black phyllites are either encountered with or without a small content of limestone and sometimes contain quartzite or breccia. As precursor dark clays with sandy input are assumed, which were deposited in the abyssal parts of the Penninic ocean (Pestal et al., 2009). In the lower area of the Ingelsberg these black phyllites form the base for the overlying calc-mica schist and the unit of greenschists and amphibolites, which will be summarized as metabasic unit (*'Grüngesteine'*). The black phyllites in the study area display heavily weathered surfaces and can mostly be broken by hand. Therefore, strongly eroded black phyllites provide a distinctive zone of weakness at the base of the Ingelsberg (Wilhelmstötter, 2013).

Due to its possible influence on the instability of the Ingelsberg a more detailed mineralogical analysis of the black phyllites was executed. Therefore, four exemplary samples were taken at a road cut along the access road of the dam (Figure 25). All samples were powdered and investigated, using XRD (X-ray diffraction) to gain an overview of the mineralogical composition. Figure 29 displays an X-ray diffraction pattern with the detected peaks and the according

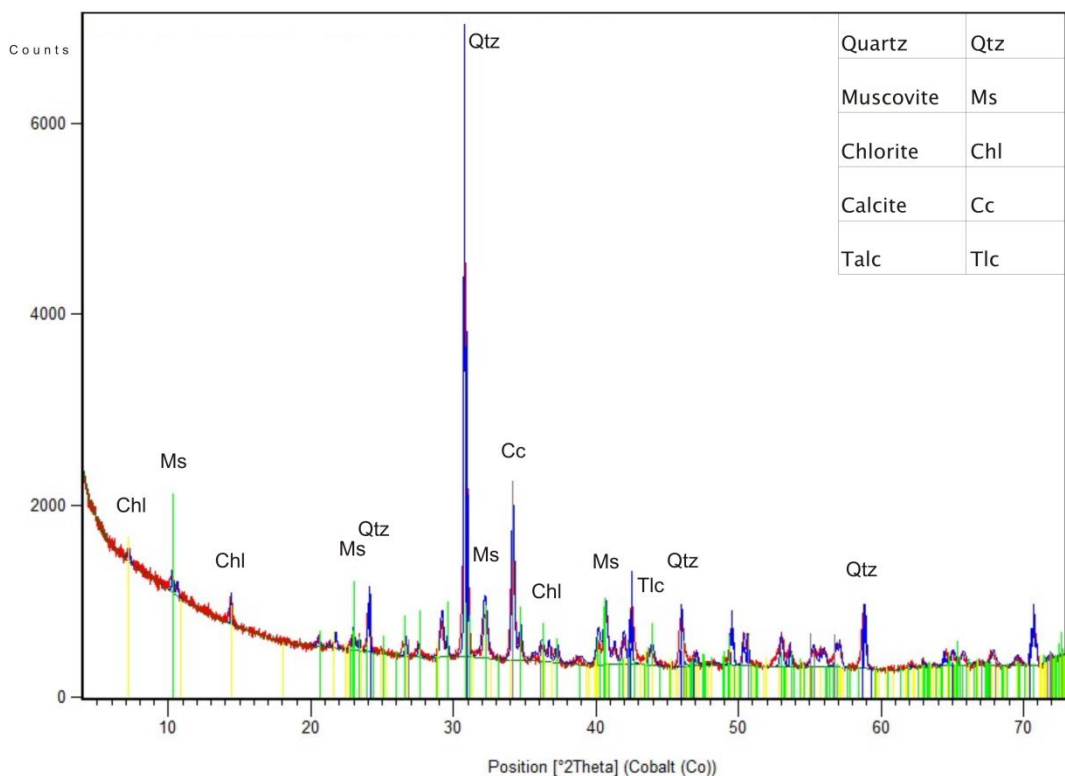


Figure 29, XRD analysis of a black phyllite sample (UK2). Minerals identified: Quartz, Muscovite, Chlorite, Calcite and Talc. Axis *Counts* refers to intensity of detected backscattered signal and *2Theta* position refers to the interplanar distance d [Å].

minerals. Quartz, muscovite and chlorite were identified in all samples, whereupon calcite was only found in one sample, which was taken close to neighboring calc-mica schist. Additionally talc was found in the samples, which delivers, together with chlorite and muscovite, an explanation for the 'greasy' feel.

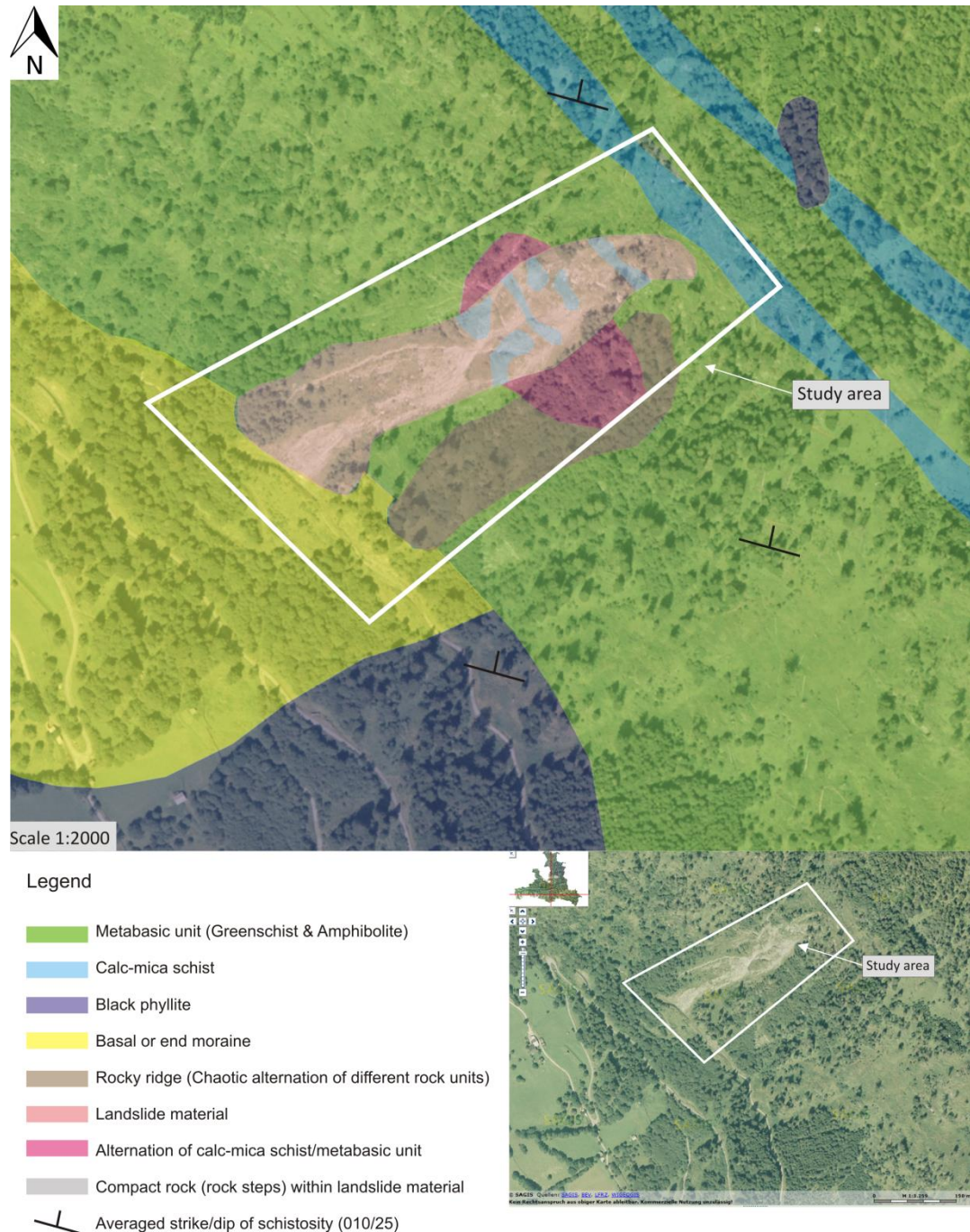


Figure 30, Geological site map of the Ingelsberg, Scale 1:2000, modified after (Wilhelmstötter, 2013)

- The calc-mica schists (*‘Kalkglimmerschiefer’*) overlie the black phyllites alternating with the metabasic unit (Figure 30). Mainly composed of calcite, mica and quartz,

the calc-mica schists outcrop with a light brown color when slightly weathered, or with a grey to blue-grey color when freshly exhibited. These schists mainly originate from arenitic calcareous ooze, which was deposited onto the edge of the continental shelf in the Penninic ocean (Pestal et al., 2009). Subsequently they got relocated and transported into the abyss onto the oceanic crust (Pestal et al., 2009).

- The metabasic unit (*'Grüngesteine'*) is mainly formed by amphibolites and greenschists, with a mineralogical main composition of feldspars, actinolite, epidote and chlorite (Pestal et al., 2009). Commonly this unit shows a fine grained texture and a high schistosity as well as a clearly distinctive light green to dark green color. Quartz nodules may stick out of the exposed and eroded parts of this unit (Pestal et al., 2009). Taken together, the metabasic unit and the calc-mica schist unit alternate on top of the black phyllites and build up most of the unstable area (Figure 30).

The Ingelsberg includes an alternating composition of black phyllite at the base and an overlying metabasic unit and calc-mica schist on top. The shallow exhibited layers of black phyllite and partly highly eroded calc-mica schist tend to show a horizontal and even downhill dipping angle, although strike and dip of all rock units averages at 010/25 for the schistosity (Wilhelmstötter, 2013). On top of the tilted black phyllite and calc-mica schist, intersecting joint sets form freestanding blocks. Therefore Wilhelmstötter (2013) proposed a *'hart auf weich'* scenario, as the phyllites form a soft deformable underground and the overlying units split into stiff unstable blocks. This failure mechanism is also supported by cracks, which are located along the head area at the top of the Ingelsberg. The cracks have dimensions up to 2m opening width and up to 80m in depth according to local speleologists (Wilhelmstötter, 2013).

4.3 Historical Landsliding & Mitigation Measures

The Ingelsberg near Bad Hofgastein experienced several rock fall events, dating back hundreds of years (Wilhelmstötter, 2013). With its first recorded event in 1774, the Ingelsberg has remained periodically active. Many rock fall events are documented and quoted within the archives of the '*Land Salzburg*' (Wilhelmstötter, 2013). The most significant recorded events include:

- 25.05. 1931: Detached block with a mass of 1500kg
- 10.05. 1987: Rock fall with block sizes up to 40m³ and a total volume of 3000 - 5000m³
- 21.-22.04. 2001: Several hundred cubic meters of rock fall are triggered by heavy rainfall
- 21.07. 2012: Several hundred cubic meters of rock are detached from the upper head area during rainfall

Due to its landslide activity in the past mitigation measures were made to prevent a major impact of rock falls on infrastructure and human life. Dams and rock fall guard nets have been raised at the end of the debris talus to retain detached material. Preventive blastings had been executed in the uppermost area of the study site to lower the probability of major rock falls (Wilhelmstötter, 2013). However, potentially hazardous blocks remain in this area due to the instability of the slope.

4.4 Previous Survey Campaigns

Five fissurometers and three remotely controlled cameras enable a real time monitoring, whereby an accuracy of tenths of millimeters is achieved by the fissurometers (GEODATA, 2008). Additionally total station measurements were carried out on six reflecting prisms (Figure 31) and on seven fixed control points (Wilhelmstötter, 2013).



Figure 31, Fixed reflecting prism at the upper part of the Ingelsberg; Installed fissurometer inside one of the major cracks at the top of the Ingelsberg

Three weatherproof cameras are installed as two close-ups, one at the head area of the Ingelsberg and one near the dam at the bottom of the unstable area (Figure 32). The third camera is mounted on a supermarket and delivers an overview of the entire investigation area. All cameras are equipped with LED-spots to provide day and night observation. The main purpose of the cameras is to evaluate possible alarms on their severity and to capture a set of images during rock fall events.



Figure 32, Image at the top left shows the upper head area; image at the top right shows the dam at the toe with accumulated debris; bottom image shows the entire investigation area; (Images taken on 29.04.2013)

5. Hornbergl GBInSAR Measurement Campaign

5.1 Instrument Setup

Successful GBInSAR monitoring requires a stable foundation and a secure mounting of the equipment. An existing concrete foundation of the measurement campaign of the Technical University of Munich was utilized at the Hornbergl (Schaes, 2012). Using a positioning and drilling template 5 holes were drilled and injected with resin to allow the installation of threaded studs for the mounting of the rail (Figure 33). Several nuts and washers provide for horizontal and secure mounting of the guiding rail (Figure 33).



Figure 33, Using the positioning template for drilling the holes; resin injected holes with fixed threaded studs and base washers; detail of the installed rail.

After installing the rail, the radar head is mounted onto the 'elevation pointing system' and a trolley, which moves along the rail (Figure 34). During this step adjustments regarding the height of the sensor and the general viewing angle can be implemented. Before initiating any measurements the supply unit and the radar must be connected with a USB cable for data transfer and a cable for power supply.



Figure 34, The tilted radar head mounted on the 'elevation pointing system' using several spacers for ideal positioning.

As IBIS-FL is only capable of measuring LoS (Line of Sight) displacements, the most favorable angle and position for the radar head must be determined. If the principal movement direction can not be estimated in advance, problems can arise with the interpretation of the measured data. Therefore it would be necessary to acquire exact knowledge about the geometry and the real movement direction of the investigated area to calculate the absolute displacement using a simple trigonometric approach. However, the easiest method to overcome this limitation is to find the best fitting position for the radar regarding the actual movement (Figure 35).

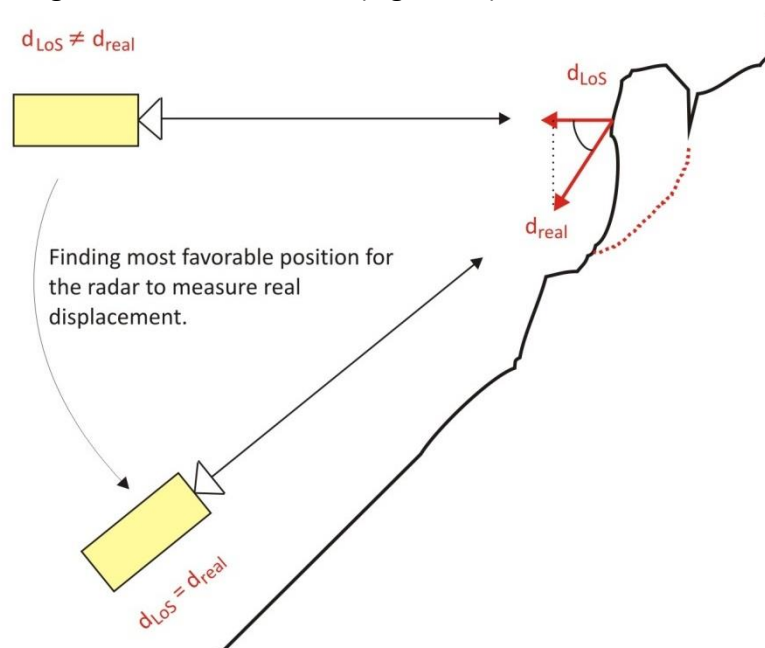


Figure 35, To avoid the measurement of LoS displacement the orientation of the radar beam must be aligned as accurately as possible to the direction of real displacement (d_{real}).

Concerning the Hornbergl the location of the radar foundation was already established by Schares (2012), who considered the directions of expected movement. According to Moser et al. (2009), Schuhbäck (2009) most of the displacement takes place in direction to the Herrenbach, which is approximately a movement away from the radar head and a positive value along the LoS. In contrast movement is also expected towards the radar, as several of the rock pinnacles and the area around the 'Höfener Kreuz' indicate movement towards the Murenbach (Moser et al., 2009). Movement onto the talus in the Murenbach would result in a negative value or a movement in direction of LoS of IBIS-FL. Considering these directions of movement the location is ideal in terms of view, expected displacement direction and power supply (Figure 36).

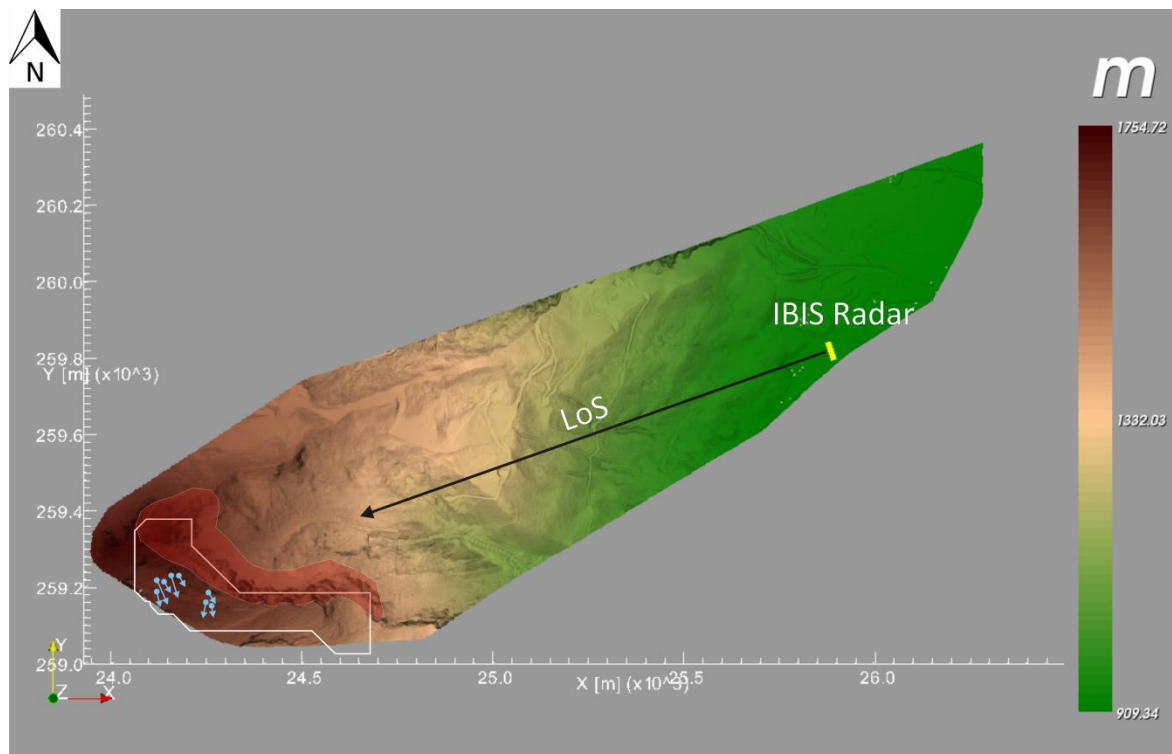


Figure 36, Position of the IBIS Radar next to Höfen for investigating the Hornbergl. Red shaded area refers to illuminated area; LoS resembles the direction of measurement. White line indicates area of previous measurement campaigns; arrows indicate previously measured direction of movement.

The GBInSAR equipment was set up on September 19th and 20th 2012, and monitoring continued until December 11th 2012. With a maximum measurement distance of approximately 2km and quickly changing weather the general conditions were not highly ideal in terms of coherence of the measurements. Additionally, densely vegetated areas within the investigated site hindered a comprehensive evaluation of the entire illuminated site. Furthermore short snowfall events in October and November interrupted measurements briefly.

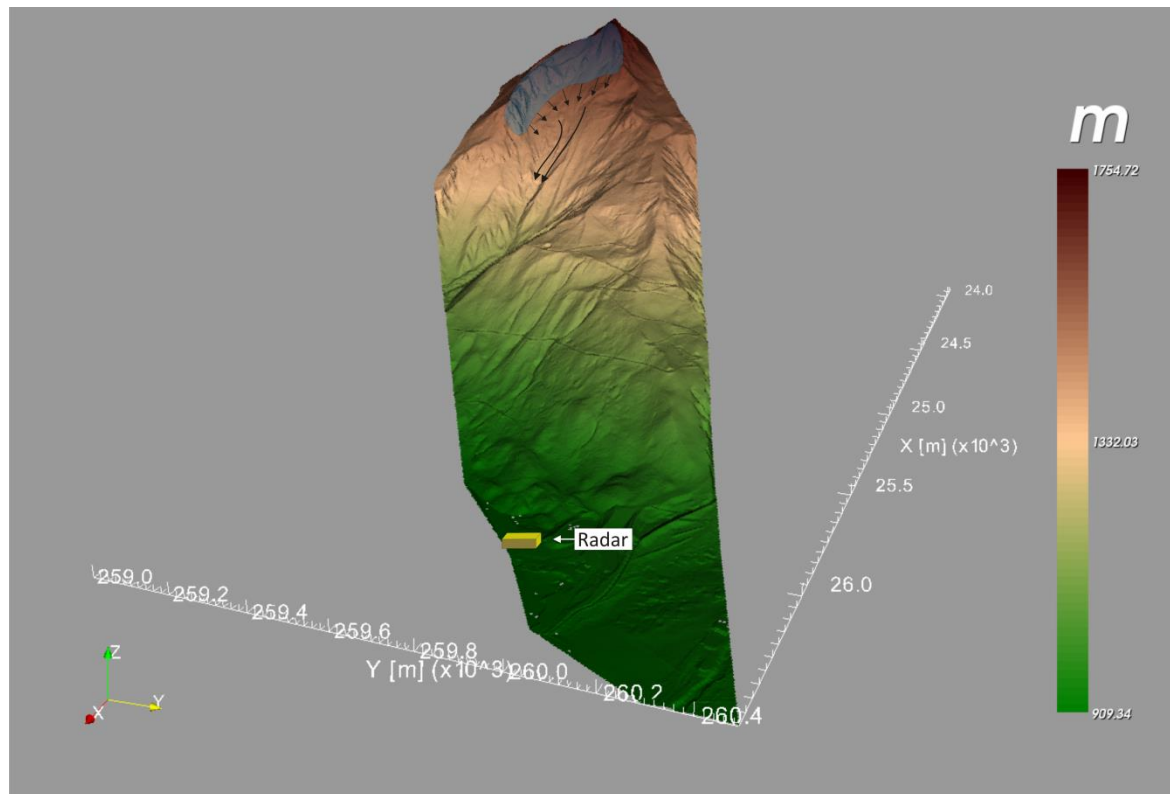


Figure 38, Investigated area projected on the used aerial laser scan DTM. Yellow box indicates position of the radar, arrows indicate possible direction of displacement and further transportation within the Murenbach (View looking SW).

Figure 37 displays the GBInSAR selection mask, which excludes heavily vegetated areas. The actual Hornbergl and its adjacent debris talus lie within the NW-Mask, whereas the SE-Mask covers the steep rock walls along south-east striking ridge. Depositional

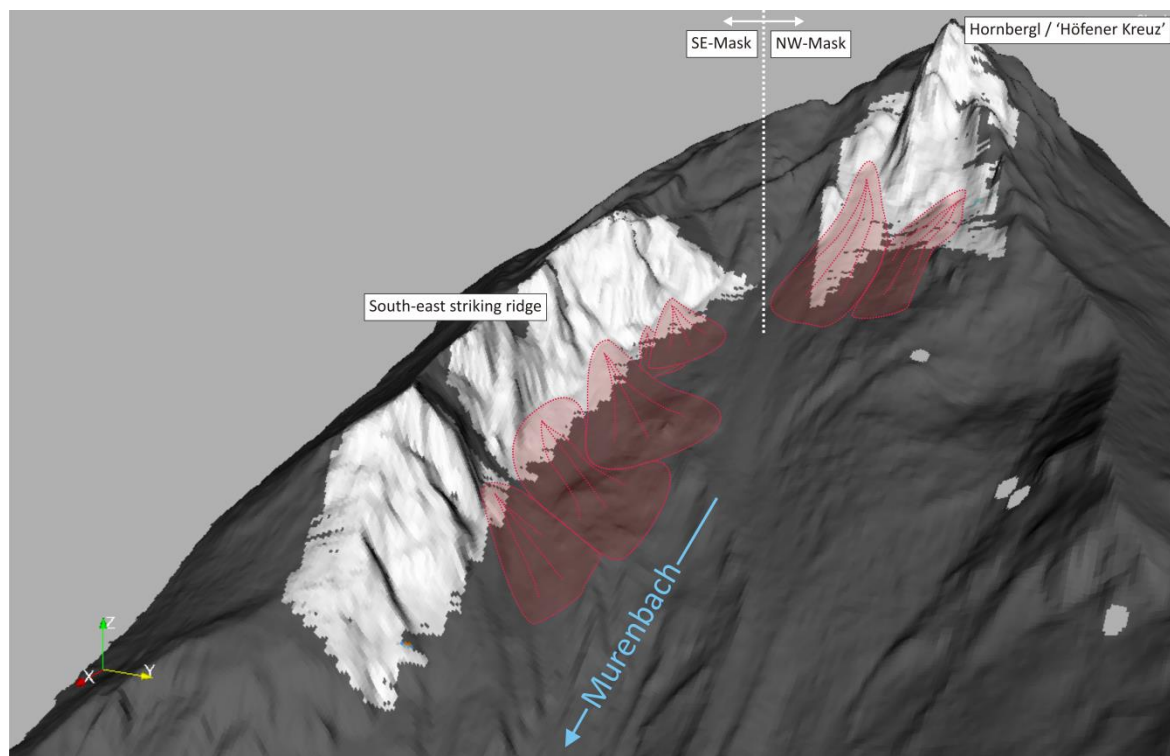


Figure 37, Overview of the masked area at the Hornbergl without any processed displacement. Red shaded areas indicate depositional areas/talus.

areas/talus at the toe of both masks are also included. The grey dots in the right foreground originate of the DTM cutting process and do not interfere with the measurements.

A correlation of measured displacements against precipitation enables an interpretation in terms of response time and impact. Generally speaking a distinctive effect of changing weather conditions has to be considered. Concerning the investigation of the Hornbergl one weather stations in the close proximity is suitable for delivering adequate meteorological data. Meteorological data was available from the 'Flugsportverein Reutte-Höfen', which runs a weather station at the bottom of the valley floor, 1km away from the position of the radar.



Figure 39, Completely installed IBIS-FL radar at Reutte within the equipment shelter.

5.2 Measurement Results

Repeatedly used scale bars range from 0mm (white) to -50mm or -100mm (red) and indicate a movement towards the radar in the LoS. Displacement in the opposite direction, away from the radar, was consciously neglected within most of the applied scale bars to provide a simpler presentation of monitoring data. Movements in direction

away from the radar (positive values) were considered and investigated, as prior investigations detected displacement in this direction. However, only exemplary radar images are shown including displacements in both directions (+100mm to -100mm).

The most evident displacement at the Hornbergl was measured within talus areas at the toe of the steep walls along the ridge, as well as at the major talus close to the actual Hornbergl (Figure 40). These unconsolidated deposits show a high sensitivity to rainfall events. Additionally displacement was detected at the toe of the Hornbergl and continued throughout the entire measurement campaign, showing distinctive events of movement. The steep rock walls generally showed a stable behavior, however, a small area of a few measurement pixels indicated displacement (Figure 40).

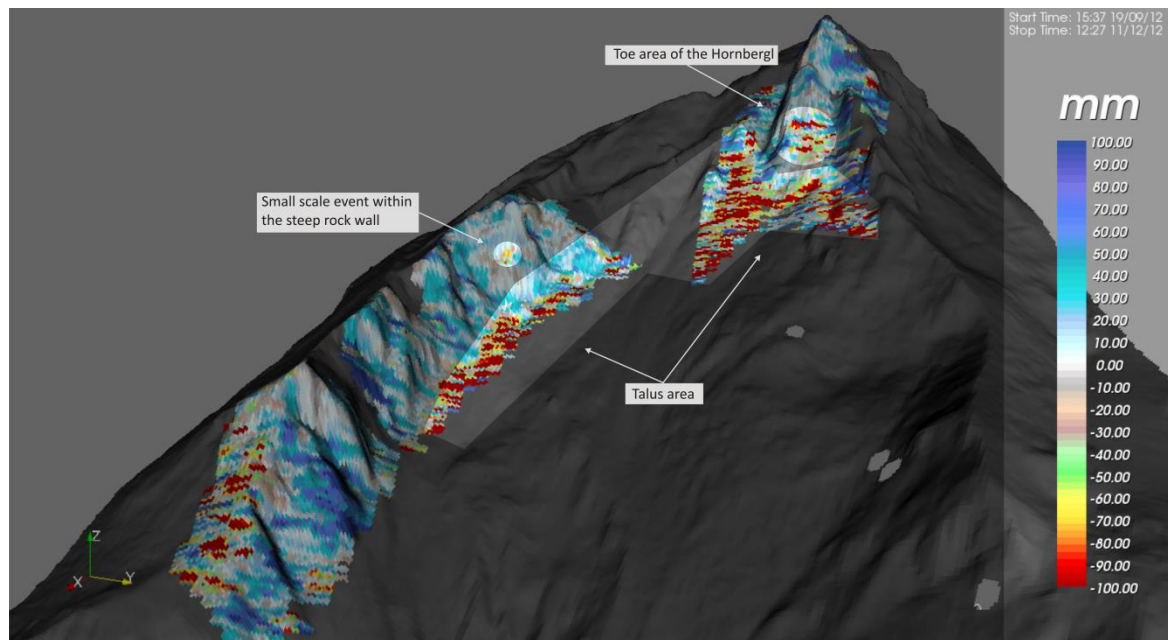


Figure 40, Location of repeatedly measured displacement at the Hornbergl. Displacement occurred within the talus and at the toe of the Hornbergl, as well as during a small-scale event within the steep rock walls. Image covers the complete duration of the measurement campaign (19.09. – 11.12.2012) and displays accumulated displacement over this time span. Displacement pixels in the lower left corner refer to a highly vegetated area and therefore lack a necessary reliability of acquired data.

A significant increase in detected movement occurred during the first ten days of December. The bottom graph in Figure 41 correlates a rainfall event on the 4th of December with the occurred displacement. In the beginning of December significant snowfall occurred. During dismounting of the GBInSAR equipment, approximately 1m of accumulated snow was observed close to the radar shelter. Snowfall and accumulated snow at the surface have an impact on radar measurements, as they both lower the coherence of measurements and cause pseudo-displacements (Rödelsperger, 2011).

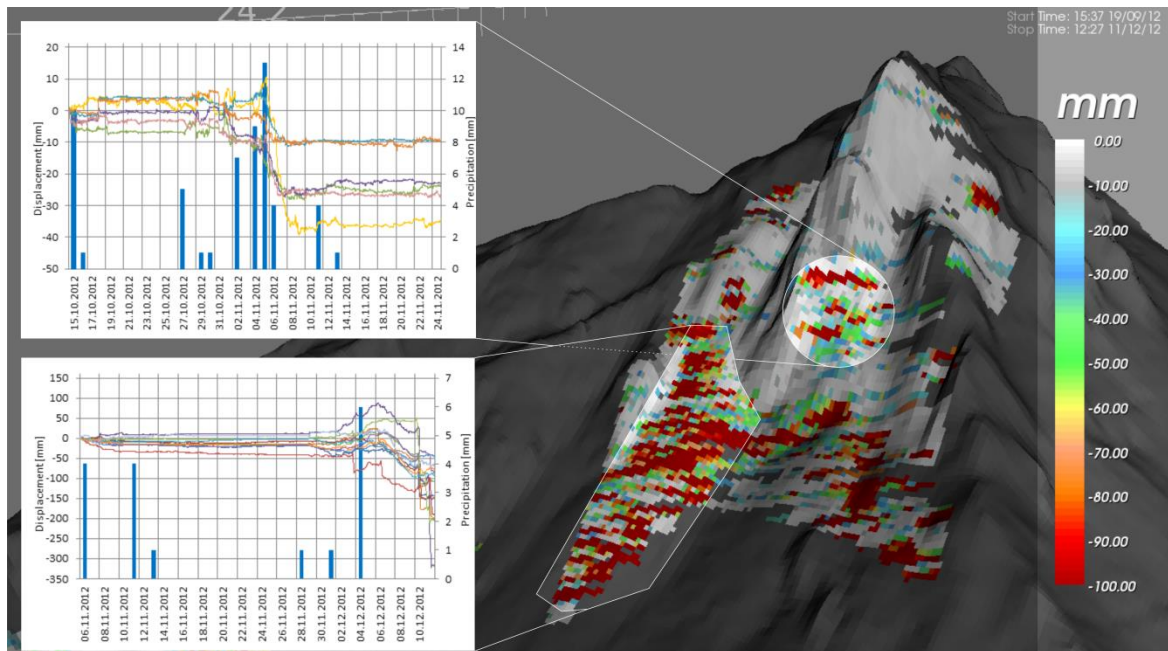


Figure 41, Characteristic example of measured displacement plotted against precipitation. Top graph refers to the toe area of the Hornbergl, bottom graph refers to the main talus at the Hornbergl. Both time series show strong correlation to measured rainfalls.

As displayed in the bottom graph in Figure 41 the talus of the Hornbergl showed displacement after a minor rainfall event in the beginning of December. The top graph in Figure 41 also shows the onset of talus displacement with rainfall during the first days of November. A quick stabilization of displacement after the rainfall is observable.

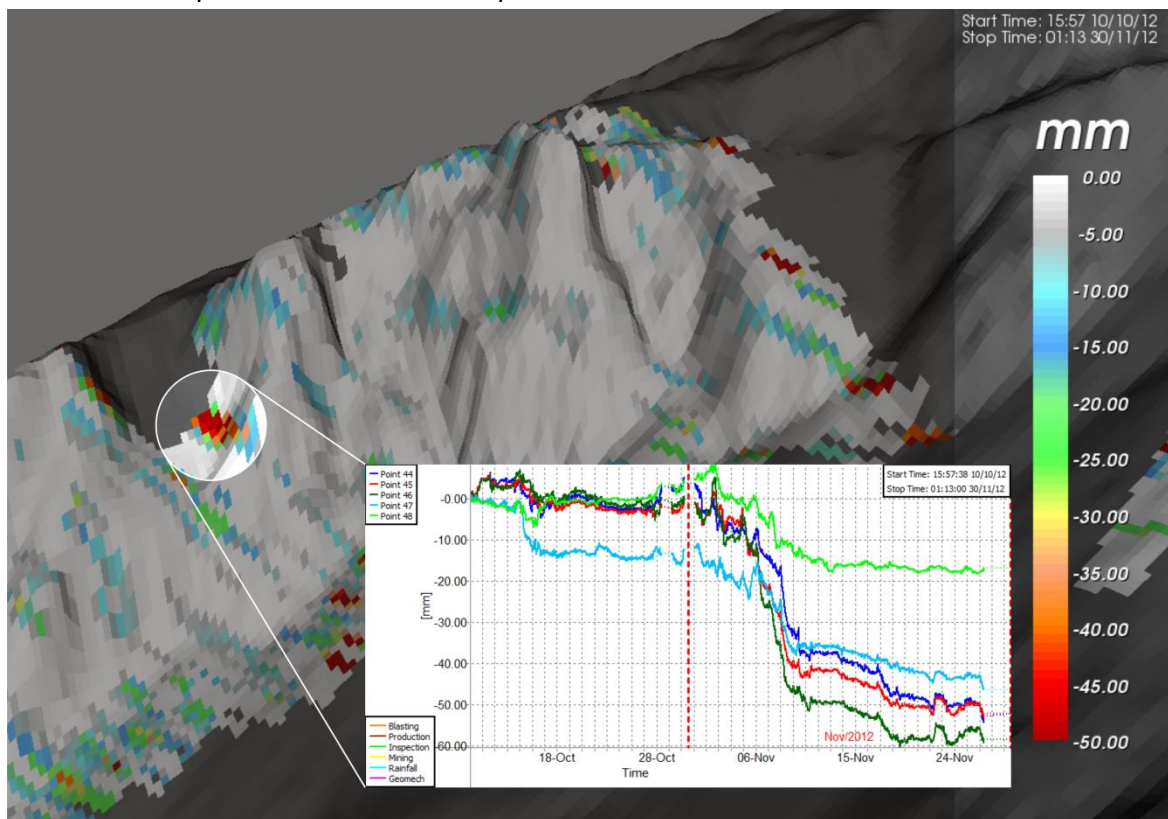


Figure 42, Characteristic small-scale example of measured displacement within a few pixels located at the steep confining wall along the south-east striking ridge. Displacement shows strong correlation with the rainfalls at the beginning of November.

Multiple small-scale events took place during the investigation. One of these distinctive events is displayed within Figure 42 as a characteristic example. Still, the dimension of one measurement pixel at this distance has to be considered (e.g. Pixel size@2km, 0.75m by 8.8m). The displacement time series shown in Figure 42 again state a clear correlation with precipitation in the beginning of November (30mm on 04./05.11.2012). Furthermore, the stable and non-moving wall areas can be seen in the background covered with white and light blue colors, indicating no or very small displacement (<15mm).

5.3 Comparison of Monitoring Methods

No simultaneous measurement campaign was executed at the Hornbergl, hence older measurement data only enabled a comparison of movement tendencies. In particular convergence measurements, using high precision tape measure, delivered displacement rates along the south-east striking ridge and the actual Hornbergl, whereupon measured displacement mainly occurred in direction to the Herrenbach (Kirschner, 2006). Movement at the south-east striking ridge showed opening and closing tendencies with rates of 5-10 cm/a. Highest movement rates were detected at the small debris talus close to the '*Höfener Kreuz*' with rates up to 30cm/a (Moser et al., 2009).

The final mask applied within the GBInSAR investigation focused onto the actual Hornbergl and the steep cliffs along the south-east striking ridge towards the Murenbach. As no former measurement data was available covering the '*Höfener Kreuz*', the only comparison could be executed with the prior radar measurements performed by (Schaes, 2012). Due to their short time span (<48h) reliability may be not sufficient to provide a reasonable correlation with acquired data. Consistent displacement data was obtained for the toe area of the actual Hornbergl (Figure 43), whereby Schaes (2012) referred occurred movement to the slight vegetation cover. No exact explanation for detected movement could be proposed for this area.

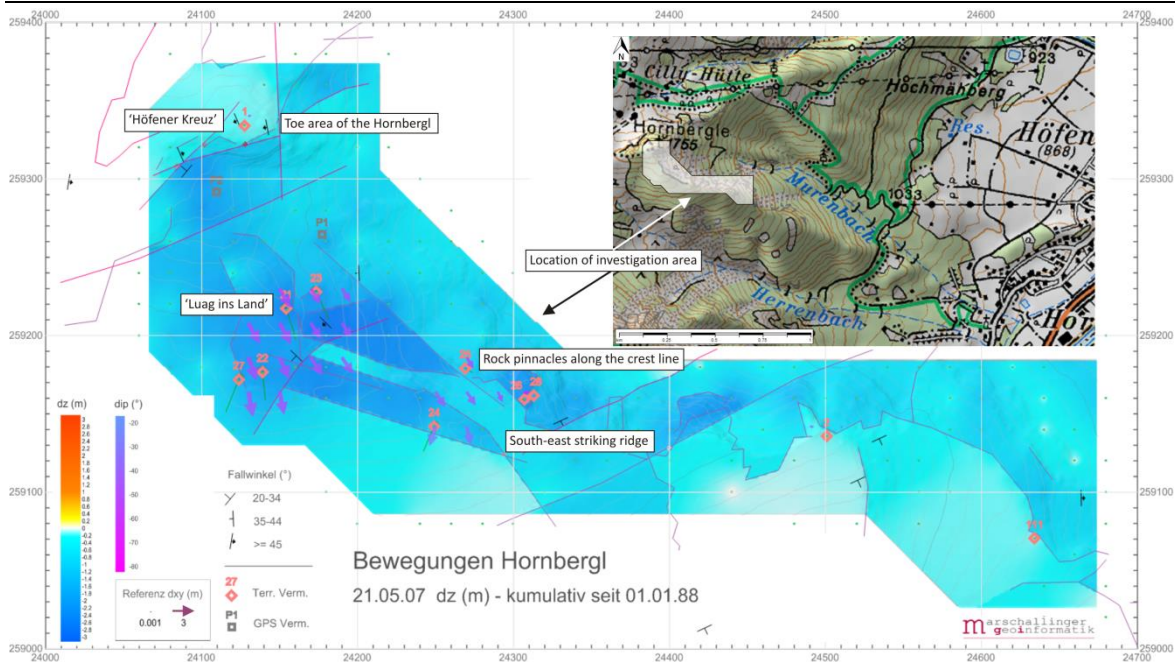


Figure 43, Long term measurement data for the entire study area (e.g. convergence and geodetic measurements); Cumulative displacement between 01.01.1988 – 21.05.2007; Arrows indicate direction and dip (purple colors) of movement; Colors indicate interpolated vertical displacement between +3m (red) and -3m (blue), modified after (Marschallinger et al., 2010)

Concerning the almost vertical cliffs along the Murenbach Moser et al. (2009) did not propose an overall movement trend towards the Murenbach (NNE), than rather in the opposite direction towards the Herrenbach (SSW-SE), even if measurement points were located beyond the crest-line (Figure 43). Convergence measurements indicated closing tendencies of large cracks, due to sliding of blocks towards the Herrenbach. Moreover, a significant increase of movement with the beginning of snowmelt could be proved over the years (approx. 2.3cm/month) (Moser et al., 2009). On the contrary very slow movement rates were detected during winter months (approx. 0.1cm/month). In general averaged 0.4 cm/month were detected within convergence measurements in this area (Moser et al., 2009). As the GBInSAR investigation of the Hornbergl lasted from late September to early December, the very low displacement values detected correlate well with long term measurements. Strong sagging tendencies of exposed rock pinnacles along the crest-line were detected by geodetic observations, showing a highly varying behavior (Moser et al., 2009). Radar observations could not prove these observations, possibly due to low movement rates in winter, or to very unfavorable directions of displacement relating to the LoS measurements of the radar. For instance vertical sagging movement would result in very low displacement rates within the radar map.

However, distinctive small-scale events were detected within the rock walls, which displayed a similar behavior to the suggested movement of the rock pinnacles on top.

5.4 Interpretation

Several areas with repeated displacement were detected during the investigation of the Hornbergl. A rough division defines areas with displacement at the talus of the steep rock walls and the Hornbergl, a moving part at the toe of the Hornbergl and a small-scale event within the steep rock walls (Figure 44). Displacement within the talus was measured during the entire investigation and generally indicated a very continuous accumulation of debris, displaying a strong correlation to rainfalls. However, detected displacement in this talus areas rather represents shallow erosional processes, than hazardous movement due to a deep seated sliding mechanism. Former debris flows originated of these talus, as these areas respond very sensitive to precipitation (Moser et al., 2009).

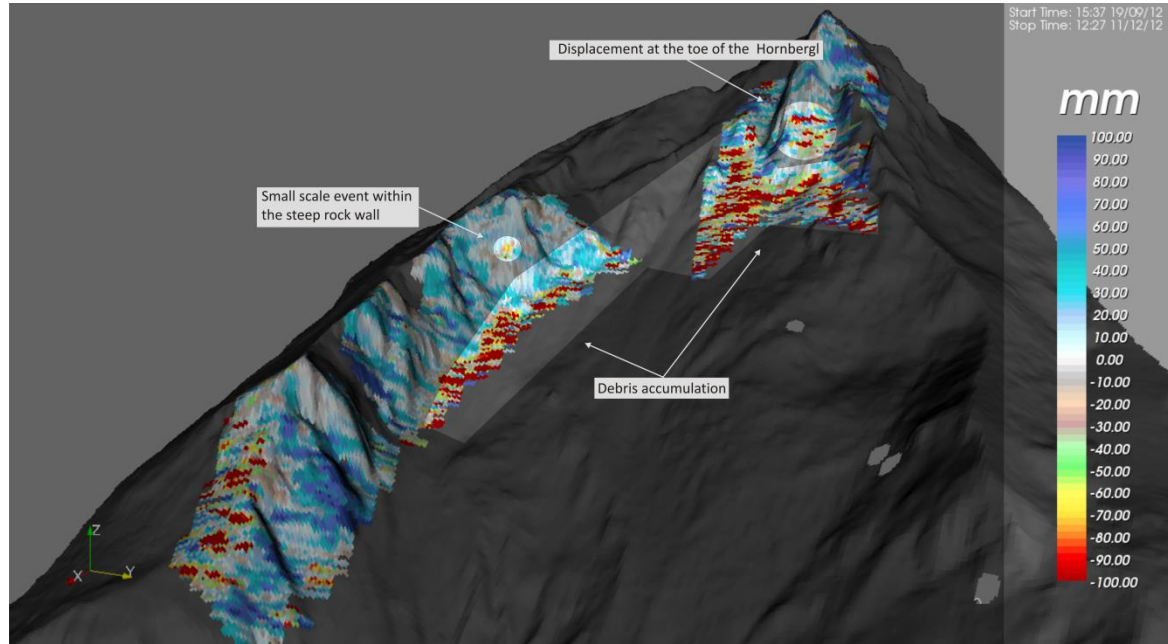


Figure 44, Areas with repeatedly detected displacement. Three distinctive zones may be classified: talus showing the accumulation of debris, a displacing area at the toe of the Hornbergl and a small-scale event within the steep rock walls. Displacement pixels in the lower left corner refer to a highly vegetated area and therefore lack a necessary reliability of acquired data.

A focus of this investigation was set on the steep and potentially hazardous sectors along the steep confining rock walls of the south-east striking ridge. During the entire monitoring period no large-scale movement occurred within this sector. A large-scale collapse of the pinnacles in Figure 45 appears very unlikely due to their constantly stable behavior throughout the entire investigation. Other measurement campaigns also detected very low displacement rates during the winter months, with a significant acceleration of movement in spring (Glabsch et al., 2009). Hence acquired radar datasets, ranging from September to December, are not ideally suitable for ruling out possible large-scale rock falls along these steep walls. On the contrary several small-scale events showed distinctive movement patterns, indicating a clear dependency to rainfalls. Very few or single moving measurement pixel do not pose a major problem, as they may refer to a discrete small block (<1m), which is not hazardous in any way within this area. Single moving pixels may even originate of vegetation and therefore resemble noise.

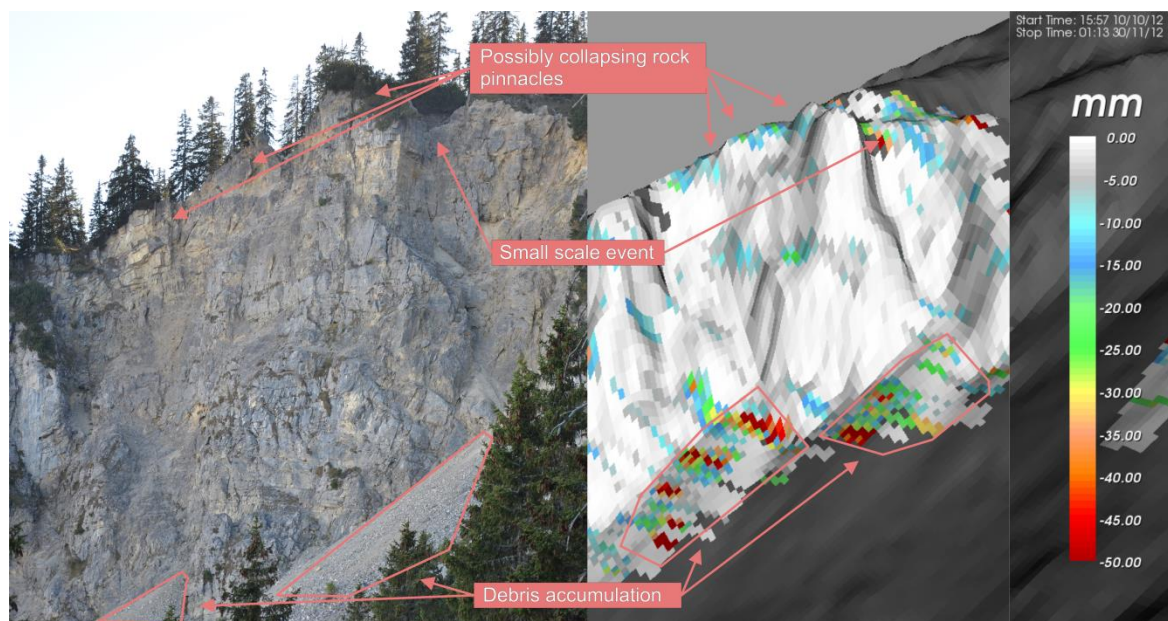


Figure 45, Comparison of detected displacement and a photograph of the steep rock wall along the south east striking ridge. Possibly collapsing rock pinnacles, exemplary small-scale event and talus (debris accumulation) are marked with arrows (Measurement period 10.10.-30.11. 2012)

Interpretation of measured displacement at the toe of the Hornbergl is complicated, as rock quality is good and without debris cover. Displacements of 10 to 40mm were detected during the entire investigation, whether they originate of shallow erosional processes or of a larger scale mechanism is very difficult to state. According to other investigations performed at this site, larger rock falls repeatedly occurred at the high-lying and steep spot, which can be seen in the yellowish colors right beneath the peak in

Figure 46 (Ploner and Sönser, 2005). As the complete Hornbergl is affected by unstable slope behavior a deep-seated failure process on adjacent fault planes may be imaginable, but rather unlikely (Moser et al., 2009, Ploner and Sönser, 2005). Schares (2012) also detected several moving pixels in this area, which were correlated to the slight grass cover in this area.

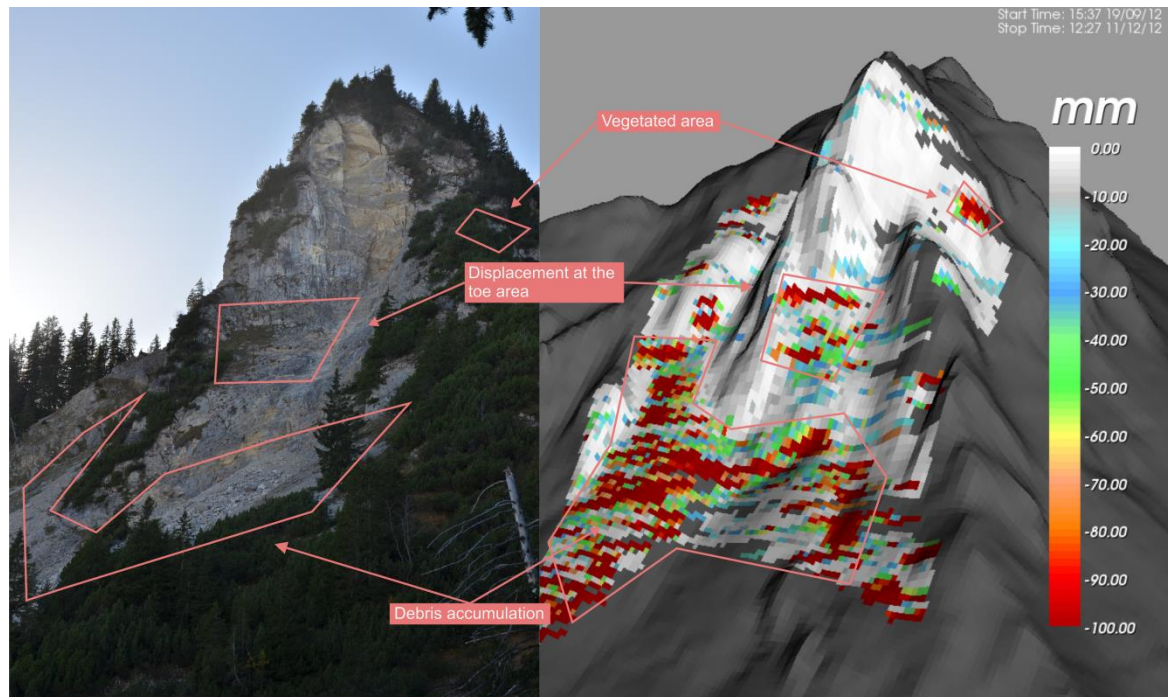


Figure 46, Left photograph shows the Hornbergl in October 2012; right image displays the accumulated displacement of the entire investigation period. Displacement areas are highlighted and linked between the two images to gain a better understanding of the acquired data.

A detailed correlation of measured displacement and a photograph is given in Figure 46 for the Hornbergl and its adjacent debris talus. Highest displacement values were detected within the talus beneath the Hornbergl. Displacement is triggered very easily in loose debris and refers to continuous erosion patterns than to distinctive events. The area to the right edge of the Hornbergl displays a high amount of pseudo-displacement, as this spot is densely vegetated with mountain pines. Although measurement pixels on this spot passed the filtering thresholds, reliability for the acquired data is not sufficient. Calculated displacement values cannot be assured for this particular area.

6. Ingelsberg GBInSAR Measurement Campaign

6.1 Instrument Setup

Finding the ideal radar position for the investigation of the Ingelsberg was a rather simple process, as previous monitoring results indicated opening tendencies of cracks in direction to the valley bottom (Wilhelmstötter, 2013). Therefore the LoS of IBIS-FL would almost perfectly match the expected real displacement (Figure 47). Additionally undisturbed view, perfect accessibility and continuous power supply was given with the position close to the road. A small baseplate was built with three smaller concrete blocks on top, as an adequate foundation for the monitoring campaign. The GBInSAR equipment was then mounted following the same procedure as for the Hornberg!

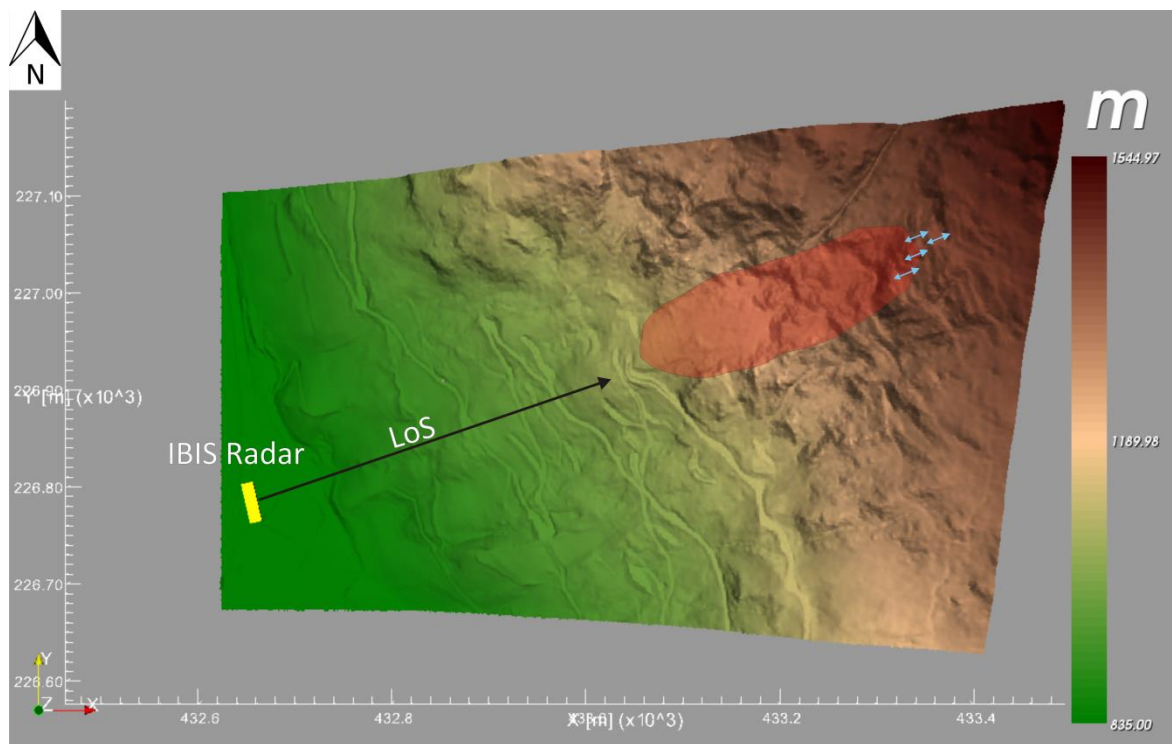


Figure 47, Position of the IBIS Radar in Bad Hofgastein for investigating the Ingelsberg. Red shaded area refers to illuminated area, LoS resembles the direction of measurement and arrows (blue) indicate opening tendencies of previously monitored cracks.

For the investigation of the Ingelsberg ten trihedral corner reflectors were mounted within the entire site (Figure 48). With an edge length of 30cm and a weight of roughly 5kg, support was required during the mounting process. Their installation was enabled due to the help of the WLV (Wildbach und Lawinenverbauung), ÖBRD (Österreichischer Bergrettungsdienst) and the support via helicopter. These reflectors provide a strong and

stable phase signal even within the vegetated non-moving area and are therefore ideal for distinguishing between moving and stable parts of the Ingelsberg.



Figure 48, Installation of a corner reflector close to a fixed reflecting prism; Mounted corner reflector No. 8

A fixed weather station was installed on the roof of the radar shelter in Bad Hofgastein. Using online data transfer via www.weatherlink.com the acquired data was sent to Graz for further processing and interpretation. The installed weather station measures several climatic parameters including atmospheric pressure, rain, temperature and wind direction/speed. The main interest was on temperature and precipitation values, as they have a major influence on occurring displacement (Moser et al., 2009, Wilhelmstötter, 2013).

The equipment setup for the measurement campaign of the Ingelsberg in Bad Hofgastein was performed on March 26th and 27th 2013. The maximum range was at approximately 1.2km. Neighboring trees and bushes at the boundary of the investigated area were excluded using selection masks or high coherence filtering thresholds. Monitoring is intended to continue until the end of 2013 to acquire a data set of several months.

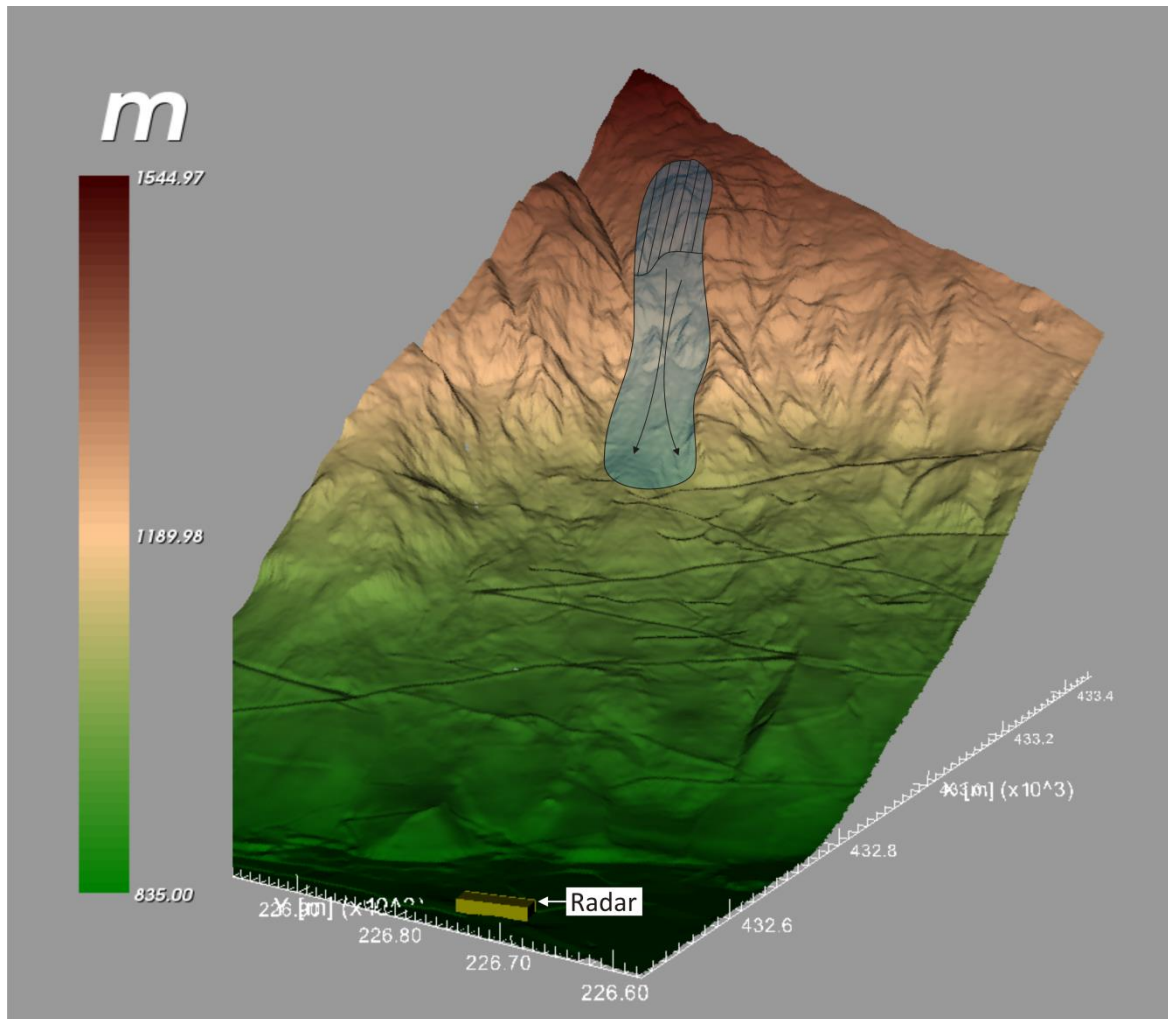


Figure 49, Investigated area projected on the used aerial laser scan DTM (View looking E). Yellow box indicates position of the radar, shaded area roughly indicates the area of slope instability.

The main goal of the investigation is to gain a better understanding of the slope behavior, more precisely on detecting and defining areas of instability. Figure 49 is an overview of the location and extent of the investigated area within the slope.

Due to software and hardware upgrades on May 2nd 2013, processing had to be restarted and separated into two phases. Figure 50 provides an overview of the survey site and the masked area. Different masks were used during the evaluation and processing, however, best results were achieved with masks that excluded vegetation very precisely.

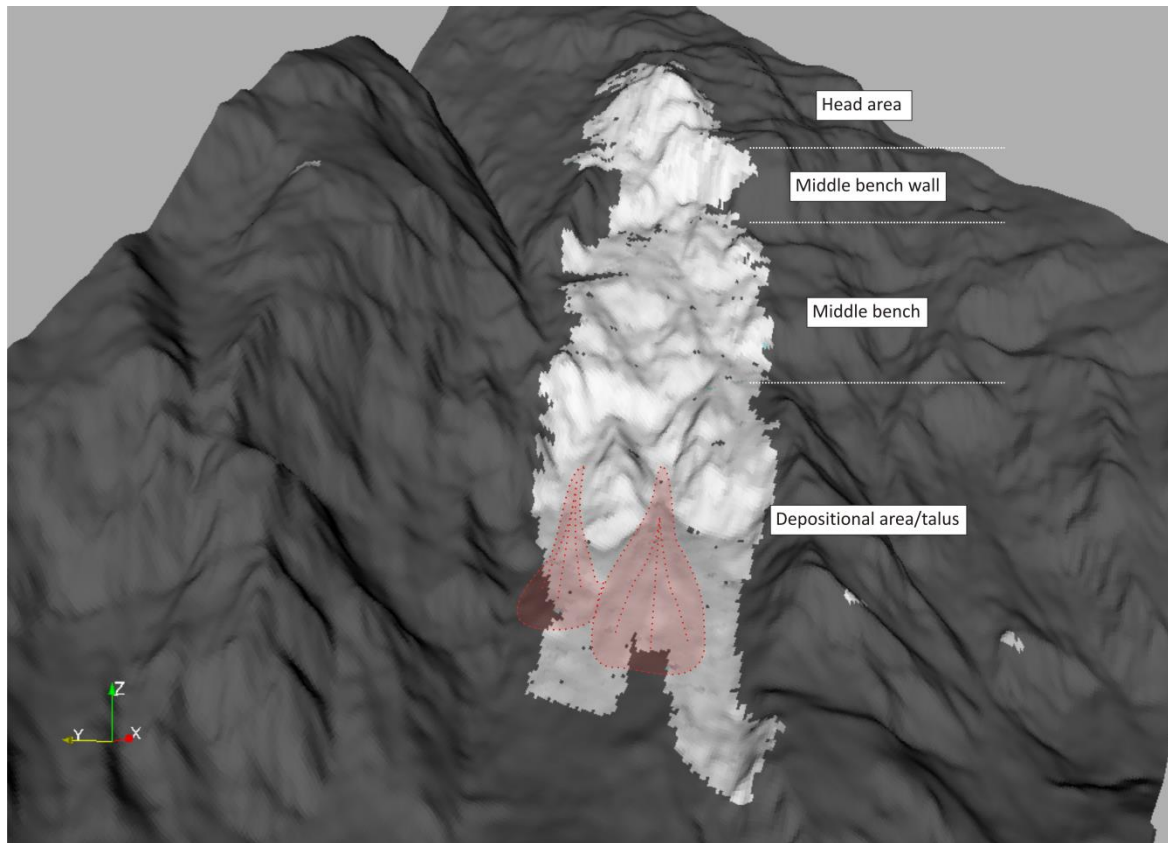


Figure 50, Overview of the masked area at the Ingelsberg without any processed displacement. Red shaded areas indicate major talus.

6.2 Measurement Results

6.2.1 Phase 1 (27.03. – 01.05.2013)

Soon after the implementation of first measurements displacement patterns became apparent, often correlating with rainfall events. Figure 51 displays 13 randomly selected pixels within the depositional area and their corresponding displacement time series in correlation with precipitation. At the beginning of the measurement campaign all pixels retained a stable position, however, with the onset of rain on March 30th and 31st 2013, displacements started to occur. Within four days some measurement pixels showed displacements of up to -80mm in the LoS direction. The negative displacement value indicates a movement towards the radar and therefore a movement towards the valley. One week after the rainfall event pixels stabilized again and remained at their position. Throughout the entire measurement campaign displacement occurred repeatedly within this and other talus deposits.

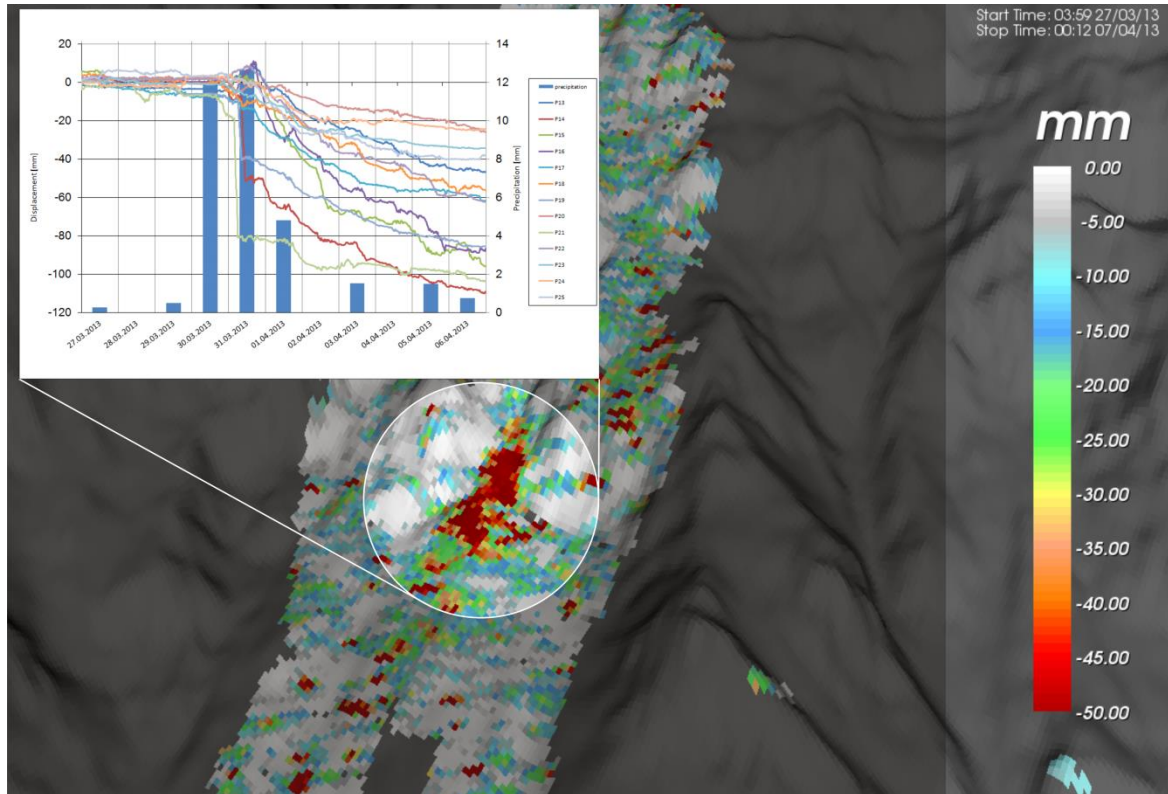


Figure 51, Position of the onset of the main talus in the depositional area. P13-P24 are randomly scattered along the highly moving pixels. Displacement [mm] of selected points plotted against measured precipitation [mm].

Contrary to the repeated displacement within the talus, a distinct rock fall event took place on April 29th 2013. The source of this rock fall was located within the head area of the Ingelsberg. Movement started on April 18th and continued at an average rate of 0.12mm/hour until the 28th of April. During the 28th of April displacement accelerated

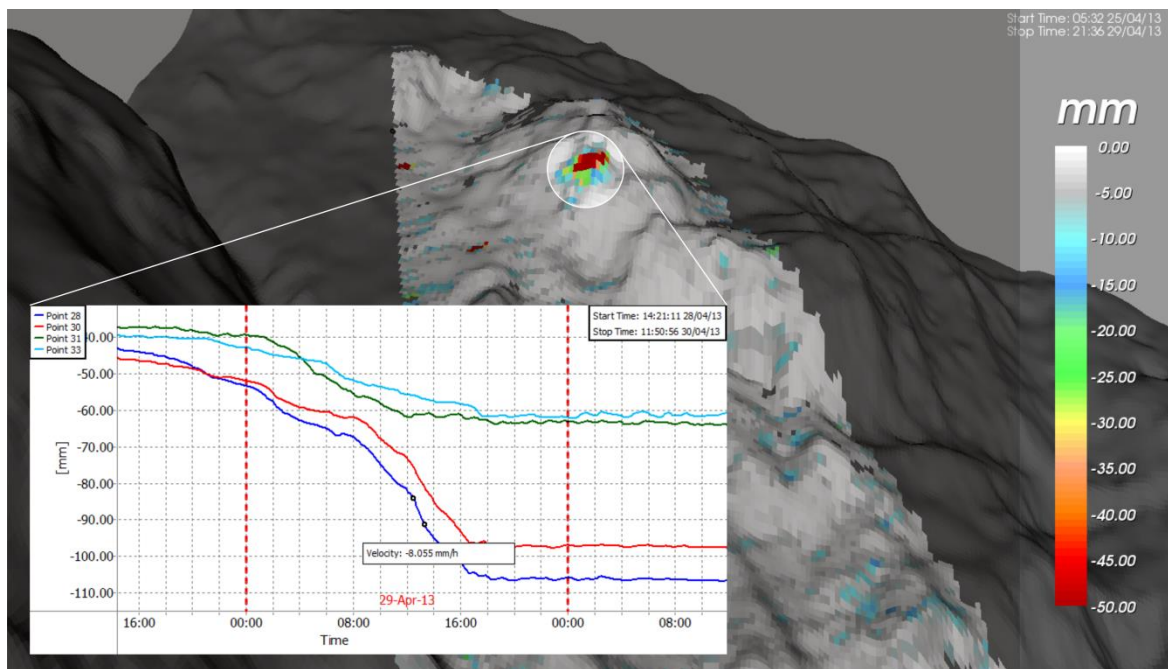


Figure 52, Time series of measurement pixels within the head area shortly before the stabilization. Final movement rates between two selected points reached up to 8.055mm/h. The negative value indicates a movement towards the radar. Movement stopped at around 17:00 on April 29th 2013.

significantly, continuing until the 29th of April leading to a distinctive stabilization after 17:00 on the same day. In the final phase of displacement movement rates of 8mm/hour were detected (see Figure 52).

In Figure 53 areas with highly moving pixels are marked and aligned with the plotted time series. Measurement pixels within the investigated area were selected across the detected displacement to gain an overview of the occurred movement. All time series range from April 11th until May 1st and therefore cover the beginning of the detachment process until the rock fall event of April 29th 2013. Displacement time series of the detachment area indicate a steady movement over nine to ten days with a rapid acceleration during the last two days (Figure 53). Before the rock fall an accumulated displacement of up to 70mm was measured, until measurement pixels stabilized in the head area. Time series of displacing pixels at the middle bench and the depositional area show continuous displacement (Figure 53). However, two distinctive events of accelerated displacement are visible, whereupon the first on April 19th clearly correlates with rainfalls (16mm precipitation on 19.04.). The second event on April 29th displays a shortly delayed correlation with the occurred rock fall in the head area.

6.2.2 Phase 2 (03.05.2013 - Present)

Due to the software upgrade to the most recent version of IBIS-FL a separation into two measurement phases at the Ingelsberg had to be executed. Mainly the missing compatibility between the two different data types of performed measurements made this step necessary. The readjustment was performed on May 2nd 2013 and measurements were restarted on May 3rd 2013. The basic advantage of the new operating system is the drastic reduction of measurement time (7 to 2.5 min) and the accompanying reduced atmospheric influence, due to the shorter exposure to changing weather conditions. Additionally default settings of filtering parameters increased the thresholds for measurement pixels and therefore slightly lowered the number of selected pixels.

Former rock fall events and already executed monitoring campaigns confirm the head area of the Ingelsberg as a potentially hazardous spot within the investigation site (Wilhelmstötter, 2013). The rock fall event on April 29th 2013 also proved this statement and therefore special focus was put on monitoring any displacement within this area. The middle bench wall at the lower part of the head area was monitored and according time series were analyzed (Figure 54). Additionally, the uppermost head area was investigated (Figure 54). Wilhelmstötter (2013) also suggested a further investigation and extended protection measures for the confining ridge to the south of the currently active area. Hence a selection of coherent pixel and their according time series were analyzed, though vegetation complicated a comprehensive analysis.

Figure 54 and Figure 56 display two different radar maps with scales ranging from +50mm to 0mm and from 0mm to -50mm, indicating movement in the LoS away from the radar and towards the radar, respectively. As collapsing material has to leave a gap at its origin rock falls should also be detectable on the radar map showing positive values. No displacement within the scales ranging from +50mm to 0mm with simultaneous displacement within the scales ranging from 0mm to -50mm either reflects no collapse of the moving mass or a different source area.

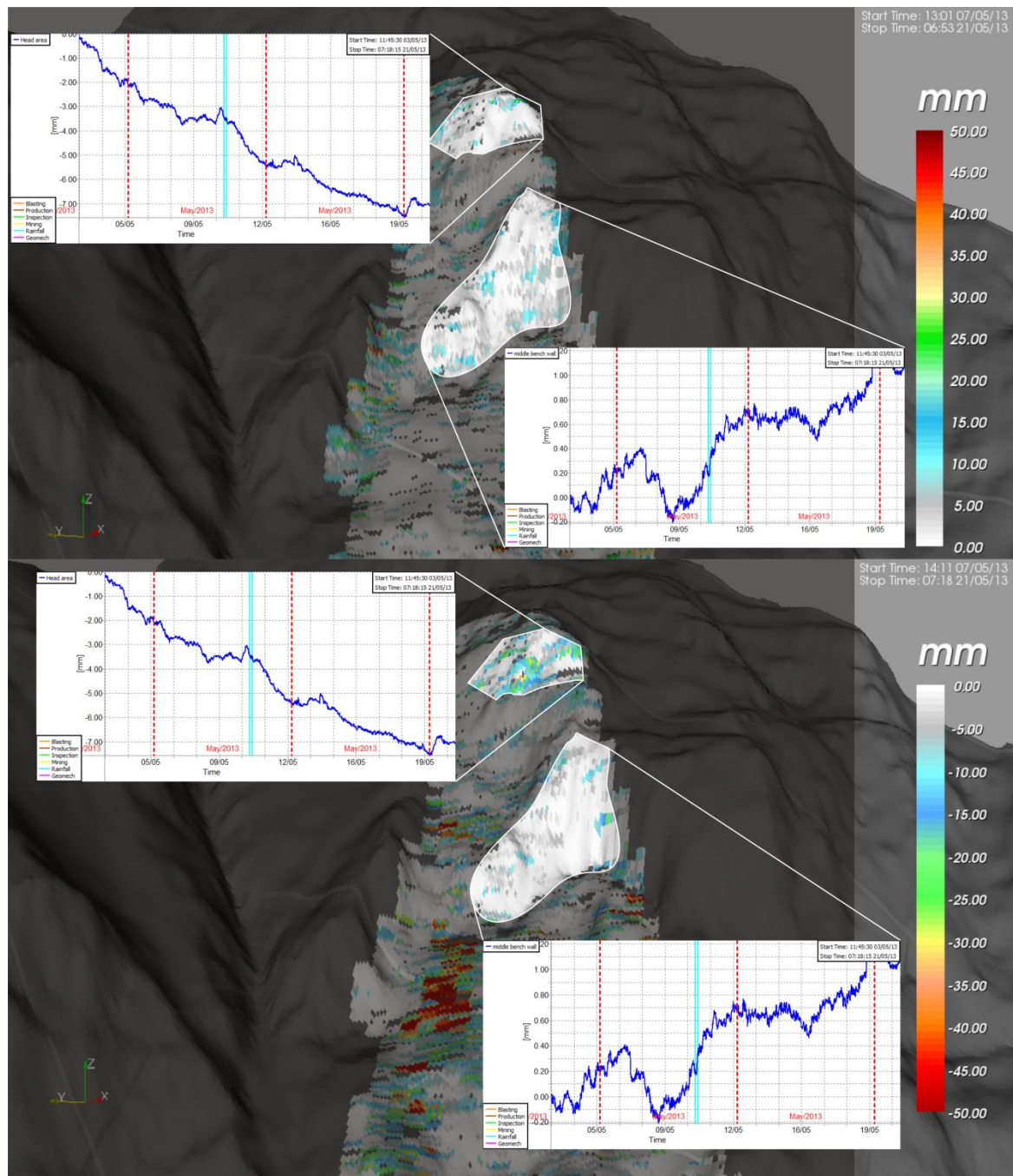


Figure 54, Averaged time series of investigation areas at the *head area* and at the *middle bench wall* above the middle bench. Top graph displays movement away from the radar (+50 – 0mm), bottom graph displays movement towards the radar (0 – 50mm). The turquoise bar represents a major rainfall with 50mm of accumulated rain within two days (10./11.05.2013)

In Figure 54 focusing areas are highlighted and their averaged time series are plotted. The upper area will be referred as '*head area*' and the lower one as '*middle bench wall*'. The second one was selected on an almost vertical and partly jointed wall, which separates the uppermost head area from the middle bench beneath.

Time series of the *middle bench wall* indicated a very continuous, almost oscillating movement ranging within 2mm. On the contrary a distinctive trend of displacement was

observable within the time series of the *head area*. As the time series in Figure 54 displays an averaged value of all measurement pixels, the selected area was investigated in terms of an overall movement tendency and on single highly displacing pixels. Detailed investigation indicated very few highly moving pixels (up to 60mm) which caused an overall moving tendency of the *head area*, whereas the majority of measurement pixels showed no or small displacement (Figure 55).

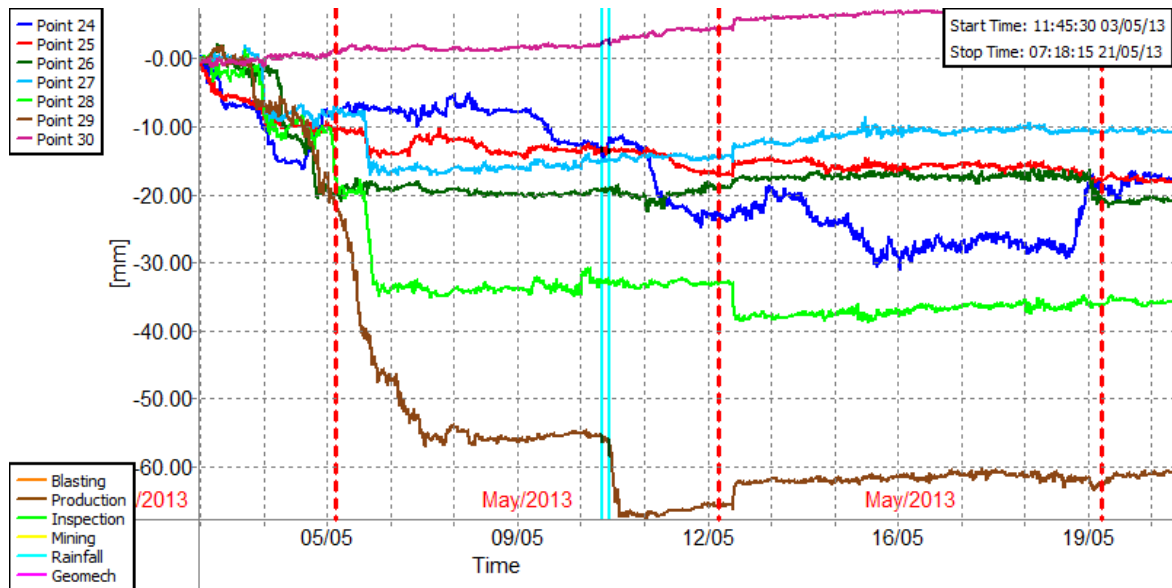


Figure 55, Time series of displacing and stable pixels within the *head area*. The turquoise bar represents a major rainfall with 50mm of accumulated precipitation within two days (10./11.05.2013)

A further focus was on the confining ridge in the south of the currently active area. Observed from the radar's point of view this ridge is located right to the illuminated area. The chosen mask does not extend too far into vegetated terrain, as the SNR and coherence values drop significantly below an acceptable value. No large-scale displacement was detected at the ridge or its adjacent area. However, several smaller areas, including a few pixels, showed distinctive displacement in both directions, away and towards the radar (up to 50mm). Figure 56 shows the focused area and its according time series, which are all situated within highly moving areas and red colored pixels, respectively. Time series of the upper radar map indicate a movement away from the radar with a mean displacement of 30mm, whereas the lower radar map shows movements towards the radar with an averaged displacement of roughly 20mm during the time span of May 3rd until May 21st 2013.

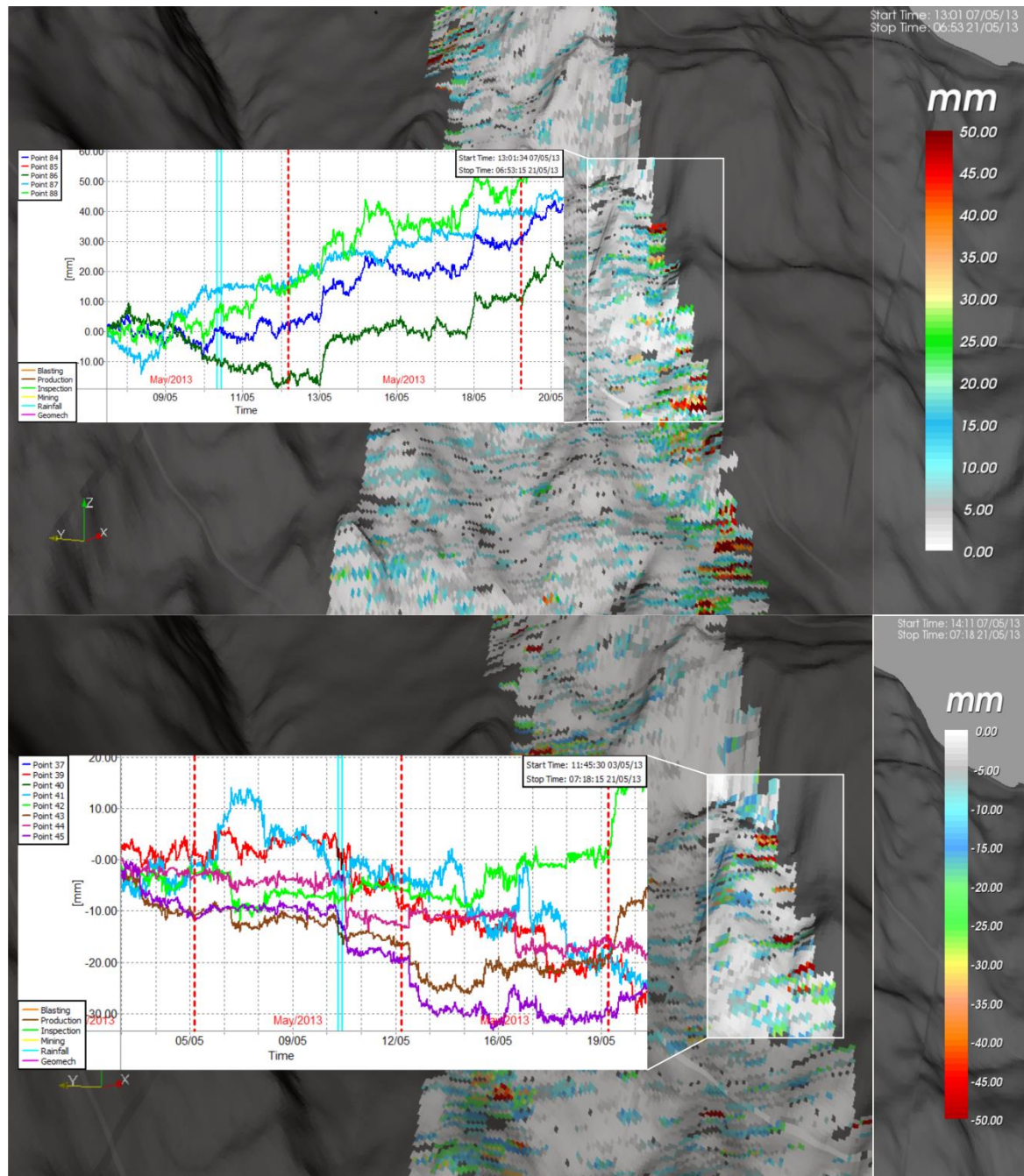


Figure 56, Selected time series of various measurement pixels along the right confining ridge of the masked area. The turquoise bar represents a major rainfall on May 10th and 11th with 50mm of accumulated precipitation. Top graph displays movement away from the radar (+50 – 0mm), bottom graph displays movement towards the radar (0 – (-)50mm).

Precipitation during the last days of May and the first days of June (30.05.-02.06.2013) exceeded all previously measured values in 2013 regarding the amount and duration of rainfall (approx. 150mm within 4 days, Figure 57). Causing a catastrophic flooding in the entire federal state of Salzburg these rainfall events also strongly affected the Ingelsberg, resulting in extreme displacement within most of the investigation site. Due to the enormous water saturation, several minor debris avalanches and even small streamlets developed along the already established erosional rills.

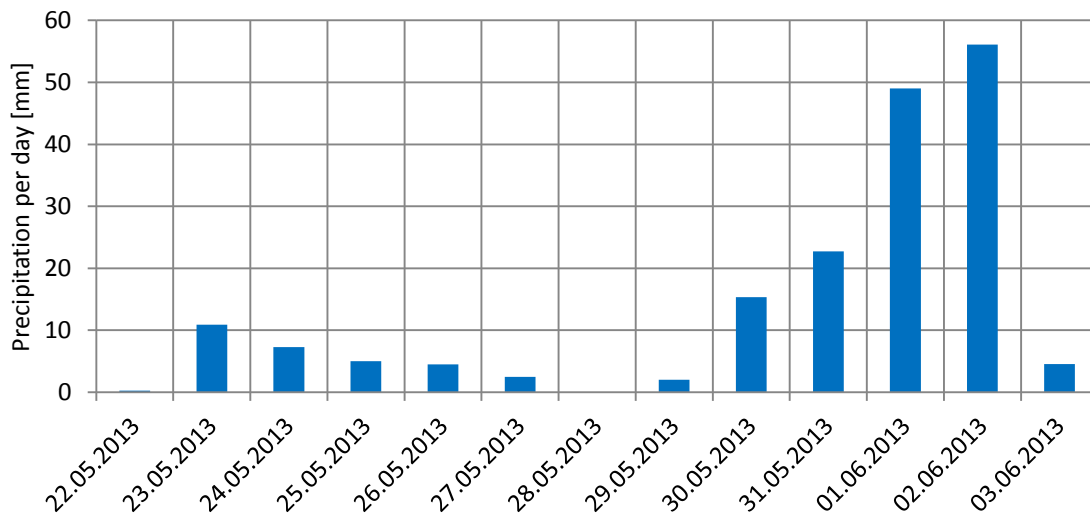


Figure 57, Extreme rainfall events during 22.05. – 03.06.2013

Graph (b) and (c) in Figure 58 display randomly selected points within the lower right talus and the accumulated debris on the middle bench. The entire middle bench, as well as the talus in the depositional area are affected by movements $>50\text{mm}$ within the investigation interval of 22.05. – 04.06. 2013. Both the extent and the magnitude of occurred displacement exceed previously detected movement. Single pixels at the middle bench indicated displacements up to 100mm within 3 days (see graph (b) in Figure 58). Maximum values reached up to 400mm within 3 days at the talus in the depositional area (see Graph (c) in Figure 58). On the contrary no distinctive acceleration of displacement was detected at the head area. Graph (a) displays a slight correlation to the rainfalls, however, averaged 4mm of displacement for this investigation area do not represent alarming displacement values. Still camera images show several small detaching blocks ($<1\text{m}$), some descending until the first rock dam. Images of the dam camera proved the increased accumulation of blocks and debris at this first protective barrier. Graph (d) displays time series of selected pixels within a newly developing zone of movement in the head area.

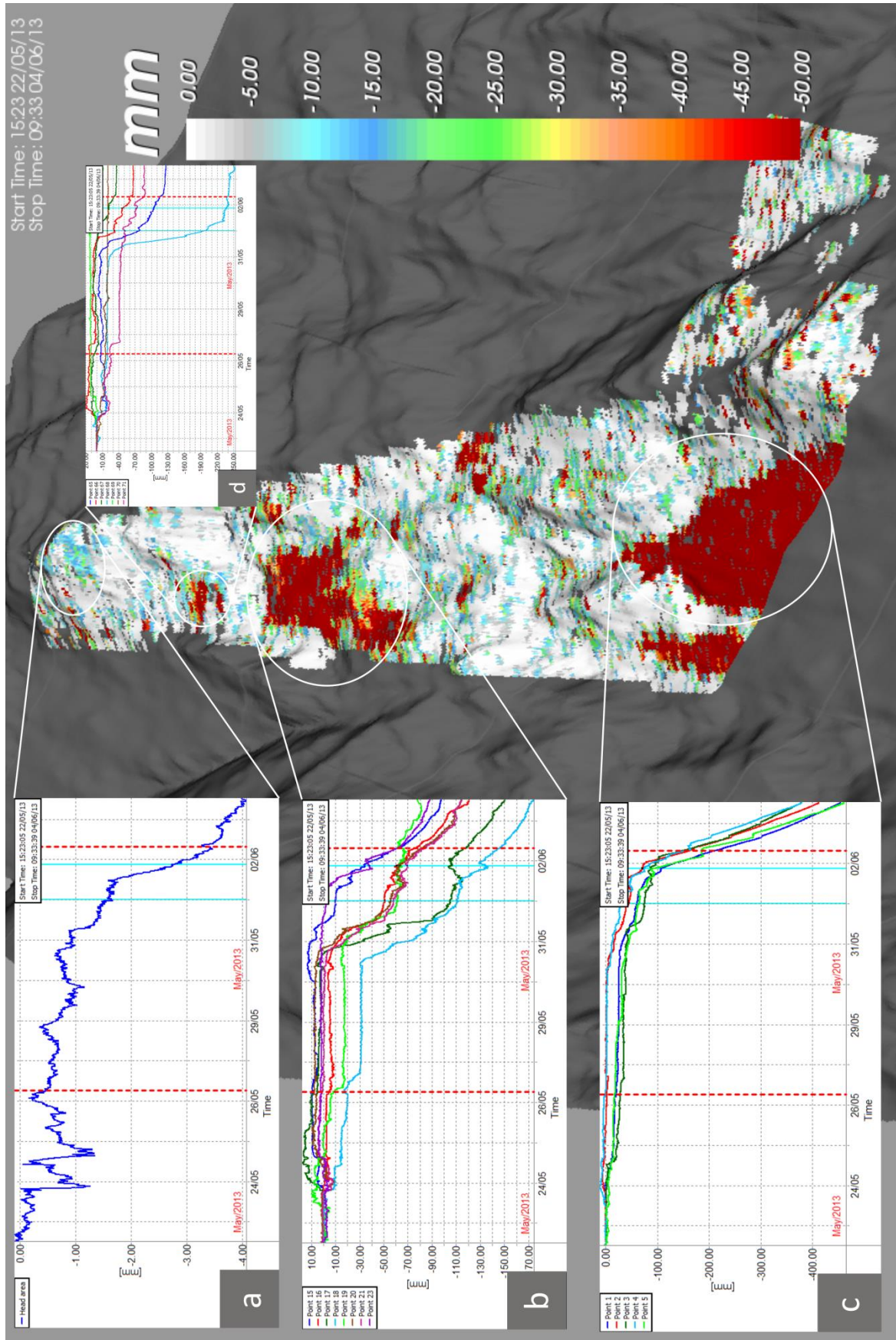


Figure 58, Displacement map during the time span of 22.05.-04.06.2013 displaying a significant acceleration of movement with the onset of extreme rainfall during 31.05-02.06.; Graph (a) shows times series of the head area with only minor impact of rainfall; Graph (b) and (c) are located within depositional areas and strongly respond to the rainfall. Graph (d) indicates a newly developing area of displacement at the lower part of the head area.

A summarizing radar map of Phase 2 including the most recent data is displayed in Figure 59 (03.05.–14.10.2013). Used scale bars range from +100mm to -100mm to include possible outbreak or source areas, indicated in blue colors. Movement away in the LoS of the radar (positive values) was mainly detected at the left and right boundary of the masked area, as well as between the two major talus in the depositional area. Significant displacement towards the radar (negative values) was consistently measured within depositional areas (e.g. lower talus or middle bench). A strong correlation of rainfalls and occurred movement in the depositional areas is shown in the time series of Figure 59, which displays a mean value of measurement pixels of the lower talus. White or greyish colors display less or no movement (+10mm to -10mm) and are located at the middle bench wall. The head area indicates selective pixels with significant displacement, however, no overall trend of movement is visible.

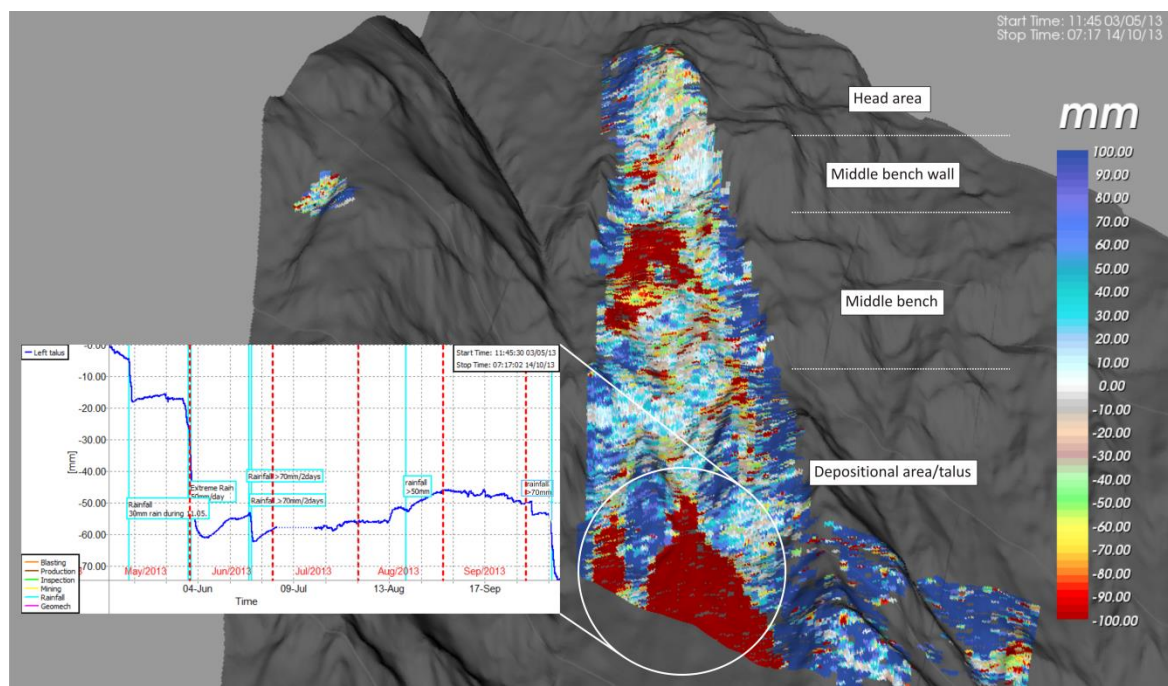


Figure 59, Displacement map of phase 2 including the most recent data (03.05.–14.10.2013). Used scale bar ranges from +100mm to -100mm. Plotted time series shows strong correlation of rainfalls and displacement in the lower talus. Turquoise bars represent rainfall events with more than 30mm/day.

6.2.3 Comparison of Different Masks

Comparison was carried out by selecting a number of pixels within the survey area and plotting their associated time series. A careful selection of highly coherent pixels guaranteed stability to high filtering thresholds. Pixels lacking a strong signal or a high coherence would be eliminated and comparison would be impossible.

The occurrence and tendency of measured displacement within different time series, according to different masks were consistent. Differences in accumulated displacement were detected, whereby the causing algorithms cannot be accessed within IBIS Guardian. Exemplary time series are plotted in Figure 60 showing calculated displacements of five chosen points within a debris talus. Points 1-5 were selected and imported in two projects using different masks and have the exact same coordinates. The mask *ingels_exact* is very accurately drawn around vegetated areas to exclude their influence. According time series are plotted with blue colors. On the contrary the mask *ingels_26_03* defines the processed area less accurate and includes several less coherent border areas. According time series are shown in red colors and accumulate less displacement than time series of mask *ingels_exact*. The differences between point-pairs reach up to 100mm (e.g. Point 1) though they average in a difference of 10-20mm. Theoretically, calculated displacements for the exact same points should be consistent,

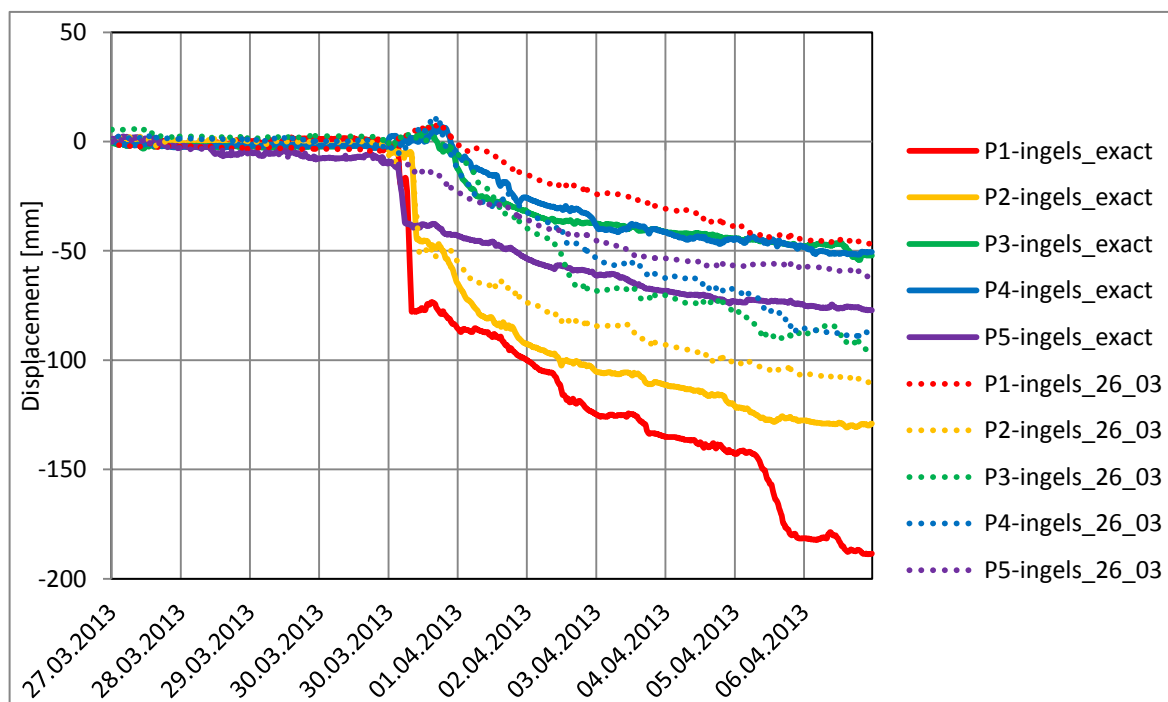


Figure 60, Comparison of exemplary time series using different masks (*ingels_exact* & *ingels_26_03*)

in practice the complex algorithms used in IBIS Guardian during processing depend on too many different variables. Slight changes in the overall pixel number and applied thresholds may influence the dimension of calculated displacement, but do not interfere with the onset, general direction or the stopping time of detected movement.

6.2.4 IBIS Data Viewer

The former processing and evaluation software IBIS Data Viewer was replaced by IBIS Guardian due to its visualization possibilities and the convenient user interface. Therefore IBIS-DV was only used for calculating the atmospheric influence regarding the measured displacement. In order to distinguish between real displacement and pseudo-displacement ground control points (GCP) had to be defined and assumed as completely stable. Figure 61 displays the location of all ten Corner Reflectors distributed along the investigated area, which were mounted to act as Ground Control Points. GCP 1, 3, 4 and 5 are supposed to be within the moving area, whereas the rest of the reflectors are situated at locations with no previously detected movement.



Figure 61, Position of all 10 Corner Reflectors within the investigation area.

6.2.4.1 Ground Control Points

The installation of trihedral Corner Reflectors within the investigation area has two big advantages. As they provide a very stable and strong signal they can be used as ground control points within the IBIS Data Viewer (IBIS-DV) to estimate the dimension of atmospheric influence. Within IBIS Guardian the exact embedding of Corner Reflectors is not specifically enabled, as IBIS Guardian applies an automatic correction of atmospheric artifacts using the permanent scatterer (PS) technique. IBIS-DV enables the input of this absolutely coherent and distinctive signals, providing stable references to support the application of the correction algorithms, as they improve the signal to noise ratio (IDS, 2013). For the differentiation between moving and stable parts within strongly vegetated areas corner reflectors deliver a referencing background for these mostly noise affected pixels.

To gain an estimate about the dimension of atmospheric influence all reflectors were considered suitable as ground control points, however, two reflectors (GCP9 and GCP10) could not be identified due to interfering signals. Eight corner reflectors were defined as ground control points within IBIS-DV. Detailed investigation showed that even though reflectors 1, 3, 4 and 5 are situated in the unstable area no displacement occurred at these particular spots. Therefore, the eight identifiable Corner Reflectors are defined as stable and every displacement calculated within the time series may be considered as pseudo-displacement, caused by changing atmospheric conditions (e.g. humidity, atmospheric pressure and temperature).

The atmospheric correction is based on the spatially homogenous distribution of atmospheric effects and its linear, distance depending effect on the phase signal (Colesanti et al., 2003, IDS, 2012). The top graph in Figure 62 displays this linear dependency as GCP 5, 6 and 7 show the highest pseudo-displacement values, whereas GCP8 shows almost no pseudo-displacement. GCP 5, 6 and 7 are situated 958m, 1075m and 1264m away in the sensor's Line of Sight. In contrast GCP 8 is located close to the farm in the foreground, with a distance of only 338m to the radar. However, the importance of accurate atmospheric correction is visible, as the accumulated LoS displacement reaches up to 30mm within 12 days of monitoring.

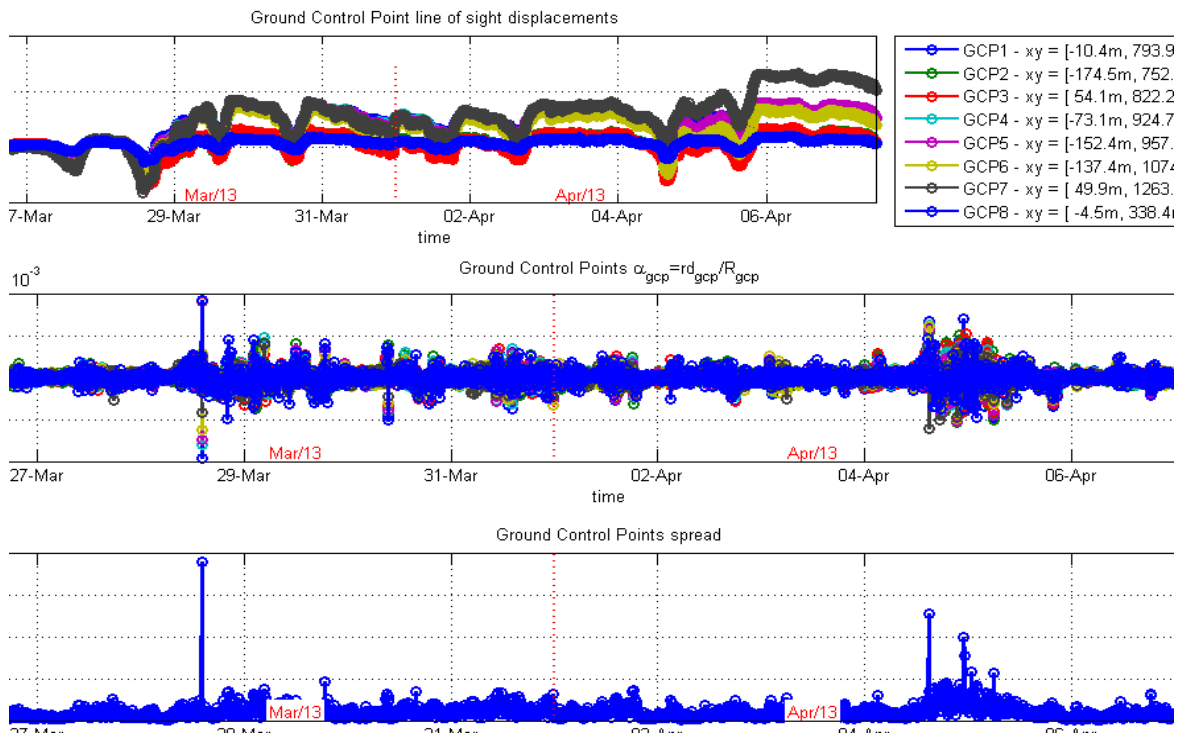


Figure 62, Calculated pseudo displacement of selected Corner Reflectors. α_{gcp} is a correction factor for each GCP. The bottom graph indicates the quality of the atmospheric correction (low values = high quality)

The central graph of Figure 62 displays the ratio between the radial differential displacement of a GCP and its distance to the radar. If the chosen reflectors are stable and the applied atmospheric corrections valid, all GCPs should have the same α factor (IDS, 2012). The bottom graph is calculated by the difference between the maximum and minimum α factor of each image. High values for this factor refer to a low quality of the selected GCP, low values indicate an adequate atmospheric correction. As both, the central and the bottom graph generally show very steady and low values, the calculated atmospheric correction eliminates pseudo-displacements in a very efficient way.

By calculating the atmospheric artifact via IBIS-DV some insight in the dimension of such correction data could be gained. Again the necessity of adequate correction data could be proved, as GBInSAR equipment suffers of high sensitivity against changing meteorological conditions. However, the elimination of atmospheric artifacts is realized automatically within IBIS Guardian via the permanent scatterer approach.

6.3 Comparison of Monitoring Methods

Two monitoring methods were applied at the Ingelsberg during the time span of radar investigation. Four fissurometer are still installed at four major tension cracks at the uppermost head area to monitor relative opening distances. Additionally total station measurements were executed to enable a comparison of the direction of occurred movement.

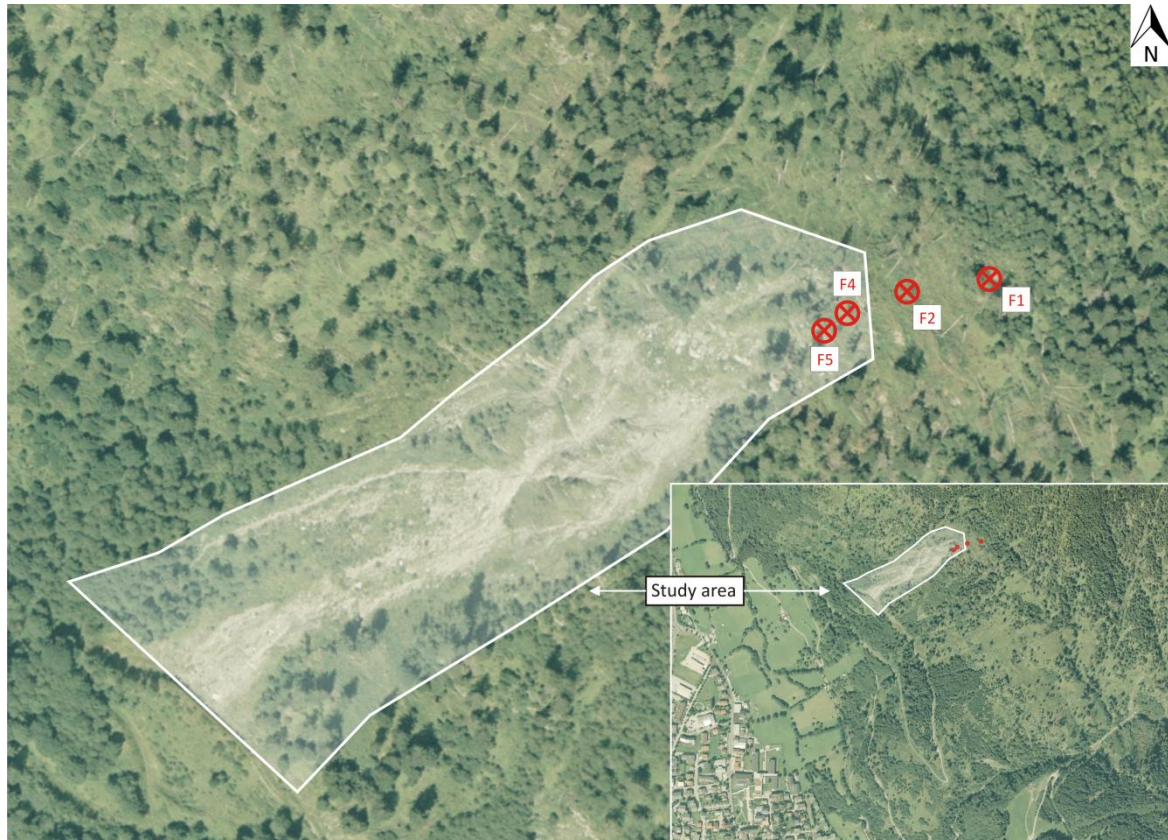


Figure 63, Location of fissurometers F1, F2, F4, and F5

Of initially five fissurometer only four are delivering data up to this date (October 2013). Fissurometer 1 is situated most easterly, Fissurometer 5 is located closest to the escarpment of the head area and therefore most westerly (Figure 63). Fissurometer 5 displays the highest relative displacement values and responds most sensitive to precipitation. In contrary fissurometer 2 and 4 remained generally stable without displaying distinctive movement. According to Wilhelmstötter (2013) fissurometer 1 indicated similar behavior as fissurometer 2 in the summer of 2012, however, since mid of April 2013 increasing values were detected, continuing until the end of June 2013. Since July 2013 all fissurometers displayed stable behavior. Figure 64 correlates

displacement at the fissurometers with measured precipitation, connecting the onset of accelerating displacement with an accumulated precipitation of 40mm during the time span of April 12th to 19th 2013. These rainfalls possibly triggered the rock fall of April 29th 2013 and induced significant displacement within the debris talus of the study site. The bottom graph of Figure 64 displays distinctive acceleration of displacement on April 18th and 19th 2013, showing an exact correlation with the measured displacement at fissurometer 1 and particularly fissurometer 5. In both graphs movement started with the onset of rainfalls on April 12th 2013.

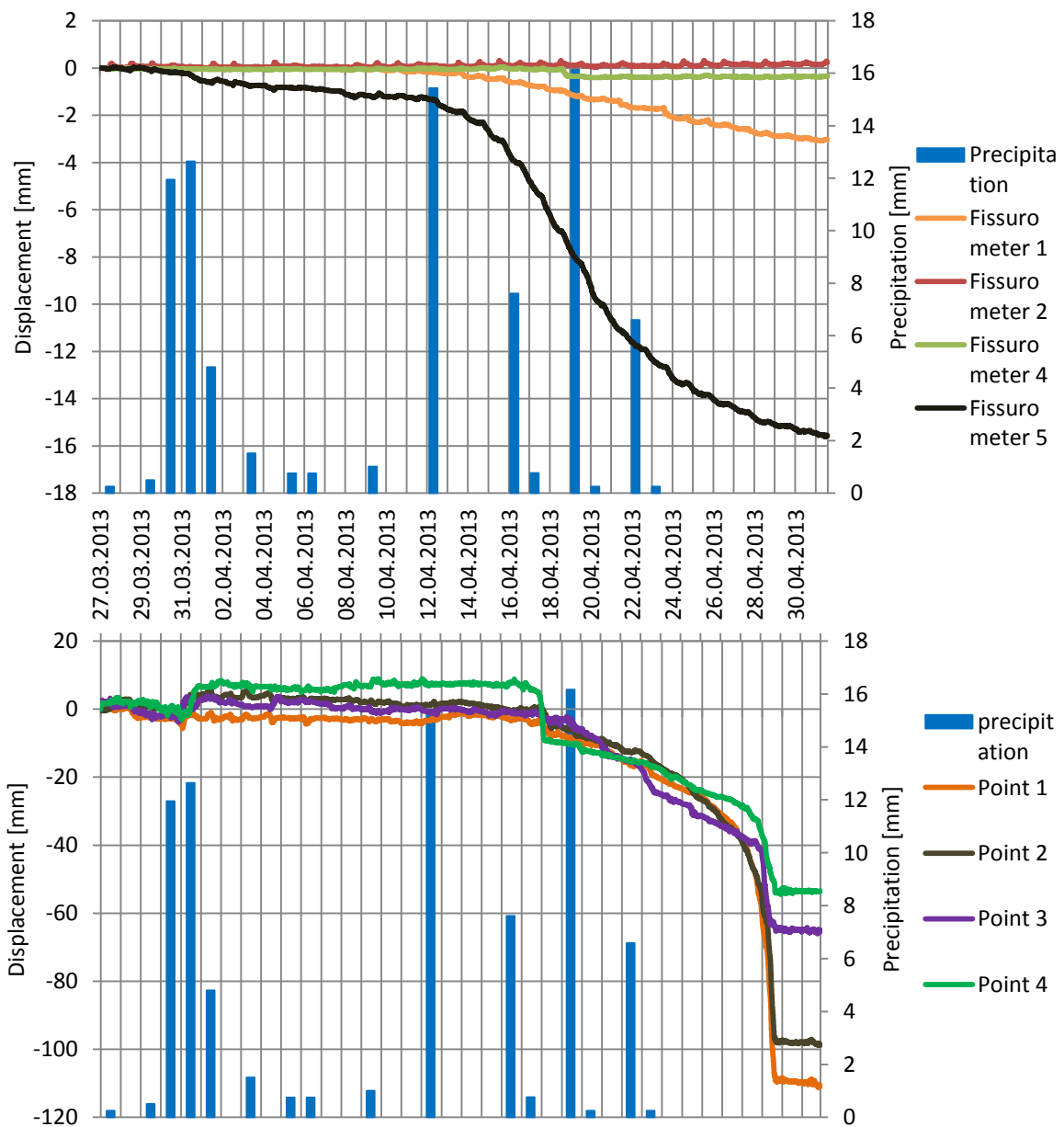


Figure 64, Top graph displays measured fissurometer displacement vs. precipitation; bottom graph indicates radar displacement vs. precipitation. Fissurometer 1 and 5 clearly correlate with detected movement at Points 1-4 in the head area.

In summary fissurometer 1 and 5 clearly indicate a correlation of measured displacement with the radar time series. By showing a similar response to rainfall events their accumulated displacement enables a comparison of movement tendencies in terms of intervals and time span, however, the dimension and direction of displacement is not completely consistent. Radar measurements (LoS) and installed fissurometers both detect similar movement trends of the head area, as their orientation is almost concordant. The dimension of displacement differs strongly, as radar measurements detect movement on the surface, fissurometers on the contrary measure opening distances of selected cracks.

The monitoring program of the Ingelsberg included the observation of fixed reflecting prisms using a total station. According to Wilhelmstötter (2013) and the Geodetic Service of Salzburg required accuracy and reliability of the measurements could not be obtained. The measurement range of 1.2km and its accompanying atmospheric effects (e.g. different warming of air layers), as well as the measurement accuracy of a total station prevented useful measurements (Wilhelmstötter, 2013). Repeatedly executed measurements displayed unsteady movements to the North and South (Figure 65) and

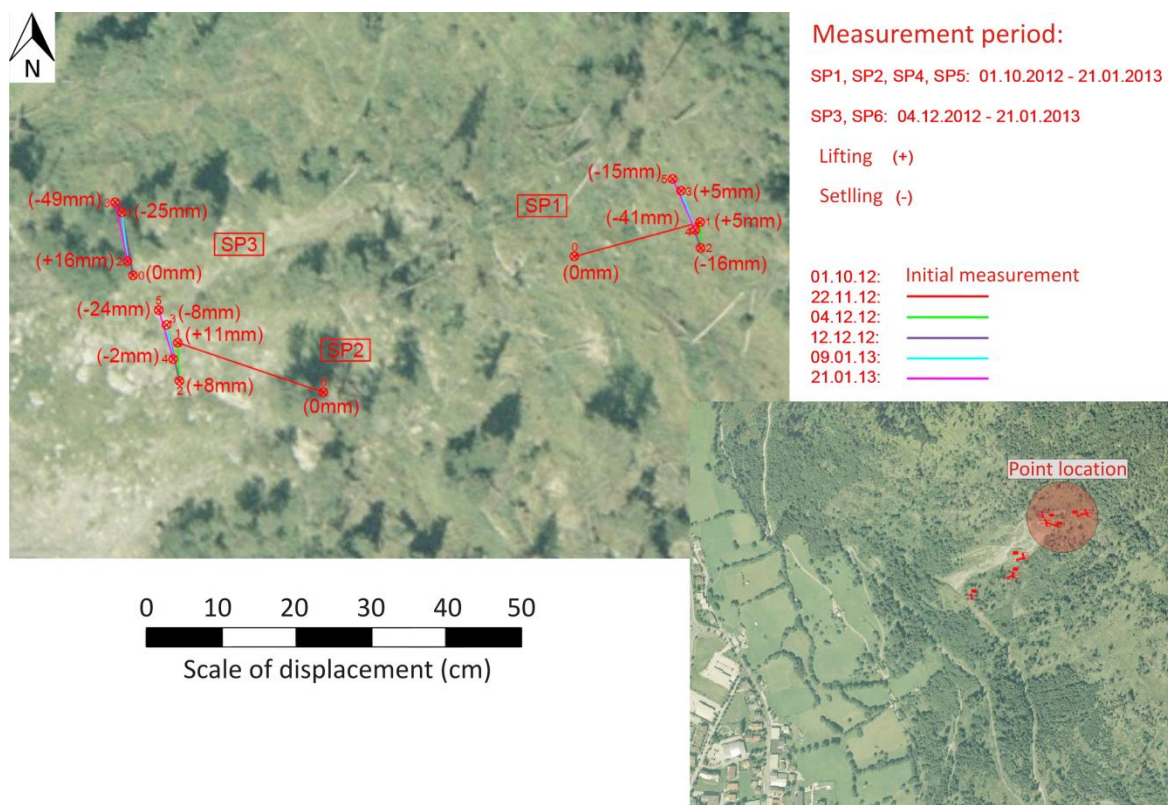


Figure 65, Exemplary total station measurements of Points 1, 2 and 3 and their direction of movement, after (Wilhelmstötter, 2013)

significant liftings (up to 59mm within one month), which are not comprehensible with the observations in the field and other measurement methods (Wilhelmstötter, 2013). Generally a movement towards the valley (to the West) would be expected, as indicated by tensile cracks in the head area and the morphology in general (Wilhelmstötter, 2013). Due to the insufficient measurement accuracy a comparison with GBInSAR measurements was not executed.

6.4 Interpretation

6.4.1 Phase 1 (27.03. – 01.05.2013)

General displacement patterns occurred repeatedly throughout the entire monitoring campaign, showing constant movement within depositional or talus areas. These displacements do not represent an unexpected or hazardous behavior, as movement is easily enabled within loosened debris. Generally these displacements were considered a shallow erosional process, caused by heavy rainfalls and by constant deposition of debris on top of the talus. This kind of displacement process had to be considered to distinguish between regular depositional displacement and hazardous displacement, caused by mass movements.

For a better understanding of the slope behavior during the distinctive rock fall event on April 29th 2013, a comparison of radar images and photographs was executed. In Figure 66 the debris track, the detachment and debris accumulation areas are highlighted. The detachment area is located within a strongly jointed sector at the uppermost head area. Following an already established erosional rill the detached material gets deposited on the lower left and right talus, as well as on the middle bench. As displayed in the radar map magnifications of Figure 66 debris accumulations form typical fan shapes, which match perfectly with the observations in the field. According to the camera images most of the debris came down within the right rill, though a small percentage followed the left deposition track, which is also detected by the displacement map. In compliance with eye witnesses and the camera images the main rock fall took place at around 17:00 on April 29th, whereupon several blocks fell down until 18:15. During this time multiple rock

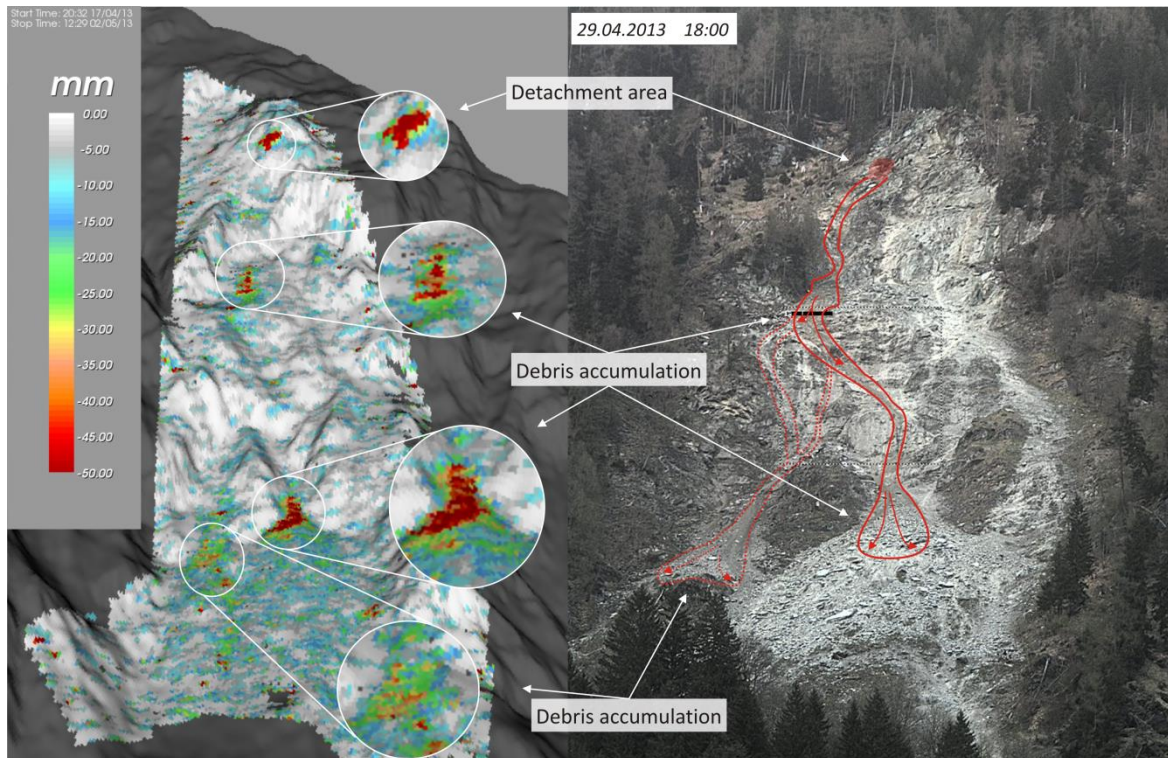


Figure 66, Left image displays the calculated displacement map during the rock fall event. Right image is taken by the fixed camera in the valley one hour after the rock fall occurred. Detachment and debris accumulation areas are highlighted and linked between the two images. Displacement scale shows movement towards the radar from 0mm (white) to -50mm (red). The main debris track is indicated by red lines, the secondary track is indicated by dashed red line.

fall notifications were made at the local police station and a dust cloud covered the lower areas.

Basically a rock fall of this size does not pose a serious threat, as most of the detached material came to rest on the talus. Only a few single blocks with a size of <math><1\text{m}</math> descended until the first rock fall dam, though none of them exceeded this barrier.

Displacement time series do not suggest a collapse of rock material, but rather stabilization on April 29th 2013 (Figure 67), as completely detached material would result in a positive displacement (away from the radar). A possible explanation for this result would be a rock fall located on the boundary of measurement pixels. Small rock falls would then affect only parts of each measurement pixel producing an averaged displacement curve. This phenomenon would be possible for small scale events as measurement pixels at the head area have a dimension of approximately 5.28m x 0.75m at 1.2km distance. Anyhow, camera images, eye witnesses and a field survey definitely prove a collapse of rock material.

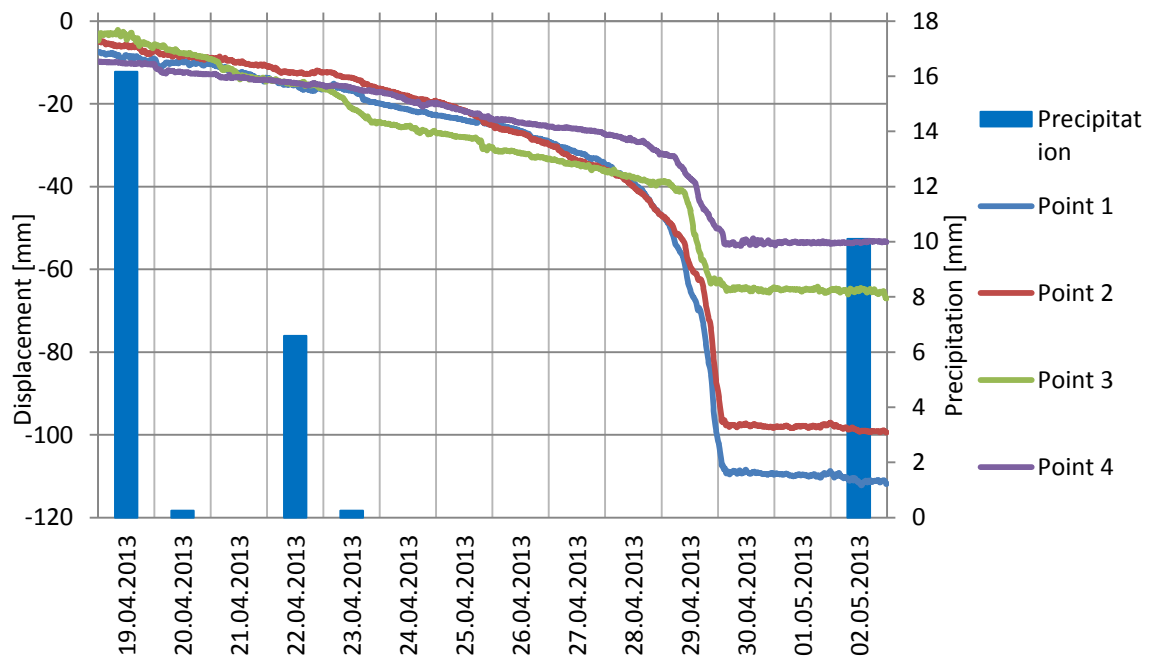


Figure 67, Time series of measurement pixels during the rock fall event of April 29th 2013; Pixels are located within the detachment area and plotted against measured precipitation

According to the fixed weather station at the radar shelter no distinctive rainfall event was recorded for the six days before the rock fall took place. Heavy rainfall occurred on April 19th 2013, which is supposed to be an initial trigger for the rock fall, as movement started to accelerate since this date and continued until a final collapse (Figure 67). On April 29th weather was warm and windy, but no rainfall occurred.

The shallow character of the rock fall could be proved within the site investigation performed three days after the event. The highly jointed and partly eroded blocks in the head area and the continuous erosion at the toe of this steep area lead to an irreversible loosening and collapse of blocks. Tilted blocks may crumble in pieces or collapse as a whole. To gain a rough estimate of the dimension of the collapse, Figure 68 indicates the detached volume with an approximation of 20-40 m³. The complete decomposition of the former fabric and the slight dipping towards the valley is supported by the bending or toppling mechanisms based on a 'hart auf weich' scheme as proposed by Wilhelmstötter (2013).



Figure 68, Shaded area refers to the detached material at the head area. An approximate volume of 20-40 m³ was estimated. Potentially collapsing blocks can be seen underneath the two trees.

6.4.2 Phase 2 (03.05.2013 - Present)

The second monitoring phase of the Ingelsberg indicated similar erosion patterns as phase 1, not displaying significant changes of occurred movement within the talus. A focus was put on the head area, as it repeatedly acted as the source of major rock falls (Wilhelmstötter, 2013), as well as on the middle bench wall (Figure 69). Additionally emphasis was put on the confining sector in the South of the active area on the transition to forested area. Due to decreasing coherence of measurement data in this zone, investigation was limited and delivered only a slight insight in slope behavior of this ridge.

Figure 69 displays location and averaged time series of the *head area* and the *middle bench wall*. Due to the almost vertical gradient and the generally existing joint sets at the *middle bench wall* (Wilhelmstötter, 2013) the potential of a detaching rock mass was evaluated. Displacement was only detected on a very small and almost cyclic scale. Over a period of three weeks oscillations within 1mm represent more likely a thermal effect or atmospheric artifacts, than any kind of hazardous behavior.

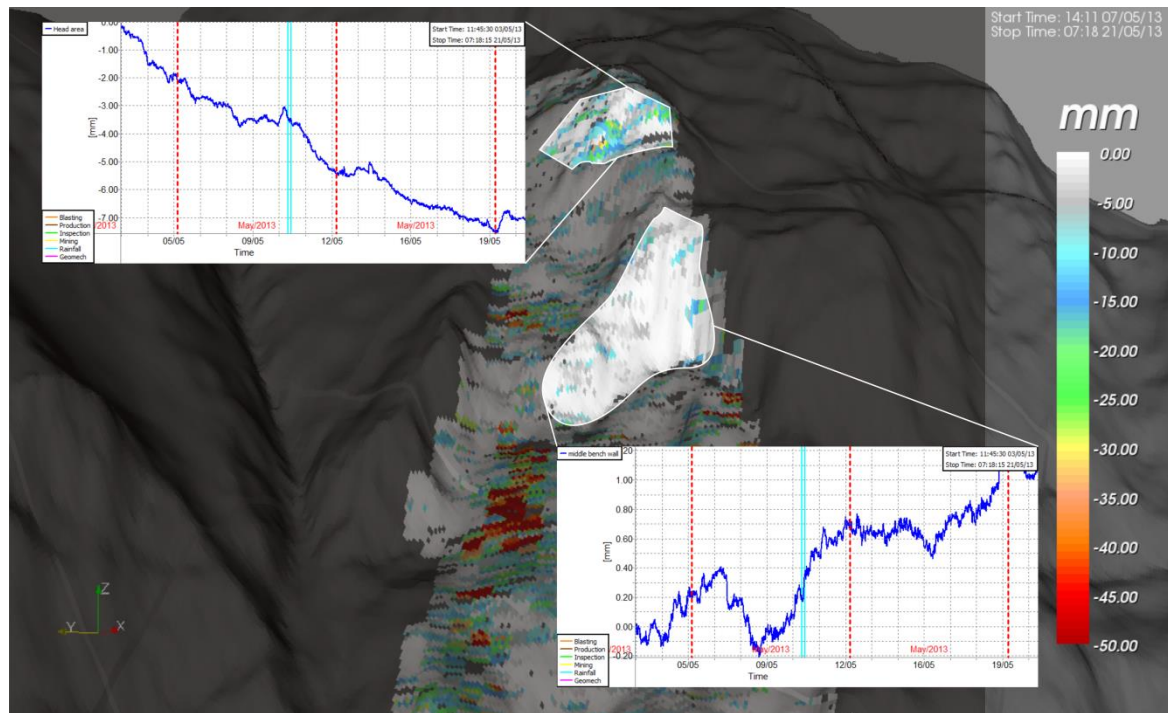


Figure 69, Location and according Time Series of upper focusing area '*head area*' and lower focusing area '*middle bench wall*'. Turquoise bar indicates a major rainfall with accumulated precipitation of 50mm.

A detailed analysis of the *head area* showed the development of a new slowly moving area just right to the prior rock fall zone. Additionally displacement continued within the older rock fall source area and displayed clear movement tendencies with averaged 25mm during 19 days. In Figure 70 time series of selected pixels in the *head area* are plotted against precipitation, whereupon no significant influence of the occurred rainfall is detectable. Developments of such time series resemble those detected before the rock fall event of April 29th and thus have to stay in the focus of upcoming measurements. Detected displacements concentrate on a few pixels and indicate movements of unstable blocks, comparable with the already occurred rock fall. The main part of illuminated pixels in the head area remains stable to sporadically slightly moving and does not deliver any indications of a large-scale collapse within the head area during this investigation.

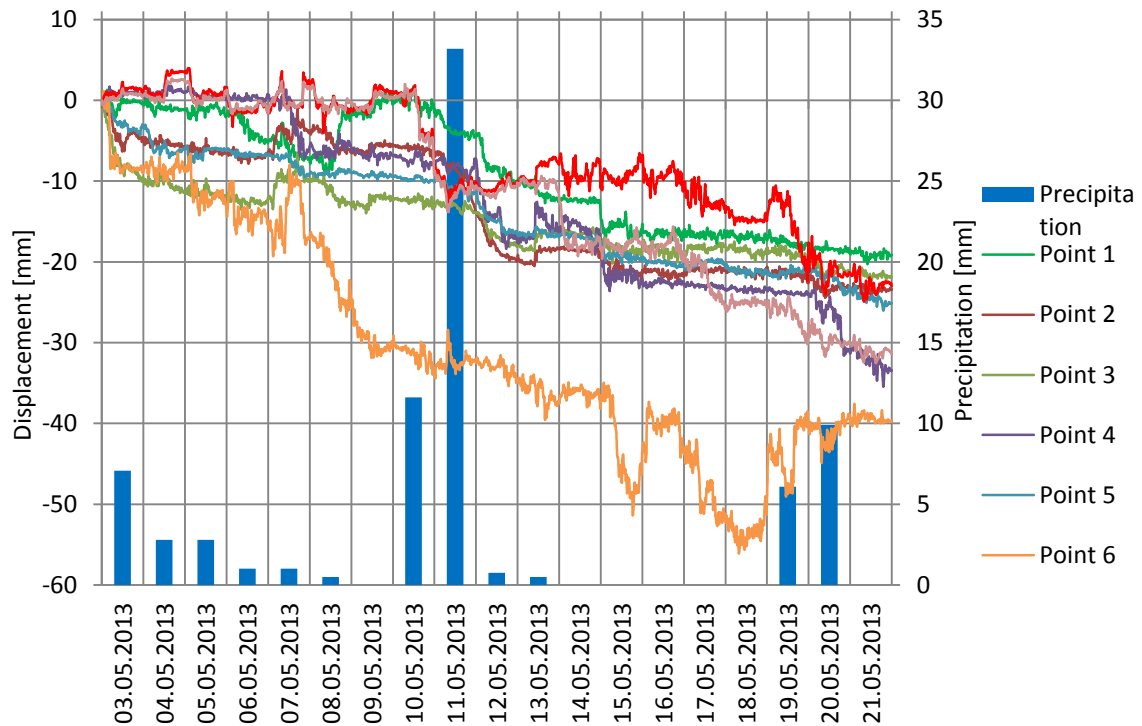


Figure 70, Displacement of selected pixels within the *head area* plotted against precipitation per day.

Vegetation prevented an extended analysis of the confining ridge to the south of the actively sliding area, due to the insufficient coherence of measurement data. Interpretation of results is only possible for slightly vegetated parts along the ridge. As occurred movement focuses on a few clearly defined spots, no evidence for overall displacement of the ridge is given. Possible movement further to the right remains unobserved, since vegetation inhibits a reliable investigation.

In the end of May and the beginning of June the entire federal state of Salzburg suffered of catastrophic rainfalls, which caused several debris flows and devastating floodings. During these days approximately 150mm of rain fell within 4 days (30.05-02.06 2013) at the Ingelsberg. Due to the enormous rainfalls the uppermost soil and debris cover of the Ingelsberg became extremely saturated with water. As a result several earth and debris slumps and smaller debris flows developed, showing significant displacement values (up to -400mm).

The fixed camera of the head area clearly displayed a shallow earth slump on June 2nd, causing an averaged displacement of 100mm within the radar time series. More precisely a soil cover of roughly 25-35 m² detached of the bedrock and slid down (see Figure 71). No major rock fall occurred during these days, although detected displacements exceeded former displacements in terms of dimension and extent. Summarizing, these rainfalls significantly increased displacement values at talus and depositional areas, whereas rock walls and the head area remained stable.

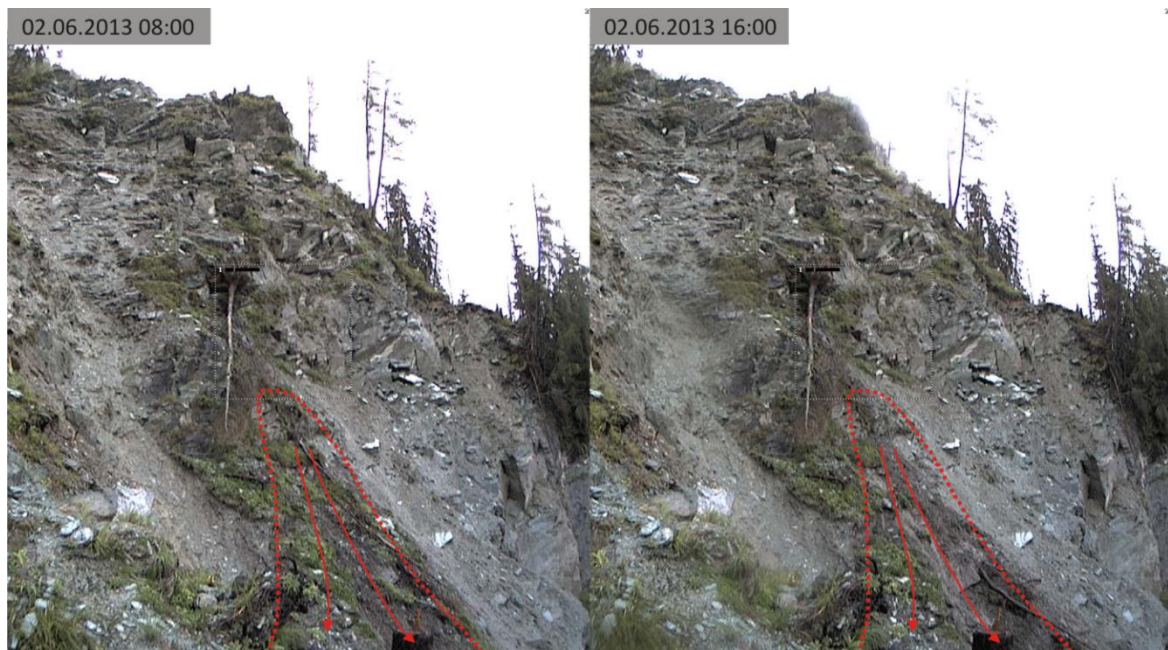


Figure 71, Images of the fixed camera at the head area during 02.06.2013; left image was taken at 08:00; right image was taken at 16:00 displaying a newly developed earth slump (red dashed line)

During the same time interval (30.05-02.06 2013) two major earth flows developed south of the investigation site, within vegetated area (Figure 72). One flow occurred right beyond the confining ridge in the south of the monitored area within very steep terrain (>40°). As this sector is also highly affected by unstable slope behavior, visible in numerous deeply penetrating cracks and tilted trees, an inclusion of this area into the monitoring program should be evaluated. The second earth flow developed on a steep meadow 300-400m south of the investigation site. Both flows stopped before reaching any protective structures or buildings.



Figure 72, Shaded area indicates the study area illuminated by the radar beam. Framed areas to the right display recently developed earth flows after the extreme rainfalls of June 1st and 2nd 2013.

Summarizing a radar map of the entire phase 2 (Figure 73), including the most recent data (03.05.-14.10.2013), displays the overall movement of the study site and enables a distinction in zones of continuous displacement trends. Highest displacements were consistently measured within the major talus in the lower part of the investigation area. Measured displacements in the talus areas, as well as on the middle bench, are a result of accumulated debris. Additionally displacement was detected below the head area, where the development of an earth slump caused displacement values of up to -100mm.

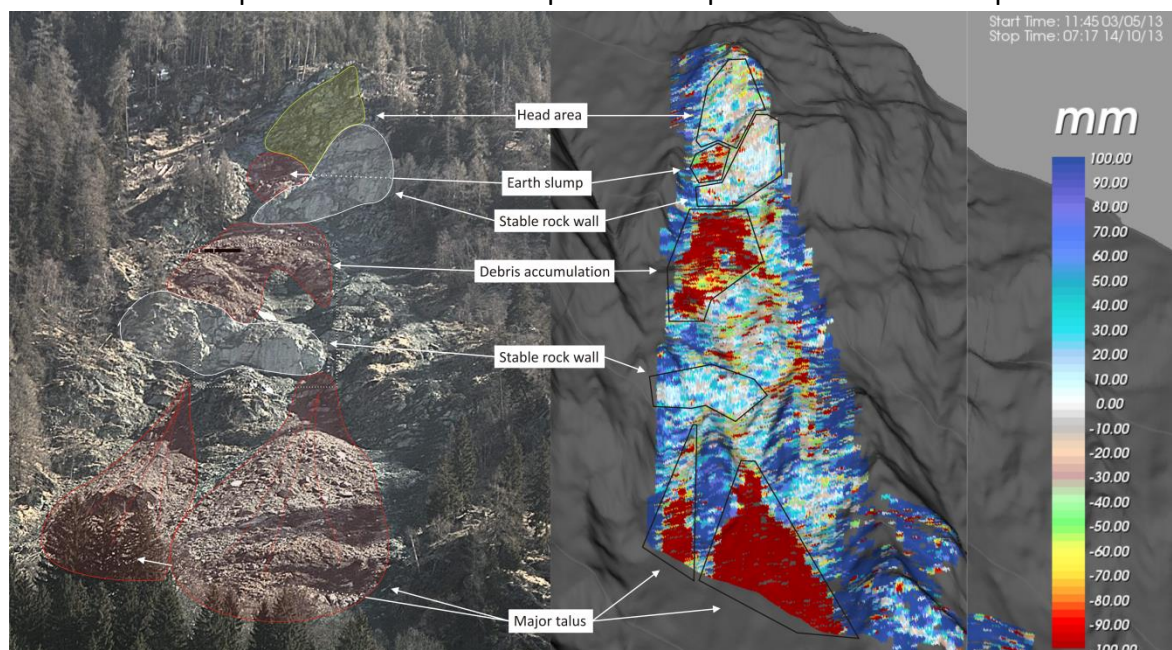


Figure 73, Comparison of a photograph and a radar map of entire phase 2 (03.05.-14.10.2013) using a scale bar ranging from +100mm to -100mm. Areas with continuous movement trends are highlighted.

No or little displacement was continuously measured on the two stable rock walls (Figure 73). Detailed analysis of their time series indicated oscillating movement within a few mm, but no distinct trend of movement. The head area acted as the source of distinctive rock fall events, whereas no large scale trend of movement was detected. Apart from a few detaching pixels the majority of measurement pixels in the uppermost part of the investigation area remained stable to slightly moving. The possible source areas of accumulated debris of the talus areas are displayed in blue colors in Figure 73 and are located at the boundary of the masked study site and between the major talus, respectively. Detected movement patterns do not represent a significant hazard, as rock walls and the head area remain stable to slightly moving. High displacement rates in talus areas are caused due to accumulation of debris, representing a common erosional behavior.

6.4.3 Slope Failure Prediction

The prediction of time of slope failure is of highest interest during all landslide monitoring campaigns to avoid fatal casualties, reduce damage to properties and initiate effective countermeasures (Federico et al., 2011). Different approaches have been developed during the last decades to give reasonable estimations for the time of slope failures. Usually an interpretation of monitoring data, more precisely of measured displacements and velocities, is applied to estimate the onset of failure (Federico et al., 2011). Regression techniques based on empirical functions provide the best fitting models to state any outlook (Federico et al., 2011). One already established method for predicting slope failure is the so called inverse velocity method proposed by Fukuzono (1985). This method was successfully applied on several natural and man-made slopes. Rose and Hungr (2007) presented three case studies of open pit mines in the USA proving the enormous advantage of an adequate failure prediction. In most cases monitoring data requires a certain smoothing to filter out instrument errors or obvious noise, like thermal or atmospheric effects (Rose and Hungr, 2007). However, data manipulation represents a delicate issue and has to be performed with care to avoid loss of useful information.

Fukuzono (1985) proposed a linear correlation of the logarithm of surface displacement acceleration and the logarithm of surface velocity, based upon numerous laboratory tests. If inverse velocity ($\frac{1}{v}$) was plotted against time, values of inverse velocity approached zero with an increasing velocity towards failure (Rose and Hungr, 2007). Therefore, an inserted trend-line through all inverse velocity values cuts the x-axis predicting the approximate time of failure (at zero inverse velocity). Fukuzono (1985) proposed three different types of plots (concave, convex and linear) using the following equation:

$$\frac{1}{v} = [A(\alpha - 1)]^{\frac{1}{\alpha-1}} * (t_f - t)^{\frac{1}{\alpha-1}} \quad (9)$$

Using Equation 9 the time of failure t_f can be calculated by inserting the constants A and α . Laboratory tests indicated α to range between 1.5 and 2.2 with $\alpha=2$ to plot as linear trend predicting an adequate estimate of time of failure. The inserted curve fitting through inverse velocity is concave if $\alpha < 2$ and convex if $\alpha > 2$. Prediction of failure time works best under creep type conditions, as Fukuzono (1985) simulated creep failures on sand and loam slopes with angles between 30° and 40°.

In Figure 74 an exemplary case is displayed using velocity values of the rock fall event of April 29th 2013. Due to the fast monitoring intervals of 5-7 minutes and the accompanying fluctuations of measured velocity data smoothing was required. The median of 6h intervals of velocity was calculated to eliminate potential outliers and to get reasonable time intervals. Certainly data handling is very delicate and has to be executed with great care to avoid losing crucial information. For the inserted linear trend-line equations and R^2 regression coefficient can be accessed and further used to calculate time of slope failure. All displayed failure predictions were generated after the rock fall took place.

Generally time of slope failure prediction is most valuable, when executed as early as possible. The linear prediction displayed on the left side in Figure 74 was therefore generated using inverse velocity data of April 22nd to 24th 2013. Time of slope failure was then predicted at 05:13 on April 25th 2013 with a R^2 value of 0.33. As the real rock fall occurred at 17:00 on April 29th 2013 a prediction error (Δ) of approximately 108 hours is

given. The linear prediction on the right side in Figure 74 uses inverse velocity values ranging from April 22nd to April 28th 2013. Slope failure was predicted at 12:00 on April 29th 2013 with a R^2 value of 0.35, showing a prediction error (Δ) of 5 hours. Although correlation coefficient R^2 remains relatively low in both predictions, the need for a continuous or real time monitoring is shown with the highly differing predictions. As inverse velocity values close to the actual failure deliver the best fitting prediction only real-time monitoring data allows a precise and useful prediction.

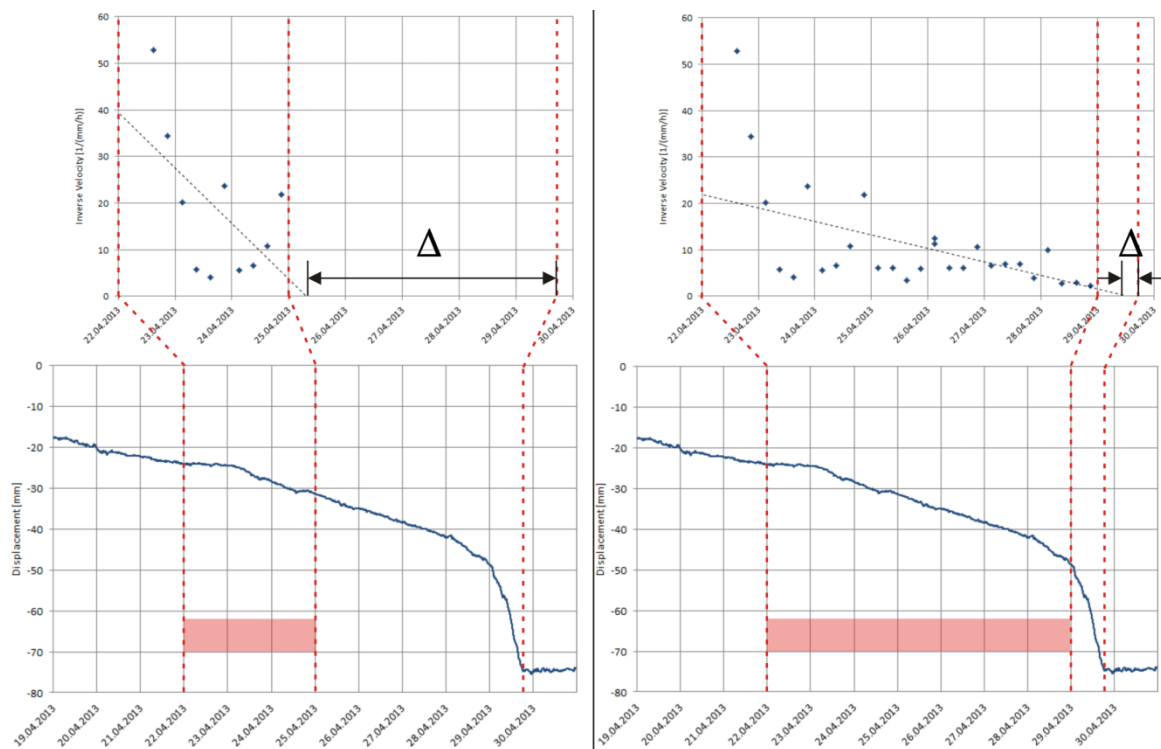


Figure 74, Averaged 6h intervals of measured inverse slope velocity displaying best fitting linear trend-line. Red shading indicates time span of used data set, left graph displays prediction using data from April 22nd to 24th 2013., right graph displays prediction using data from April 22nd to 28th 2013. Δ indicates prediction error between predicted and real event.

Summarizing, Fukuzono's approach provides a highly useful method for predicting the time of slope failure, if adequate monitoring data is available. Additionally data smoothing requires a particular expertise to retrieve best possible results of slope monitoring data.

7. Summary & Conclusions

7.1 Hornbergl

On September 19th and 20th 2012 the IBIS-L/IBIS-FL equipment was installed next to Höfen to monitor unstable slopes at the Hornbergl. Due to multiple monitoring campaigns executed at the Hornbergl general information about failure mechanisms and movement tendencies was available for planning a radar monitoring campaign. Nevertheless, none of the already applied measurement methods delivered comprehensive or real time information about slope behavior.

The radar was mounted on a foundation already established by Schares (2012). Monitoring was initiated on September 20th 2012 and completed on December 11th 2012. After the beginning of GBInSAR monitoring a field investigation was performed to gain a better overview of the geology and morphology of the site. Extensive literature research and measurement data of other monitoring campaigns supported the understanding of slope behavior at the Hornbergl.

After two weeks of monitoring distinctive movement patterns within depositional areas were detected and continued until the end of the measurement campaign. Low coherence values within vegetated areas constrained reliable measurements to rocky or sparsely vegetated sectors.

Distinct areas of movement could be defined during radar monitoring. A constant accumulation of debris was observed within all talus areas and along the steep cliffs of the south-east striking ridge. Small displacing sectors could be identified within the steep cliffs of the south-east striking ridge, whereas none of them represented a serious hazard in area. A sector of movement was detected at the toe of the actual Hornbergl with pixels displacing repeatedly throughout the entire measurement campaign. No clarification of the causing mechanism, either a shallow erosional process or deep seated movement, could be made. No evidence for an extensive rock fall could be found during this short-term monitoring and represents therefore a very unlikely event during this time of year (September-December). Movement rates usually accelerate during spring and summer with a higher possibility of rock fall events to occur in this time (Glabsch et

al., 2009, Moser et al., 2009). Displacement data of the executed GBInSAR investigation do not indicate a collapse of rock pinnacles along the ridge or extensively detaching areas within steep walls of the Hornbergl or the south-east striking ridge during the short period of this measurement campaign. However, future GBInSAR campaigns can be a powerful tool to understand slope behavior on a long-term scale.

7.2 Ingelsberg

With an increased landslide activity during the last few years the Ingelsberg came into the focus of several monitoring programs. In summer 2012 fixed cameras, fissurometers and geodetic measurement points were installed to provide better prediction and control of possible slope failures (Wilhelmstötter, 2013). The above stated measurement methods rely on selective measurement points and have limitations in defining the extent of the unstable area. Therefore, radar monitoring was initiated to acquire comprehensive displacement data of the entire study site and to gain a better understanding of the slope behavior.

During March 2013 preparatory work was executed (e.g. construction of a foundation and shelter) to provide ideal requirements for the installation of the IBIS-L/IBIS-FL equipment. Monitoring started on March 27th 2013 and continues presumably until the end of 2013. Ten corner reflectors were mounted within the investigation site to provide a stronger signal and to support the distinction between vegetated moving and stable areas.

Within a few days of monitoring, displacement on two major talus areas in the lower part of the study area was detected by radar measurements. Additionally a debris accumulating area was defined on the middle bench of the study site, showing distinct movement. As suggested by other monitoring methods the uppermost head area proved its activity with a distinctive rock fall on April 29th 2013. Time series displayed the onset of failure ten days in advance with a continuous acceleration of measurement pixels towards the rock fall. Finally an approximate volume of 20–40m³ of rock detached and descended until the lower talus and the first dam, respectively.

During May 2nd 2013 the readjustment to the most recent performing IBIS-FL version was executed. Monitoring resumed on May 3rd with the advantage of lowered measurement intervals (7 to 2.5 minutes).

Phase 2 of the investigation resembled phase 1 in most of the occurred movements. Highest displacements were measured within the lower talus areas and on the middle bench. Similar to the rock fall event of April 29th 2013 continuous movement was detected in the head area, without displaying acceleration of displacement or a distinctive rock fall event. Other parts of the head area, as well as the confining ridge to the south of the active area were investigated regarding their possibility of slope failure. However, no indication for extensive detachment of rock masses could be found within the observed areas. Occurred displacement mainly focused on the talus and the erosional tracks between the talus. Even the extreme rainfalls during June 1st and 2nd 2013 did not trigger a major rock fall within the investigation site. With the onset of warm and dry weather in the mid of June movement rates decreased and displayed consistently stable behavior.

A correlation of displacement data and meteorological information proved intense rainfall as a trigger for accelerating displacement. Especially loosely accumulated debris displayed clear response to rainfall, but also the rock fall of April 29th 2103 showed a correlation with high precipitation values.

To crosscheck acquired radar results a correlation with fissurometer measurements was performed. In the precise case of the rock fall event of April 29th 2013 exact correlation of highly sensitive fissurometers was executed. Only fissurometer close to the escarpment of the head area were suitable for comparing radar and fissurometer results, due to their high sensitivity against precipitation (Wilhelmstötter, 2013). Similar movement tendencies, as well as starting and ending times could be proved for the particular rock fall of April 29th 2013.

One chapter of this thesis aims at a prediction of time of slope failure using the approach presented by Fukuzono (1985). By plotting the inverse velocity of monitored slope displacement an estimate of the time of failure can be stated, delivering a necessary time span to initiate adequate countermeasures. Depending on the extent of used

measurement data and on the type of data smoothing post-failure predictions were calculated for the rock fall of April 29th 2103 displaying prediction errors between 108 hours and 5 hours.

Summarizing, displacement focused on depositional areas, which do not represent a major hazard. Smaller rock fall events occurred during the monitoring campaign, showing the potential danger of the collapsing head area. Wilhelmstötter (2013) attested the currently existing dams and rock fall nets a reasonable protection of rock fall events with a volume of 1.000m³. Rock falls with the dimension of 10.000m³ would most likely ascend until the valley floor, representing an intolerable risk to human life, private properties and infrastructure (Wilhelmstötter, 2013). However, during GBInSAR monitoring no evidence could be found for such a large volume to detach. Protective structures appear sufficient regarding its current dimension and location. Nevertheless, monitoring via fissurometers and camera images has to be continued to detect potentially accelerating displacement in the head area.

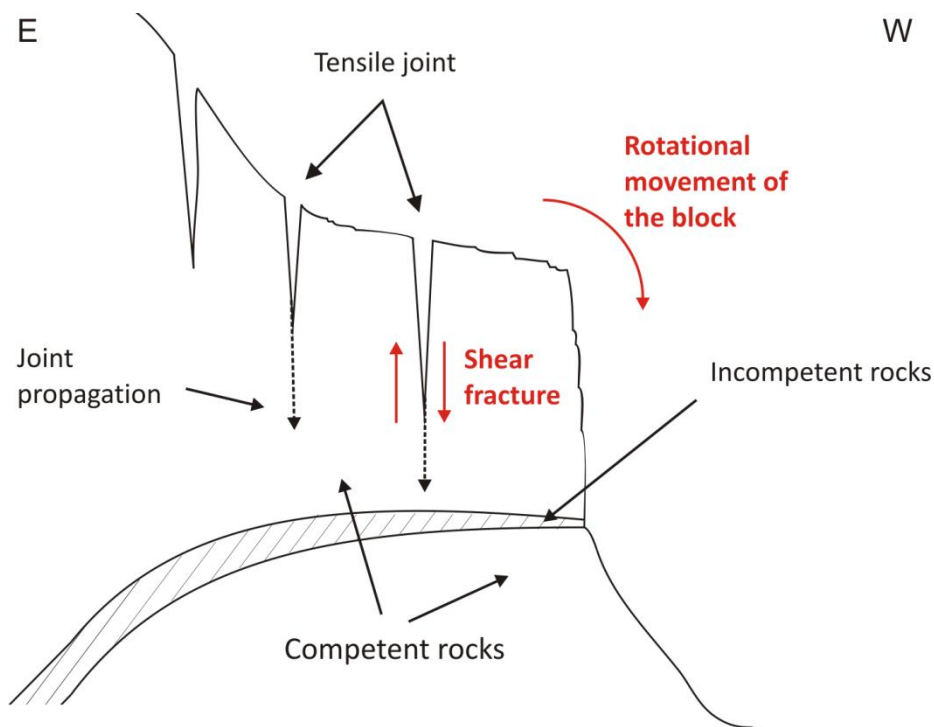


Figure 75, Schematic diagram (E to W) of the block failure mechanism proposed by Wilhelmstötter (2013) following the principle of 'hart auf weich'. Incompetent rocks refer to black phyllites and competent rocks to metabasic rocks and calc-mica schist.

(Wilhelmstötter, 2013) suggested an overall bending of rock units based on the 'hart auf weich' scenario as the destabilizing process at the Ingelsberg. In this scenario incompetent rocks (Black phyllite) provide a soft and deformable underground on which competent rocks (Calc-mica schist and metabasic rocks) split into stiff and unstable blocks. However, a deep and overall bending of rock units due to the black phyllites, which are mainly encountered in the lowest parts of the study area, is difficult to explain. A mechanism called pseudo-sheeting is a more realistic explanation for the unstable slope behavior (Kieffer, 2013). In this scenario an alternate bedding of competent and incompetent rocks enables the generation of vertical joints due to stress relief and missing overburden (Figure 76). These release joints may form unstable, often collapsing, blocks. In contrary to the overall bending proposed by Wilhelmstötter (2013) this pseudo-sheeting mechanism represents a near-surface process of instability due to stress relief. GBInSAR measurements support this scenario as displacements are limited to distinct sectors and do not indicate an overall movement of entire investigation areas (e.g. head area).

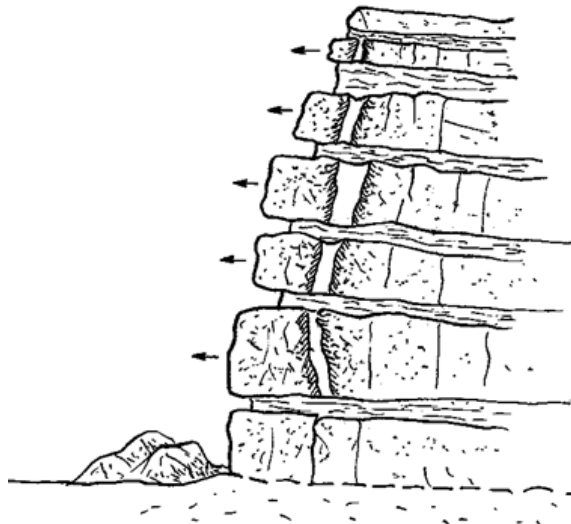


Figure 76, Pseudo-sheeting mechanism caused by stress relief within alternating bedding of competent and incompetent rocks (Kieffer, 2013).

Concluding it has to be stated that this Master's Thesis is a scientific paper and only implies certain recommendations. Any suggestions regarding the general slope behavior, the protective structures or other countermeasures evolved from the GBInSAR investigations. Before initiating any further arrangements the expertise of a specialist has to be acquired and more detailed inspections have to be performed.

8. Appendix

8.1 List of Figures

Figure 1, Resolution cells GBInSAR (Kurka, 2012); graphics from IDS, 2011	4
Figure 2, Pulse Radar working principle (Coppi, 2011)	5
Figure 3, Range resolution concept (Coppi, 2011)	5
Figure 4, Synthetic pulse with bandwidth B and frequency steps Δf using SF-CW, modified after (Schaes, 2012)	6
Figure 5, Idealized range measurement along a profile with several targets showing the amplitude of the echoes (Coppi, 2011)	7
Figure 6, Illustration of the pixel resolution defined by range resolution ΔR and cross range resolution ΔCR (Coppi, 2011)	8
Figure 7, Different stages of focusing during the generation of a GBInSAR image (Amplitude only); (Rödelsperger, 2011)	9
Figure 8, Distortion of measurement cells due to the projection on a three-dimensional system (Coppi, 2011)	10
Figure 9, Principle of interferometry (Coppi, 2011)	12
Figure 10, Different types of radar reflectors (Rödelsperger, 2011)	14
Figure 11, IBIS-FL equipment mounted on a concrete foundation in Bad Hofgastein	15
Figure 12, Power map (a); Signal to noise ratio (SNR) map (b); Coherence map (c); Selection mask (green) applied onto the coherence map of the Ingelsberg investigation (d). Bright areas indicate highly coherent pixels and represent rocky or sparsely vegetated areas.	18
Figure 13, Location of the Hornbergl study area within Austria, Scale 1:2 000 000 (BEV, 2013)	21
Figure 14, The Hornbergl seen from the valley (view looking SW). The ‚Höfener Kreuz‘ is located at the right edge, whereby the south-east striking ridge and its confining cliffs can be seen at the left.	22

Figure 15, Hornbergl study area indicated with white shading, Scale 1:50 000 (BEV, 2006)	22
Figure 16, Earthquake hazard map of Tyrol (ZAMG, 2013a).....	23
Figure 17, Regional geological map of the area around Reutte, Scale 1:50 000, modified after (GBA, 2009).....	24
Figure 18, Typical alternating layers of limestone and marly interbeds of the ' <i>Alpine Muschelkalk Gruppe</i> '	25
Figure 19, Geological site map of the Hornbergl, Scale 1:500, modified after (Kirschner, 2006).....	26
Figure 20, Schematic profile along the south-east striking ridge at the Hornbergl; this general model includes the development of rock slides along the bedding planes at the dip slope. On the contrary the formation of rock pinnacles at the scarp slope and the formation of graben-like structures at the ridge are implied. 'Competent rocks' refer to the limestone layers of the alpine shell limestone unit, 'Incompetent rocks' to the Reichenhall formation; modified after (Kirschner, 2006, Meier et al., 2009)	27
Figure 21, Freestanding rock pinnacle on top of the ridge; 5m deep crack along the ridge	28
Figure 22, Result of the debris flow of May 2.-5. 1986 (Photograph taken by Dr. Dragosits in 1986, WLV, Ausserfern).....	29
Figure 23, Cumulative displacement between 01.01.1988 – 21.05.2007; Arrows indicate direction and dip (purple colors) of movement; Colors indicate interpolated vertical displacement between +3m (red) and -3m (blue), modified after (Marschallinger et al., 2010).....	31
Figure 24, Location of the Ingelsberg study area within Austria, Scale 1: 1 000 000, (BEV, 2013).....	32
Figure 25, Ingelsberg study area indicated with white shading, Scale 1:50 000 (BEV, 2006)	33

Figure 26, The Ingelsberg, seen from the Gastein valley and the position of the radar (view looking E). The framed area shows the unstable area and the encircled parts represent interpreted previously detached blocks.....	34
Figure 27, Tectonic overview of Salzburg, Scale 1:1 000 000, modified after (Pestal et al., 2009).....	35
Figure 28, Earthquake hazard map of Salzburg (ZAMG, 2013a)	36
Figure 29, XRD analysis of a black phyllite sample (UK2). Minerals identified: Quartz, Muscovite, Chlorite, Calcite and Talc. Axis <i>Counts</i> refers to intensity of detected backscattered signal and <i>2Theta</i> position refers to the interplanar distance d [Å].	37
Figure 30, Geological site map of the Ingelsberg, Scale 1:2000, modified after (Wilhelmstötter, 2013).....	38
Figure 31, Fixed reflecting prism at the upper part of the Ingelsberg; Installed fissurometer inside one of the major cracks at the top of the Ingelsberg	41
Figure 32, Image at the top left shows the upper head area; image at the top right shows the dam at the toe with accumulated debris; bottom image shows the entire investigation area; (Images taken on 29.04.2013).....	42
Figure 33, Using the positioning template for drilling the holes; resin injected holes with fixed threaded studs and base washers; detail of the installed rail.	43
Figure 34, The tilted radar head mounted on the 'elevation pointing system' using several spacers for ideal positioning.	44
Figure 35, To avoid the measurement of LoS displacement the orientation of the radar beam must be aligned as accurately as possible to the direction of real displacement (d_{real}).	44
Figure 36, Position of the IBIS Radar next to Höfen for investigating the Hornbergl. Red shaded area refers to illuminated area; LoS resembles the direction of measurement. White line indicates area of previous measurement campaigns; arrows indicate previously measured direction of movement.....	45
Figure 37, Overview of the masked area at the Hornbergl without any processed displacement. Red shaded areas indicate depositional areas/talus.....	46

Figure 38, Investigated area projected on the used aerial laser scan DTM. Yellow box indicates position of the radar, arrows indicate possible direction of displacement and further transportation within the Murenbach (View looking SW).	46
Figure 39, Completely installed IBIS-FL radar at Reutte within the equipment shelter. ...	47
Figure 40, Location of repeatedly measured displacement at the Hornbergl. Displacement occurred within the talus and at the toe of the Hornbergl, as well as during a small-scale event within the steep rock walls. Image covers the complete duration of the measurement campaign (19.09. – 11.12.2012) and displays accumulated displacement over this time span. Displacement pixels in the lower left corner refer to a highly vegetated area and therefore lack a necessary reliability of acquired data.....	48
Figure 41, Characteristic example of measured displacement plotted against precipitation. Top graph refers to the toe area of the Hornbergl, bottom graph refers to the main talus at the Hornbergl. Both time series show strong correlation to measured rainfalls.	49
Figure 42, Characteristic small-scale example of measured displacement within a few pixels located at the steep confining wall along the south-east striking ridge. Displacement shows strong correlation with the rainfalls at the beginning of November.	49
Figure 43, Long term measurement data for the entire study area (e.g. convergence and geodetic measurements); Cumulative displacement between 01.01.1988 – 21.05.2007; Arrows indicate direction and dip (purple colors) of movement; Colors indicate interpolated vertical displacement between +3m (red) and -3m (blue), modified after (Marschallinger et al., 2010)	51
Figure 44, Areas with repeatedly detected displacement. Three distinctive zones may be classified: talus showing the accumulation of debris, a displacing area at the toe of the Hornbergl and a small-scale event within the steep rock walls. Displacement pixels in the lower left corner refer to a highly vegetated area and therefore lack a necessary reliability of acquired data.	52
Figure 45, Comparison of detected displacement and a photograph of the steep rock wall along the south east striking ridge. Possibly collapsing rock pinnacles, exemplary small-	

scale event and talus (debris accumulation) are marked with arrows (Measurement period 10.10.-30.11. 2012).....	53
Figure 46, Left photograph shows the Hornbergl in October 2012; right image displays the accumulated displacement of the entire investigation period. Displacement areas are highlighted and linked between the two images to gain a better understanding of the acquired data.....	54
Figure 47, Position of the IBIS Radar in Bad Hofgastein for investigating the Ingelsberg. Red shaded area refers to illuminated area, LoS resembles the direction of measurement and arrows (blue) indicate opening tendencies of previously monitored cracks.....	55
Figure 48, Installation of a corner reflector close to a fixed reflecting prism; Mounted corner reflector No. 8.....	56
Figure 49, Investigated area projected on the used aerial laser scan DTM (View looking E). Yellow box indicates position of the radar, shaded area roughly indicates the area of slope instability.....	57
Figure 50, Overview of the masked area at the Ingelsberg without any processed displacement. Red shaded areas indicate major talus.	58
Figure 51, Position of the onset of the main talus in the depositional area. P13-P24 are randomly scattered along the highly moving pixels. Displacement [mm] of selected points plotted against measured precipitation [mm].....	59
Figure 52, Time series of measurement pixels within the head area shortly before the stabilization. Final movement rates between two selected points reached up to 8.055mm/h. The negative value indicates a movement towards the radar. Movement stopped at around 17:00 on April 29 th 2013.....	59
Figure 53, Processed displacement map of the investigation site showing highly moving areas (head area, middle bench and depositional area) and its corresponding time series. Negative displacement values indicate a movement towards the radar. Displacement scale ranges from 0mm (white) to -50mm (red).....	61
Figure 54, Averaged time series of selected investigation areas at the <i>head area</i> and at the <i>middle bench wall</i> above the middle bench. Top graph displays movement away from	

the radar (+50 – 0mm), bottom graph displays moment towards the radar (0 – 50mm). The turquoise bar represents a major rainfall with 50mm of accumulated rain within two days (10./11.05.2013)	63
Figure 55, Time series of displacing and stable pixels within the <i>head area</i> . The turquoise bar represents a major rainfall with 50mm of accumulated precipitation within two days (10./11.05.2013).....	64
Figure 56, Selected time series of various measurement pixels along the right confining ridge of the masked area. The turquoise bar represents a major rainfall on May 10 th and 11 th with 50mm of accumulated precipitation. Top graph displays movement away from the radar (+50 – 0mm), bottom graph displays movement towards the radar (0 – (-)50mm).....	65
Figure 57, Extreme rainfall events during 22.05. – 03.06.2013	66
Figure 58, Displacement map during the time span of 22.05.-04.06.2013 displaying a significant acceleration of movement with the onset of extreme rainfall during 31.05-02.06.; Graph (a) shows times series of the head area with only minor impact of rainfall; Graph (b) and (c) are located within depositional areas and strongly respond to the rainfall. Graph (d) indicates a newly developing area of displacement at the lower part of the head area.	67
Figure 59, Displacement map of phase 2 including the most recent data (03.05.–14.10.2013). Used scale bar ranges from +100mm to -100mm. Plotted time series shows strong correlation of rainfalls and displacement in the lower talus. Turquoise bars represent rainfall events with more than 30mm/day.	68
Figure 60, Comparison of exemplary time series using different masks (ingels_exact & ingels_26_03)	69
Figure 61, Position of all 10 Corner Reflectors within the investigation area.	70
Figure 62, Calculated pseudo displacement of selected Corner Reflectors. α_{gcp} is a correction factor for each GCP. The bottom graph indicates the quality of the atmospheric correction (low values = high quality).....	72
Figure 63, Location of fissurometers F1, F2, F4, and F5.....	73

Figure 64, Top graph displays measured fissurometer displacement vs. precipitation; bottom graph indicates radar displacement vs. precipitation. Fissurometer 1 and 5 clearly correlate with detected movement at Points 1-4 in the head area.	74
Figure 65, Exemplary total station measurements of Points 1, 2 and 3 and their direction of movement, after (Wilhelmstötter, 2013)	75
Figure 66, Left image displays the calculated displacement map during the rock fall event. Right image is taken by the fixed camera in the valley one hour after the rock fall occurred. Detachment and debris accumulation areas are highlighted and linked between the two images. Displacement scale shows movement towards the radar from 0mm (white) to -50mm (red). The main debris track is indicated by red lines, the secondary track is indicated by dashed red line.	77
Figure 67, Time series of measurement pixels during the rock fall event of April 29 th 2013; Pixels are located within the detachment area and plotted against measured precipitation	78
Figure 68, Shaded area refers to the detached material at the head area. An approximate volume of 20-40 m ³ was estimated. Potentially collapsing blocks can be seen underneath the two trees.	79
Figure 69, Location and according Time Series of upper focusing area ' <i>head area</i> ' and lower focusing area ' <i>middle bench wall</i> '. Turquoise bar indicates a major rainfall with accumulated precipitation of 50mm.....	80
Figure 70, Displacement of selected pixels within the <i>head area</i> plotted against precipitation per day.	81
Figure 71, Images of the fixed camera at the head area during 02.06.2013; left image was taken at 08:00; right image was taken at 16:00 displaying a newly developed earth slump (red dashed line).....	82
Figure 72, Shaded area indicates the study area illuminated by the radar beam. Framed areas to the right display recently developed earth flows after the extreme rainfalls of June 1 st and 2 nd 2013.	83

Figure 73, Comparison of a photograph and a radar map of entire phase 2 (03.05.-14.10.2013) using a scale bar ranging from +100mm to -100mm. Areas with continuous movement trends are highlighted.	83
Figure 74, Averaged 6h intervals of measured inverse slope velocity displaying best fitting linear trend-line. Red shading indicates time span of used data set, left graph displays prediction using data from April 22 nd to 24 th 2013., right graph displays prediction using data from April 22 nd to 28 th 2013. Δ indicates prediction error between predicted and real event.....	86
Figure 75, Schematic diagram (E to W) of the block failure mechanism proposed by Wilhelmstötter (2013) following the principle of 'hart auf weich'. Incompetent rocks refer to black phyllites and competent rocks to metabasic rocks and calc-mica schist.....	90
Figure 76, Pseudo-sheeting mechanism caused by stress relief within alternating bedding of competent and incompetent rocks (Kieffer, 2013).	91

8.2 List of Tables

Table 1, Technical specifications of IBIS-L/IBIS-FL; modified after (IDS, 2012, IDS, 2013) .	16
--	----

8.3 List of References

- ALBA, M., BERNARDINI, G., GIUSSANI, A., RICCI, P. P., RONCORONI, F., SCAIONI, M., VALGOI, P. & ZHANG, K. 2008. Measurement of dam deformations by terrestrial interferometric techniques. *The International Archives of the Photogrammetry, Remote Sensing and Spatial Information Sciences*, Vol. XXXVII.
- ALBRECHT, T. 1999. Die Geologisch-Geotechnischen Verhältnisse im Einzugsgebiet des Herrenbaches – Reutte / Tirol. *unpublished Diploma Thesis*, Institut für Geologie und Mineralogie, Lehrstuhl für Angewandte Geologie, Universität Erlangen-Nürnberg.
- BAMLER, R. & HARTL, P. 1998. Synthetic aperture radar interferometry. *Inverse Problems*, 14, R1-54.
- BARLA, G., ANTOLINI, F., BARLA, M., MENSI, E. & PIOVANO, G. 2010. Monitoring of the Beaugard landslide (Aosta Valley, Italy) using advanced and conventional techniques. *Engineering Geology*, 116, 218-235.
- BEV 2006. Österreich Karte 1:50 000 der Bundesanstalt für Eich- und Vermessungswesen.
- BEV 2013. Amap Übersichtskarte 1:2 Millionen.

- BOZZANO, F., CIPRIANI, I., MAZZANTI, P. & PRESTININZI, A. 2011. Displacement patterns of a landslide affected by human activities: insights from ground-based InSAR monitoring. *Natural Hazards*, 59, 1377-1396.
- COLESANTI, C., FERRETTI, A., PRATI, C. & ROCCA, F. 2003. Monitoring landslides and tectonic motions with the Permanent Scatterers technique. *Engineering Geology*, 68, 3-14.
- COPPI, F. 2011. IBIS Image by Interferometric Survey - Working principles. <http://www.idscorporation.com/en/georadar>.
- FEDERICO, A., POPESCU, M., ELIA, G., FIDELIBUS, C., INTERNÒ, G. & MURIANNI, A. 2011. Prediction of time to slope failure: a general framework. *Environmental Earth Sciences*, 66, 245-256.
- FERRETTI, A., PRATI, C. & ROCCA, F. 2000. Nonlinear Subsidence Rate Estimation Using Permanent Scatterers in Differential SAR Interferometry. *IEEE Transactions on Geoscience and Remote Sensing*, 38, 2202-2212.
- FUKUZONO, T. 1985. A new method for predicting the failure time of a slope. *Proceedings of the IVth International Conference and Field Workshop on Landslides*, Tokyo, Japan Landslide Society, 145-150.
- GBA 2009. GEOFAST M1:50 000, 115 - Reutte. *Zusammenstellung ausgewählter Archivunterlagen der Geologischen Bundesanstalt*.
- GEODATA 2008. Fissurometer. *Data sheet hardware*, <http://www.geodata.at/deu/company/download/Fissurometer.pdf>.
- GLABSCH, J., HEUNECKE, O. & SCHUHBÄCK, S. 2009. Monitoring the Hornbergl landslide using a recently developed low cost GNSS sensor network. *Journal of Applied Geodesy*, 3, 179-192.
- HERRERA, G., FERNÁNDEZ-MERODO, J. A., MULAS, J., PASTOR, M., LUZI, G. & MONSERRAT, O. 2009. A landslide forecasting model using ground based SAR data: The Portalet case study. *Engineering Geology*, 105, 220-230.
- IDS 2012. IBIS_L v02.00 - User Manual. (Ingegneria dei Sistemi S. p. A.) www.idscorporation.com.
- IDS 2013. (Ingegneria dei Sistemi S. p. A.). www.idscorporation.com.
- JUNGNER, A. 2009. Ground-Based Synthetic Aperture Radar Data Processing for Deformation Measurement. *unpublished Master's Thesis*, Royal Institute of Technology, Stockholm.
- KIEFFER, D. S. 2013. Personal Communication. *Institute of Applied Geosciences, Graz University of Technology*.
- KIRSCHNER, H. 2006. Hornbergl Bericht zur geologisch-geotechnischen Untersuchung Bez. Reutte/Tirol Austria. *unpublished Mapping Report for Wildbach- und Lawinenverbauung*.
- KURKA, M. 2012. Introduction into Terrestrial Interferometry (TInSAR). *unpublished Report for Technical University of Graz*.

- LUZI, G. 2010. Ground based SAR interferometry a novel tool for Geoscience. www.intechopen.it.
- LUZI, G., NOFERINI, L., MECATTI, D., MACALUSO, G., PIERACCINI, M., ATZENI, C., SCHAFFHAUSER, A., FROMM, R. & NAGLER, T. 2009. Using a Ground-Based SAR Interferometer and a Terrestrial Laser Scanner to Monitor a Snow-Covered Slope: Results from an Experimental Data Collection in Tyrol (Austria). *IEEE Transactions on Geoscience and Remote Sensing*, 2, 382-393.
- MARSCHALLINGER, R., MÖLK, M. & IHRENBERGER, C. 2010. Geostatistische Raum-Zeit-Analyse der Deformationen am Hornbergl: Entscheidungsgrundlagen für die Abwehr von Schadensszenarien. *COGeo 2010 contribution*.
- MAZZANTI, P. 2011. Displacement Monitoring by Terrestrial SAR Interferometry for Geotechnical purposes. *Geotechnical Instrumentation News*, 25-28.
- MAZZANTI, P., BOZZANO, F., CIPRIANI, I. & ESPOSITO, F. 2011. Temporal prediction of landslide failure by continuous TInSAR monitoring. *contribution to 8th International Symposium on Field Measurements in GeoMechanics, Berlin, Germany, September 12-16, 2011*.
- MEIER, J., DATCHEVA, M. D., MOSER, M. & SCHANZ, T. 2009. Identification of Constitutive and Geometrical Parameters for Slope Instability Modelling – Application to Mountain-Splitting Area Reutte/Tyrol (Austria). *Austrian Journal of Earth Sciences*, 102/2, 81-89.
- MONSERRAT HERNANDEZ, O. 2012. Deformation measurement and monitoring with Ground-Based SAR. *unpublished Dissertation at the Universitat Politècnica de Catalunya*.
- MOSER, M., WUNDERLICH, T. A. & MEIER, H. 2009. Kinematische Analyse der Bergzerreiung Hornbergl – Reutte (Tirol). *Jahrbuch der Geologische Bundesanstalt*, 149, 177-193.
- PAULOSE, A. 1994. High Radar Range Resolution with the Step Frequency Waveform. *unpublished Master's Thesis*, Naval Postgraduate School, Monterey, California.
- PESTAL, G., HEJL, E., BRAUNSTINGL, R. & SCHUSTER, R. 2009. Geologische Karte von Salzburg 1:200.000. Erläuterung. *Wien: Geologische Bundesanstalt*.
- PLONER, A. & SÖNSER, T. 2005. Geologische Kartierung Hornbergl, Gemeinde Höfen. *unpublished Report for Wildbach- und Lawinenverbauung, Gbl. Auerfern*.
- RÖDELSPERGER, S. 2011. Real-time Processing of Ground Based Synthetic Aperture Radar (GB-SAR) Measurements. *Dissertation - Fachbereich Bauingenieurwesen und Geodäsie*, Schriftenreihe der Fachrichtung Geodäsie - Technische Universität Darmstadt.
- RÖDELSPERGER, S., BECKER, M., GERSTENECKER, C. & LAEUFER, G. 2009. Near real-time Monitoring of Displacements with the Ground Based SAR IBIS-L. *unpublished workshop contribution*.
- RÖDELSPERGER, S., BECKER, M., GERSTENECKER, C., LÄUFER, G., SCHILLING, K. & STEINECK, D. 2010. Digital elevation model with the ground-based SAR IBIS-L as basis for volcanic deformation monitoring. *Journal of Geodynamics*, 49, 241-246.

- ROSE, N. D. & HUNGR, O. 2007. Forecasting potential slope failure in open pit mines—contingency planning and remediation. *International Journal of Rock Mechanics and Mining Sciences*, 44, 308-320.
- SCHARES, J.-M. 2012. Verwendung einer GBSAR-Sensors am Hornbergl bei Reutte/Tirol - Installation und Messungen. *unpublished Master's Thesis*, Technical University of Munich.
- SCHMID, S. M., FÜGENSCHUH, B. & EDUARD, K. 2004. Tectonic map and overall architecture of the Alpine orogene. *Eclogae Geologicae Helvetiae*, 97, 93-117.
- SCHUHBÄCK, S. 2009. Kontinuierliche Überwachung der Massenbewegung am Hornbergl mit einem Low Cost GNSS Sensor Netzwerk. *Workshop Hornbergl 17./18.09.2009*.
- TARCHI, D., CASAGLI, N., FANTI, R., LEVA, D. D., LUZI, G., PASUTO, A. & PIERACCINI, M. 2003. Landslide monitoring by using ground-based SAR interferometry- an example of application to the Tessina landslide in Italy. *Engineering Geology*, 68, 15-30.
- TOLLMANN, A. & DEUTICKE, F. 1976a. Monographie der Nördlichen Kalkalpen, Analyse des klassischen nordalpinen Mesozoikums - Stratigraphie, Fauna und Fazies der Nördlichen Kalkalpen. Teil II.
- TOLLMANN, A. & DEUTICKE, F. 1976b. Monographie der Nördlichen Kalkalpen, Der Bau der Nördlichen Kalkalpen - Orogene Stellung und regionale Tektonik. Teil III.
- WILHELMSTÖTTER, F. 2013. Geotechnisch-Geologische Untersuchung des Felssturzgebietes Ingelsberg/Bad Hofgastein. *unpublished Master's Thesis*, Institute of Soil Mechanics and Foundation Engineering, Technical University of Graz.
- ZAMG 2012. Klimanormalwerte Österreich 1961-1990. *Zentralanstalt für Meteorologie und Geodynamik, Wien*, Software data for MS-Excel.
- ZAMG 2013a. Earthquakes in Austria. *Zentralanstalt für Meteorologie und Geodynamik, Wien*, http://www.zamg.ac.at/cms/de/geophysik/erdbeben/erdbeben-in-oesterreich/uebersicht_neu.
- ZAMG 2013b. Zentralanstalt für Meteorologie und Geodynamik, Wien. http://www.zamg.ac.at/cms/de/klima/klima-aktuell/klimaspiegel/jahr/zell_am_see/?jahr=2012, accessed on 02.10.2013.
- ZAMG 2013c. Zentralanstalt für Meteorologie und Geodynamik, Wien. <http://www.zamg.ac.at/cms/de/klima/klima-aktuell/klimaspiegel/jahr/reutte/?jahr=2012>, accessed on 09.09.2013.